Reduced Order Model-Based Prediction of the Nonlinear Geometric Response of a Panel Under Thermal, Aerodynamic, and Acoustic Loads

by

Andrew Matney

A Dissertation Presented in Partial Fulfillment
of the Requirements for the Degree
Doctor of Philosophy

Approved April 2014 by the
Graduate Supervisory Committee:

Marc Mignolet, Chair
Aditi Chattopadhyay
Hanqing Jiang
Jay Oswald
Stephen Spottswood

ARIZONA STATE UNIVERSITY

December 2014

ABSTRACT

This paper addresses some aspects of the development of fully coupled thermal-structural reduced order modeling of planned hypersonic vehicles. A general framework for the construction of the structural and thermal basis is presented and demonstrated on a representative panel considered in prior investigations. The thermal reduced order model is first developed using basis functions derived from appropriate conduction eigenvalue problems. The modal amplitudes are the solution of the governing equation, which is nonlinear due to the presence of radiation and temperature dependent capacitance and conductance matrices, and the predicted displacement field is validated using published data. A structural reduced order model was developed by first selecting normal modes of the system and then constructing associated dual modes for the capturing of nonlinear inplane displacements. This isothermal model was validated by comparison with full finite element results (Nastran) in static and dynamic loading environments. The coupling of this nonlinear structural reduced order model with the thermal reduced order model is next considered. Displacement-induced thermal modes are constructed in order to account for the effect that structural deflections will have on the thermal problem. This coupling also requires the enrichment of the structural basis to model the elastic deformations that may be produced consistently with the thermal reduced order model. The validation of the combined structural-thermal reduced order model is carried out with pure mechanical loads, pure thermal loads, and combined mechanical-thermal excitations. Such comparisons are performed here on static solutions with temperature increases up to 2200F and pressures up to 3 psi for which the maximum displacements

are of the order of 3 thicknesses. The reduced order model predicted results agree well with the full order finite element predictions in all of these various cases. A fully coupled analysis was performed in which the solution of the structural-thermal-aerodynamic reduced order model was carried out for 300 seconds and validated against a full order model. Finally, a reduced order model of a thin, aluminum beam is extended to include linear variations with local temperature of the elasticity tensor and coefficients of thermal expansion.

ACKNOWLEDGEMENTS

First, I would like to thank Dr. Mignolet for his constant involvement in my work. Without his knowledge, guidance, and direction the progress made thus far on the project would not have been possible. I would also like to thank Dr. Spottswood, who has consistently supported and been involved in my work, and who has sponsored my visits to the Air Force Research Lab over the past few summers. Additionally, the assistance that I have received from Dr. Culler was essential to the completion of this project. His help is gratefully acknowledged. I would like to acknowledge the instruction I received from Dr. Jiang, who taught me the fundamentals of solid mechanics, and thank him for his willingness to serve on my committee. Finally, I would like to thank Dr. Oswald and Dr. Chattopadhyay for serving on my committee.

TABLE OF CONTENTS

Page

CHAPTER Page

LIST OF TABLES

LIST OF FIGURES

Figure Page

Figure Page

Figure Page

Figure Page

Figure Page

Figure Page

Figure Page

CHAPTER 1 – INTRODUCTION

One of the goals of the United States Air Force is to field a manned, reusable, air-breathing hypersonic aircraft. This pursuit has been met with a number of challenges within a number of disciplines including aerodynamics, structural dynamics, heat transfer, material science, guidance and control, and propulsion. These challenges have been the subject of considerable research, yet much progress is still needed in order to field such an aircraft. The Air Force Research Lab (AFRL) Structural Sciences Center recently initiated an effort with partners in industry that sought to understand and summarize the knowledge gaps relating to structural design that inhibit the development of such a vehicle. The first phase of the project involved a survey of previous attempts to produce a reusable hypersonic vehicle, and the shortcomings experienced therein [1-3]. A number of projects were reviewed, including the National Aerospace Plane (NASP) and the X-33. Both efforts arrived at very similar conclusions regarding knowledge gaps. These include, but are not limited to, the evolution of material properties when structures are exposed to extreme heating, the coupling of the aero-thermal-acoustic disciplines, the nonlinear response of the structure, and the accurate determination of thermo-acoustic loading conditions, to name a few. The standard approach taken was to assume a worst-case scenario in which the most extreme case of each loading type was assumed to act on the structure simultaneously. A linear analysis ensued in which superposition was used to combine the effects of the various loads. This produced an overly conservative design, which added weight and cost to the vehicle. Additionally, the uncertainty in the response

to a coupled loading environment led to a more conservative design, which translates into higher weight, and higher cost.

This assumption of linearity was tested in [4], in which a NASP ramp panel was subjected to thermal and acoustic loads expected in the flight regime. A linear and nonlinear analysis was performed, with the linear analysis overpredicting the response of the panel. This overprediction in deflection translated into an overprediction in the stress and a prediction of fatigue failure. However, the nonlinear analysis produced smaller deflections due to geometric nonlinearity and did not predict fatigue failure, showing the unnecessary cost of assuming a linear approach to the problem.

In the second phase of the program four critical regions were selected on a concept vehicle and panels from these regions were designed and used for further study [5-8]. Analysts confirmed the knowledge gaps identified in Phase I, with a few more knowledge gaps identified [6]. These panel models are intended to be used in future research so that the aerospace community can solve some of the issues inhibiting the development of a reusable hypersonic vehicle.

Many of the knowledge gaps identified involve the accurate coupling of the disciplines present in hypersonic flight. The desire to accurately model the coupling of the structural, thermal, and aerodynamic problems in hypersonic conditions has been the focus of a number of recent studies [9-13]. One study by Culler and McNamara sought to test the assumptions that are typically made regarding the two-way coupling of the structural and thermal problem on a representative hypersonic panel [10]. Early attempts to investigate the effects of coupled analyses at hypersonic speeds would neglect the two-

way coupling between the structural displacement and the aerodynamic heating, instead assuming that the structural displacements were influenced by the temperature fields while the thermal problem was not influenced by the displacements [14-17]. Although an appropriate assumption to make when panel deflections are relatively small, the influence of the displacement field on the aerodynamic heating of the structure becomes significant at large displacements. The influence of large deformations on the temperature field of the structure was later observed [18-21], but a comprehensive investigation into the influence of two-way coupling on stress and dynamic stability of the structure was not performed.

Culler and McNamara have undertaken to better understand the influence of two-way coupling in hypersonic flight conditions, and their efforts are presented in [9] and [10]. In the investigation of [10], a representative hypersonic panel is used. That panel, shown in Fig. 1, was derived from an inlet ramp panel featured in [22,23].

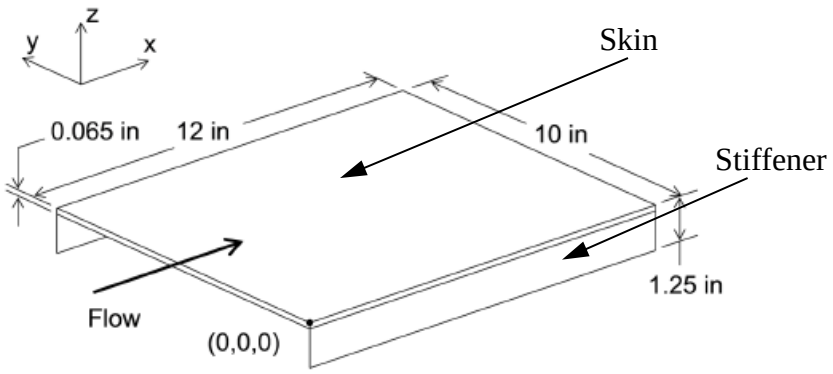

Figure 1. Representative Hypersonic Panel Model

Two different flight trajectories were used, one which maintains constant freastream conditions of Mach 12 flow, while the other uses a constant rate ascent trajectory

analysis, maintaining a constant dynamic pressure and linearly increasing the Mach number of the freastream flow from 2 to 12 over 300 seconds. It will be the latter trajectory that will be the focus of this current research. In [10], the boundary conditions of the representative panel were varied in order to assess their influence on the two-way coupled analysis. When the panel was allowed to expand freely, the resulting displacements, stresses and failure indices from the two-way and one-way analyses strongly agreed. However, when the resistance to inplane expansion was set to its maximum level, the two solutions produced very different results. In both analyses the panel buckled into the flow, and this large deflection produced a significant effect on the aerodynamic heating in the two-way coupled analysis. The resulting temperature field caused the panel in the two-way coupled analysis to be dominated by a higher order mode, while the one-way coupled model remained dominated by the lowest order mode. As the displacements diverged, the stress and failure indices did as well, resulting in the prediction of failure for the one-way coupled analysis. Additionally, the one-way coupled analysis produced a displacement that was not dynamically stable, while the two-way coupled response was stable at all points of the analysis. The reason these differences emerged was that the resistance to inplane expansion caused the panel to buckle into the flow. With such large deflections the effect of two-way coupling was no longer negligible, as the deformations had a strong influence on the aerodynamic heating of the panel.

In order to carry out these simulations, a number of simplifications had to be made. Lower fidelity, yet still reliable models were used for the aerodynamic heating and

aerodynamic pressure. Eckert's reference enthalpy method was used for aerodynamic heating [24,25], which provided the convection boundary conditions to the thermal model of the panel. Piston theory was used for aerodynamic pressure [26,27]. Here, the cubic form of the heating model was used due to the large deflections and high Mach numbers experienced [28]. The structural response was assumed to be quasi-static, due to the difference in the thermal and structural time scales (for details, see [10]).

This analysis played a significant role in advancing understanding of the effect of structural-thermal-aerodynamic coupling in hypersonic environments. It is here desired to advance predictive capabilities further by developing a structural-thermal reduced order model of this panel, and repeating the fully coupled analysis presented in [10]. As the discussion in [1-8] indicates, the fully coupled, long-duration, nonlinear dynamic analysis for structural response prediction in hypersonic flight environments cannot currently be completed due to the time and computational resources required. This being the case, the last 15 years has seen the development of a number of model reduction techniques emerge, with the goal of reducing the computational resources required for long-duration analysis.

The thin-walled aircraft panels that ROMs have been developed for will behave in a geometrically nonlinear manner during hypersonic flight. This complicates the analysis in two ways. First, it produces quadratic and cubic nonlinearities in the equation of motion. Second, it couples the transverse and inplane dominated modes. When a flat structure experiences large transverse deflections in a nonlinear analysis, a membrane stretching is nonlinearly induced. The cubic properties of the system typically harden the

system, while the quadratic nonlinearities typically soften the system through the inplane-transverse coupling [29].

The methods by which the nonlinear terms are acquired are varied, typically separated into two classes; direct and indirect methods. Direct methods assume that the user has access to the finite element nonlinear stiffness terms, and is able to manipulate them for the purposes of the reduced order model. This method was used by [30,31] in early investigations of reduced order modeling for flat structures. However, commercially available finite element packages do not typically make this information available, so it has become the goal of a number of recent projects to develop reduced order models indirectly, or without direct access to the stiffness matrices of the particular finite element program. These methods employ a series of static, nonlinear finite element solutions in order to relate the nonlinear stiffness terms to the forces applied.

In [32], Maymon describes a procedure by which the nonlinear stiffness parameters of the governing equation of motion will be fit to finite element data through either applied forces or prescribed displacements. Through this process, a single-mode ROM is attained; however, he does not go into detail about any specific model or results. McEwan et al took this a step further in [33], detailing a process by which the cubic stiffness terms in a multi-mode reduced order model were determined using a series of static solutions when the finite element model is subjected to prescribed loads. The procedure utilizes the displacements determined by the finite element program, as well as the prescribed forces, with both of these properties being transformed into modal space. The loads prescribed need to exercise the nonlinearity of the model, as well as include the

cross coupling between the selected modes. Thus, the applied loads were determined to be proportional to a linear combination of the truncated set of normal modes to be used in the reduced order model basis. A regression analysis was then used to curve fit the nonlinear coefficients to the data provided by the finite element program. The procedure outlined provided good results when used with a fully clamped and simply supported beam.

Muravyov and Rizzi outlined a similar procedure to [33], but used enforced displacements as opposed to applied loads [34]. In this procedure, the displacements are prescribed and the nodal forces required to retain this deformation are solved for by the finite element program. The displacements and forces are transformed to modal space, and the unknown stiffness coefficients are solved for. This procedure will be reviewed in Section 3.3.1.1. Nonlinearity should be exercised, as well as the coupling between multiple modes. As with the previous method, it was again found necessary to prescribe a linear combination of structural modes, however, displacements proportional to a maximum combination of three different modes is used for any given test case in this procedure.

With the methods for determining the nonlinear stiffness coefficients described, the methods for accounting for the transverse displacement induced membrane stretching will be reviewed. The method employed by [31,33] was to statically condense the inplane behavior into the transverse motion. The inplane behavior of a flat structure is very stiff, resulting in the inplane-dominated modes having a high natural frequency. The frequency of excitation the structure is subjected to is assumed to be much lower than the natural

frequency of inplane dominated modes, allowing the inplane behavior to be assumed to be a static response to the large transverse deformations. By assuming the response is quasi-static, the mass and damping terms can be removed and the inplane response is written in terms of the transverse generalized coordinate. Thus, the effect of the inplane modes on the transverse response is condensed. This condensation allows the reduced order model to have a basis of purely transverse modes, while still ensuring that the coupling effect that the inplane modes have on the transverse modes is accurately retained.

There are a number of ways to employ static condensation. In [29], Holllkamp et al. discusses a number of methods that involve static condensation, including explicit physical condensation [31], explicit modal condensation, and condensation involving companion modes. However, the most popular method is implicit condensation (IC). The applied force method for identifying nonlinear coefficients naturally pairs well with implicit condensation. By applying transverse loads and allowing the structure to deform freely in the inplane direction, the coefficients identified naturally accommodate the implicit condensation procedure. In [29], the implicit condensation method was shown to produce good results for a flat and curved beam under acoustic loading. Additionally, in [35], the response was accurately predicted for a curved beam under acoustic and uniform thermal loads. The work presented in [36] and [37] show that the ROM built using the implicit condensation method predicted results that agree well with experiments.

One of the drawbacks from this analysis is that the inplane displacements are not determined by the ROM when static condensation is employed. Because of this, the

associated stress fields of the ROM predicted displacements cannot be determined in the typical finite-element fashion. To enhance this modeling strategy, Hollkamp et al. presented a method in [38] in which the transverse displacements were used to extract associated inplane displacements that had been condensed into the transverse modes. Generally speaking, the modal amplitudes of the inplane modes are assumed to be dependent on the square of the modal amplitudes of the transverse modes. With these amplitudes estimated, the associated inplane modes are then determined by relating the displacements generated from the applied loads cases to the mode shapes and normal mode amplitudes already defined. The details of this procedure can be found in [38,39]. This procedure of implicit condensation and expansion (ICE) was shown to produce accurate results when using a flat and curved beam [38]. However, when a curved beam subjected to thermal loading was investigated in [40], the IC method was favored over the ICE method.

Hollkamp and Gordon recently developed a reduced order model of the panel from [10], however the material properties were modified [41]. The goal of this effort was to show that reduced order models are a legitimate option when it comes to simulating the response of complex structures to large thermal loads. With this being the case, a number of simplifications were made. The structural reduced order model was developed, but a thermal ROM was not since the purpose of the investigation was simply to validate the reduced order modeling procedure for the representative hypersonic panel under intense thermal loads. The through thickness temperature gradient was neglected, as well as the static pressure loads, and the analysis was performed up to Mach 7 as

opposed to the original upper limit of Mach 12. Transverse-dominated and inplane-dominated modes were included, and the enforced displacements procedure was used to identify the nonlinear coefficients. Results showed that the structural ROM was capable of producing good results with few modes when compared to the displacements predicted by the full order model.

Other attempts to capture the effect of the membrane stretching have been put forward by Rizzi and Przekop. In [42-44], normal inplane modes are included in the structural basis and the nonlinear parameters are identified using the enforced displacement method, which naturally pairs well with a modal basis consisting of all types of degrees of freedom. In [42,43], the modal basis is selected to include a fixed number of transverse dominated normal modes and inplane dominated normal modes, and this basis was shown to produce results that agreed well with finite element results for a thermally buckled beam [42] and curved beam [43]. In [44], a methodology was put forward to guide the modal basis selection that did not depend as strongly on the ROM developer's intuition or a priori knowledge of the expected structural response. In this work, the structure under consideration was subjected to loading conditions that resembled a relatively severe loading case, and a dynamic full order analysis was performed to provide a sample of the dynamic response. The displacements were partitioned into transverse and inplane components, and a POD analysis was performed on the displacement sets so that the stiffer inplane modes would not be overlooked in the analysis (see [45] and [46] for a discussion on POD analysis applied to structural displacements). The dominant POD modes (POMs) were identified by their associated

proper orthogonal values (POVs), and the participation of each POM was evaluated using Eq. (1).

$$\chi_i = \frac{\lambda_i}{\sum_{j=1}^{N} \lambda_j}, \quad i = 1,..., N \tag{1}$$

Here, χ_i denotes the POM participation factor, while λ_i denotes the POV of the i^{th} mode and N is the total number of modes. The POMs with the highest eigenvalues are selected for inclusion in the reduced order basis until the cumulative POM participation factor is at a satisfactory level. The cumulative POM participation factor, ν, is given in Eq. (2).

$$\nu = \sum_{i=1}^{M} \chi_i, \quad 0 < \nu \leq 1 \tag{2}$$

Here, M is the number of selected POMs to be included in the basis. Next, the modal assurance criterion, or MAC, is used to identify the normal modes of the system that correlate with the selected POMs [47]. These normal modes comprise the final ROM basis. This process was termed the modal amplitude participation procedure, or MAP. The validation cases were repeated for the flat and curved beams, and the results showed that the new basis retained the accuracy exhibited in [42,43], while increasing the efficiency of the ROM by requiring fewer modes.

In [48], Przekop et al outline two additional procedures that assist the ROM developer in selecting a basis. In [49] and [50] the authors derive a means of acquiring the natural frequency of POMs in a process that utilizes smooth orthogonal decomposition. This process requires the velocity data in addition to the displacement data needed for the POD analysis. Additionally, [46] observed that the mean square of the modal amplitudes converge to the mode's POV as the number of dynamic snapshots of

the lightly damped response to acoustic loading becomes very large. These two observations allow the authors in [48] to derive a method to estimate the energy provided by each POM during the analysis. By considering energy in the modal selection process, the inplane modes that tend to have small modal amplitudes relative to the transverse modes can still be selected. This is due to the fact that the inplane modes are very stiff, and even small displacements may entail a significant amount of energy present in the system. In a manner similar to that of Eq. (1), the modal energy participation factor is determined, and the highest energy modes are selected for inclusion in the ROM basis. The total number of modes to be included in the basis is decided on once the cumulative energy participation factor, analogous to Equation 2, is determined to be at the desired level. These modes are then correlated with the normal modes through a process expressed in Eq. (3).

$$C_{\text{exp}} = \Phi^T P \tag{3}$$

C_{exp} is the expansion coefficient matrix, Φ^T is the matrix of all normal modes, and P is the matrix of selected POMs. C_{exp} expresses the linear combination of normal modes required to construct a given POM in P. The modes contributing most significantly to the construction of a selected POM will be retained in the final reduced order basis. Finally, the estimated POM frequencies approach (EPF) selects the modes whose frequencies are within a certain bandwidth. The selection process for the MEP and EPF methods in [48] were modified in order to perform a more direct comparison with the MAP procedure. Each method performed well, with the EPF having a slight advantage over the other two. One other observation was that the MEP approach tended to favor a

selection of transverse dominated modes when compared to the other selection procedures.

In [51], the authors demonstrate that a model developed using the MAP approach can accurately predict the response to pressure loads which vary spatially and temporally. A high pressure region is prescribed to oscillate over a beam which is otherwise under lower pressure loading, as well as acoustic loading. Multiple basis sets were developed to account for the excitation produced by a stationary high pressure region when that region was located at various points on the beam. One cumulative basis was selected to account for every normal mode present in each of the basis sets. Consolidating the different basis sets allows for a single reduced order model to accurately predict the response of the beam under high pressure loads when the load is applied at any of the previously investigated locations, further increasing the efficiency of the ROM.

In [52-54], the concept of a "dual" mode was introduced and developed in order to account for the inplane displacements induced by nonlinear coupling with the transverse motion. In this formulation, the low order linear modes are first included in the ROM basis. Then, a series of static displacements are found from forces that are proportional to combinations of two linear modes. One mode is set as the dominant mode, and forces generated from combining this mode with all other linear modes are enforced on the structure. This is done at various loading levels, in order to exercise the nonlinearity of the problem. Then, the resulting displacements are made orthogonal to the linear modes in order to extract the nonlinearly induced components and a POD analysis is performed on these displacement vectors. The POD modes with the largest associated

eigenvalue, or POV, and strain energy are selected to be included in the basis. The strain energy is used as a measure for selecting dual modes because the inplane behavior of the panel will be stiff and modes with high inplane displacement will have large strain energy. This process was validated with isotropic and functionally graded panels to show its usefulness for symmetric and asymmetric structures [54]. Additionally, this dual-based formulation of the nonlinear ROM was extended for use in cantilevered ROMs [55]. The weak nonlinearity exhibited by the behavior of a cantilevered beam required that the typical approach be modified. Specifically, the inplane displacements were condensed into the transverse motion, and subsequently "decondensed" in order to have a full dof description of the structural response of the beam. In [35], the dual-based approach was shown to accurately model a curved beam under significant acoustic and uniform thermal loading.

A significant enhancement to the capabilities of reduced order modeling was introduced in [56]. A method to incorporate the effects of spatially varying temperature fields into the structural reduced order model was derived and validated. The derivation showed that the temperature field would influence the linear stiffness matrix, as well as the thermal moment. Each of these exhibits a linear relationship with temperature. Further, a modal approach was taken for the thermal model, resulting in a one-way coupled structural-thermal reduced order model. Results were found in static conditions in [56,57], and [58] extended these validations to unsteady thermal environments as well. Additionally, the accurate prediction of stress fields were shown for the structure under thermal loading in [58].

A number of investigations into shock-boundary layer interactions have concluded that a shock impingement will produce localized heating [59], as well as oscillating pressures [60,61], to the point that it could affect the fatigue life of a structure. It is therefore important for structural models to have the ability to accurately predict the response to unsteady thermal and aerodynamic pressure loading. In an effort to prove the capability of ROMs to model the response to oscillating thermal loads, a ROM was developed for a long, thin beam subjected to an oscillating heat source [62]. The frequency of oscillation varied from approximately 20 Hz, to just over the natural frequency of the beam, approximately 80 Hz. The ROM predicted displacements that were in agreement with the full order results when the thermal loading was applied, as well as in the presence of thermal and acoustic loading.

Furthermore, the thermoelastic formulation was recently extended in [63,64] to include temperature dependent material properties. Specifically, the Young's modulus and the coefficient of thermal expansion were assumed to vary linearly with temperature. Propagating this linear dependence of temperature throughout the structural ROM formulation showed that the linear stiffness matrix and thermal moment term would now have a cubic relationship with temperature. The quadratic and cubic stiffness tensors would now be linearly related to temperature. A method to identify these new coefficients was presented and subsequently validated with a beam model.

Perez et al presented work in [65] in which a reduced order model was developed for a 96,000 dof panel model. As the number of modes in the ROM basis increases, the number of nonlinear coefficients to be identified increases with the cube of the number of

modes, as well as the number of nonlinear enforced displacement cases required to identify those terms. In order to reduce the computational resources required to identify these parameters a new method was presented which utilizes the tangent stiffness matrix occurring at prescribed displacements, as opposed to the forces required to maintain a certain displacement field. The number of cases that must be run to identify the nonlinear coefficients is related to the square of the number of modes, significantly reducing the computational resources and time required to identify the ROM. Static cases showed agreement between the ROM and full order models, and preliminary dynamic results showed agreement as well.

In addition to the structural ROM, a thermal ROM will need to be developed. In developing a reduced order model for the thermal problem, a modal approach is taken, similar to the structural problem. A full derivation of this can be found in [56]. The primary issue in the construction of a thermal ROM is the selection of the thermal modes. In [56-58], the thermal basis was constructed using modes that are meant to satisfy nonhomogonous boundary conditions, as well as modes that were the product of the eigenvectors of the 1-D conductance capacitance eigenvalue problem and a function related to the through thickness temperature variation. It was found that linear and cubic through thickness temperature variations were needed to model the temperature fields in an unsteady environment. In [64], the eigenvectors of the 1-D eigenvalue problem were again combined with linear and cubic functions related to through thickness temperature variation. These modes were shown to produce accurate results under rapidly oscillating heat sources.

Falkiewicz and Cesnik developed thermal reduced order models in [66] to test their applicability to hypersonic control surface modeling. It was decided that POD modes would serve as the optimal basis for this thermal problem. A sample of temperature fields were generated for a given loading scenario and a POD analysis was then carried out on these temperature fields. The POD modes were then used to simulate the temperature evolution on the control surface using the modal form of the heat conduction equation, and excellent results were observed with relatively few modes. A constant and time-dependent load vector was used in the analyses and the reduced order model developed from each of these produced accurate results. It was observed that POD modes were able to contribute to the prediction of temperatures when the load applied was different from the load used to generate the snapshots from which the POD modes were generated. Also, the POD modes from the constant flux case were able to improve the predictions of the time-dependent heat flux case.

In [67], this thermal reduced order modeling strategy is extended for use in a fully coupled aeroelastic analysis of a hypersonic control surface. The thermal modes were comprised of POD modes generated from snapshots of the temperature fields occurring in a simplified, representative case. A structural ROM was developed, and the structural modes were comprised of Ritz modes, which were several normal modes of the structure when the structure was subjected to the average temperature field of the thermal analysis just mentioned. Additionally, the structural response to this average thermal loading case was incorporated into the basis. The aerodynamic heating was modeled using CFD-based kriging surrogates [68-70], while the aerodynamic pressure was found using Piston

theory [26,27]. The models were validated, and the ensuing analysis found that aeroelastic effects will have a significant impact on the aerodynamic forces, both lift and drag, of the control surface.

The fully coupled, partitioned analysis in [67] is similar to the analysis that will be presented in the subsequent chapters. One of the main differences, though, is the inclusion of nonlinear structural and thermal properties of the current work. Therefore, in the context of this brief review, the contributions of this present work are to incorporate nonlinear reduced order models into a fully coupled structural-thermal-aerodynamic ascent trajectory simulation, develop a ROM of increased complexity, relative to previous models, and accurately predict responses to extreme temperatures.

Additionally, in order to fully demonstrate the ability of the structural reduced order model to incorporate temperature dependent material properties, a reduced order model of a beam with temperature dependent Youngs modulus and coefficient of thermal expansion will be developed. The structural model of the ramp panel described above includes only the coefficient of thermal expansion that is dependent on temperature. Here, validation efforts are presented to model the structural response to non-uniform and time varying temperature fields produced by an oscillating heat flux on a thin beam, shown in Fig. 2. Previously, this methodology was only validated with a uniform temperature field [63].

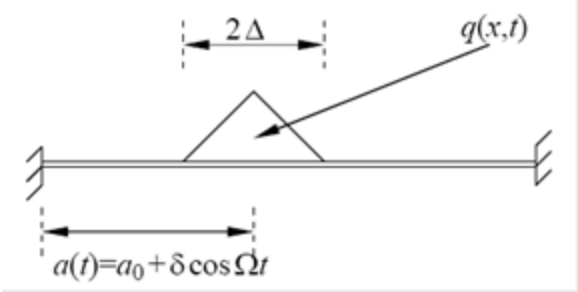

Figure 2. Model Problem for the Validation of a Reduced Order Model With Temperature Dependent Material Properties.

Finally, it should be noted that the primary goal for the structural model is the accurate prediction of displacements. While other projects have shown that stress can be accurately predicted using reduced order models [52,58], stress values will not be calculated in this analysis. As stress is a derived quantity, the accuracy of displacement will be given priority and will be the only metric by which the structural model is evaluated.

CHAPTER 2 – MODEL DESCRIPTION

2.1 Representative Panel

2.1.1 Structural Model

The panel used here, shown in Figure 1, is the same panel modeled using full order finite element analysis in [10]. The skin of the panel is 12 inches long in the direction of the flow, 10 inches wide and 0.065 inches thick. The stiffeners along the left and right edge of the skin are 1.25 inches wide and .0325 inches thick. The structural finite element model is composed of 2400 CQUAD4 (4 node plate) elements, resulting in 2499 nodes. In both the structural and thermal problems the dimensions of the element were 0.25 in. by 0.25 in.

The panel has the following structural boundary conditions [10]:

(1) At the leading edge, x=0 and z=0, zero displacements are enforced for all degrees of freedom but y translations, which are free.

(2) At the trailing edge, x=12 and z=0, zero displacements are enforced for all degrees of freedom except x and y translations, which are free. Springs also act on the nodes of the trailing edge in the *x* direction with a spring constant of 2378 lb/in.

(3) At the panel center, x=6, y=5, and z=0, zero displacement is enforced for y translations.

The structural properties of the composite material used in this model, advanced carbon-carbon 4, are provided in Tables 1 and 2 [22,23,71-73]. These properties, except for the coefficient of thermal expansion (CTE) will remain constant since there is no significant change over the range of temperatures experienced in this analysis [74]. In the

analysis of [10], the CTE value is linearly related to temperature until the temperature reaches 2190F, and above this temperature the value remains constant. The reduced order model, on the other hand, is formulated to be able to incorporate temperature dependent properties that are expressed as a polynomial with respect to temperature (see formulation in Section 3.1). In this analysis, the CTE will be assumed to vary linearly with temperature for the duration of the analysis with the same linear relationship that is used up to 2190F in the analysis of [10]. The full order results from Nastran will be found using the same linear variation of CTE over the entire temperature range in order to make a straightforward comparison between the full and reduced order model. The mean temperature of the panel exceeds 2190F only for the last 12 seconds of analysis, and comparisons between Nastran models with the two different CTE properties showed that the differences between structural displacements of the two models were minimal.

Table 1. Material Properties of Panel

Density	0.065	lbm/in^3
Young's $Modulus_{11}$	15 E6	psi
Young's $Modulus_{22}$	15 E6	psi
Shear $Modulus_{12}$	2.5 E6	psi
Poisson's $Ratio_{12}$	0.3	

Table 2. Temperature Dependent Characteristics of CTE

Temperature, ºF	CTE 1/ºF
30	0.556 E-6
2500	2.334 E-6

2.1.2 Thermal Model

There are 2400 elements in the thermal finite element model, with the skin being composed of CHEXA (8 node brick) elements and the stiffeners being composed of

CQUAD4 elements, resulting in 4508 nodes. The CHEXA elements allow for the through thickness temperature gradient to be calculated, which is then provided to the structural model. The surface of the stiffeners were assumed to be adiabatic, as well as the bottom surface of the skin. The top of the skin is exposed to the flow and the thermal loading predicted by the aerothermal analysis is imposed on the surface through a convection boundary condition, depicted in Eq. (4).

$$Q_{aero} = h_{conv}(T_{aw} - T_w) \tag{4}$$

Q_{aero} is the flux acting on the surface, h_{conv} is the heat transfer coefficient, T_{aw} is the adiabatic wall temperature, and T_w is the wall temperature. Additionally, effects of radiation on the top of the skin are modeled using Eq. (5) as provided in [10],

$$Q_{rad} = \sigma \cdot \varepsilon \cdot T_w^4 \ , \tag{5}$$

where the emissivity factor (ε) is 0.8 and the Stefan-Boltzmann constant (σ) is 3.302 E-15 BTU/s/in^2/R^4. The thermal properties are provided in Table 3 and the variation of specific heat and in-plane thermal conductivity with temperature is given in Table 4 [22,75].

Table 3. Thermal Properties at 70 °F

Density	0.065	Lbm/in.^{3}
Specific Heat	0.18	BTU/lbm/°F
Thermal Conductivity$_{11}$	18.6	BTU/ hr/ft /°F
Thermal Conductivity$_{22}$	18.6	BTU/ hr/ft /°F
Thermal Conductivity$_{33}$	3.0	BTU/ hr/ft /°F
Emissivity, ε	0.8	

Table 4. Specific Heat and Inplane Conductivity as a Function of Temperature

Temperature °F	Specific Heat BTU/lbm/°F	In-plane Conductivity BTU/hr/ft/°F
0	0.170	17.5
200	--	20.9

500	0.242	23.6
750	-	24.2
1000	0.295	24.2
1250	-	23.9
1500	0.330	23.3
1750	-	23.1
2000	0.360	22.5
2250	-	21.9
2500	0.390	21.4
2750	-	20.9
3000	0.420	20.3

2.1.3 Aerodynamic Pressure Model

The panel under consideration is assumed to be at an angle of 5º with the free stream flow. Additionally, the panel is 60 inches upstream of the transition from laminar to turbulent boundary layer. The properties of the free stream flow are defined such that the Mach number varies linearly with time, increasing from 2 to 12 over 300 seconds, and the dynamic pressure is defined as 2000 psf throughout the analysis. Oblique shock relations are used to compute the inviscid flow properties downstream of the shock [76], which will occur upstream of the panel under consideration, and as long as the body of the hypersonic aircraft is rigid and the flow remains parallel to it, the inviscid flow properties will be constant at all points downstream of the shock. However, deformations of the panel will produce nonuniform flow properties on the surface of the panel. The pressure acting at each point on the surface of the panel is found using piston theory [26,27], specifically third order piston theory due to the high Mach numbers and deflections. Piston theory has shown to be a very efficient aerodynamic model that maintains reasonable accuracy during hypersonic flight as long as the product of Mach

number and the angle of inclination of the panel remain below 1 [28]. The third order piston theory equation is shown in Eq. (6).

$$p_1 = p_0 + 2\frac{q_0}{M_0}\left[\left(\frac{1}{U_0}\frac{\partial w}{\partial t}+\frac{\partial w}{\partial x}\right)+\frac{\gamma+1}{4}M_0\left(\frac{1}{U_0}\frac{\partial w}{\partial t}+\frac{\partial w}{\partial x}\right)^2 + \frac{\gamma+1}{12}{M_0}^2\left(\frac{1}{U_0}\frac{\partial w}{\partial t}+\frac{\partial w}{\partial x}\right)^3\right] \quad (6)$$

Here, the subscript 0 denotes inviscid flow properties after the shock but upstream of the panel, while the subscript 1 denotes a property at the specific point of the panel in question [10]. w is the transverse displacement, x is the direction of the flow, t is time, p is pressure, q is dynamic pressure, U is velocity, and γ is the ratio of specific heats.

2.1.4 Aerodynamic Heating Model

Piston theory is not a complete aerodynamic model, in the sense that it does not determine aerodynamic heating. In order to model the heating that is imposed on the panel, the semi-empirical Eckert's reference enthalpy method is used [24,25]. This heating model provides the convection boundary condition to the thermal model of the panel. Additional details can be found in [10].

2.1.5 Solution Procedure

In order to determine the quasi-static solution, a staggered solution sequence is employed, which sequentially determines the aerodynamic pressure, aerodynamic heating, temperature fields, and structural deflections. The aerodynamic pressure, convection boundary conditions, and structural displacement are calculated every half

second, while the transient thermal solution is calculated at every tenth of a second. Once the structural deflections are determined, the aerodynamic pressure is updated and the structural deflections are recalculated. The solutions of the structural and aerodynamic problems are repeated until convergence. For more details on the justification of the quasi-static assumption and the selection of the simulation time steps, see [10].

2.2 Beam Model

The beam, a rough schematic of which is shown in Figure 2, has the following properties.

Table 5. Clamped-Clamped Beam Properties

Beam Length (L)	0.2286 m
Cross-section Width (w)	0.0127 m
Cross-section Thickness (h)	$7.88\ 10^{-4}$ m
Density	2700 kg/m^3
Young's Modulus	73,000 MPa
Shear Modulus	27,730 MPa
Coeff. Thermal Expansion	$2.5\ 10^{-5}$ /°C
Mesh (CBEAM)	40

Further, the changes with temperature of the Young's modulus and coefficient of thermal expansion were assumed as in Eqs (7) and (8), i.e.

$$E = E^{(0)} - E^{(1)}\,T \tag{7}$$

and

$$\alpha = \alpha^{(0)} - \alpha^{(1)}\,T \tag{8}$$

with $E^{(1)} = 3.0\ 10^9$ Pa/°C and $\alpha^{(1)} = 5.0\ 10^{-7}$ 1/°C^2. The Poisson's ratio was assumed to be temperature independent here. Note that these values are not representative of

aluminum but rather were selected to ensure a notable change in properties with the range (10°C) of temperature experienced by the beam.

CHAPTER 3 – REDUCED ORDER MODEL FORMULATION

3.1 Thermal and Structural Governing Equations

The derivation of the governing equations follows the approach taken in [56-58,62-64]. It is desired here to represent both temperature and displacement fields in a "modal expansion" form, i.e. as

$$T(\underline{X},t) = \sum_{n=1}^{\mu} \tau_n(t)\, T^{(n)}(\underline{X}) \tag{9}$$

for the temperature, and

$$u_i(\underline{X},t) = \sum_{n=1}^{M} q_n(t)\, \psi_i^{(n)}(\underline{X}) \tag{10}$$

for the displacement. In these equations, the functions $\psi_i^{(m)}$ and $T^{(m)}$ are specified functions of the position vector $\underline{X}$ in the *undeformed* configuration, chosen to satisfy the necessary boundary conditions.

To obtain a set of (nonlinear) ordinary differential equations governing the evolution of the generalized coordinates $q_n(t)$ and $\tau_n(t)$, it is first necessary to derive the governing field equations for the displacements $u_i(\underline{X},t)$ and temperature $T(\underline{X},t)$ in the undeformed configuration. Following references [77-79], one obtains (see also [57,58,54])

$$\frac{\partial}{\partial X_k}\left(F_{ij}\, S_{jk}\right) + \rho_0\, b_i^0 = \rho_0\, \ddot{u}_i \qquad \text{for } \underline{X} \in \Omega_0 \tag{11}$$

where $\underline{\underline{S}}$ denotes the second Piola-Kirchhoff stress tensor, ρ_0 is the density in the reference configuration, and $\underline{b}^0$ is the vector of body forces, all of which are assumed to

depend on the coordinates X_i of the undeformed configuration in which the structure occupies the domain Ω_0. Further, in Eq. (11), the deformation gradient tensor $\underline{\underline{F}}$ is defined by its components F_{ij} as

$$F_{ij} = \frac{\partial x_i}{\partial X_j} = \delta_{ij} + \frac{\partial u_i}{\partial X_j} \tag{12}$$

where δ_{ij} denotes the Kronecker symbol and the displacement vector is $\underline{u} = \underline{x} - \underline{X}$, $\underline{x}$ being the position vector in the deformed configuration.

The heat conduction equation on the domain Ω_0 can be written as

$$\rho_0 \, T \, \dot{\mathcal{S}} = \frac{\partial}{\partial X_i}\left[k_{ij}^0 \, \frac{\partial T}{\partial X_j} \right] \tag{13}$$

where $\mathcal{S}$ denotes the specific entropy and $\underline{\underline{k}}^0$ denotes the conductivity tensor pulled back to the undeformed configuration according to

$$\underline{\underline{k}}^0 = \det\left(\underline{\underline{F}}\right) \underline{\underline{F}}^{-1} \, \underline{\underline{k}} \, \underline{\underline{F}}^{-T} \tag{14}$$

where $\underline{\underline{k}}$ is the conductivity tensor in the deformed configuration.

To complete the formulation of the problem, it is necessary to define the material constitutive relations which stem from the Helmholtz free energy (per unit mass) $\mathcal{F}$ defined as

$$\mathcal{F} = \mathcal{E} - T \, \mathcal{S} \tag{15}$$

where $\mathcal{E}$ denotes the elastic energy. Specifically, one has

$$\rho_0 \left(\frac{\partial \mathcal{F}}{\partial E_{ij}} \right)_T = S_{ij} \quad \text{and} \quad \left(\frac{\partial \mathcal{F}}{\partial T} \right)_{E_{ij}} = -\mathcal{S} \tag{16),(17}$$

where $\underline{\underline{E}}$ denotes the Green strain tensor, i.e.

$$E_{ij} = \frac{1}{2}\left(F_{ki}\, F_{kj} - \delta_{ij}\right). \tag{18}$$

The Duhamel-Neumann form of the Helmholtz free energy [77] is adopted in the undeformed configuration. Specifically, it is postulated that

$$\rho_0\, \mathcal{F} = \frac{1}{2}\, C_{ijkl}\; E_{ij}\; E_{kl} - C_{ijkl}\alpha_{kl}\; (T - T_0)\, E_{ij} + f(T, T_0) \tag{19}$$

where $\underline{\underline{C}}$ denotes the fourth order elasticity tensor, $\underline{\underline{\alpha}}$ the second order tensor of thermal expansion, T_0 is the reference temperature, and [77]

$$\frac{d^2 f(T, T_0)}{dT^2} = -\frac{\rho C_v}{T}, \tag{20a}$$

whether or not C_v depends on temperature, and

$$f(T, T_0) = -\rho_0\; C_v\; T_0 \left[\frac{T}{T_0}\ln\left(\frac{T}{T_0}\right) - \frac{T}{T_0} + 1\right] \tag{20b}$$

when C_v does not depend on temperature.

The stress-strain relation is then obtained from Eq. (16) as

$$S_{ij} = \rho_0 \left(\frac{\partial \mathcal{F}}{\partial E_{ij}}\right)_T = C_{ijkl}\left[E_{kl} - \alpha_{kl}\; (T - T_0)\right] \tag{21}$$

whether the material properties (i.e. C_{ijkl} and α_{ij}) depend on temperature or not.

The governing equation for the heat convection is then obtained by combining Eqs (13) and (17). This gives the rate of change of the entropy as

$$\dot{\mathcal{S}} = -\frac{\partial^2 \mathcal{F}}{\partial E_{ij}\,\partial T}\dot{E}_{ij} - \frac{\partial^2 \mathcal{F}}{\partial^2 T}\dot{T} \tag{22}$$

or,

$$\begin{aligned}\dot{\mathcal{S}} &= \frac{1}{\rho_0}\left[C_{ijkl}\alpha_{kl}\ \dot{E}_{ij}\right] + \frac{C_v}{T}\dot{T} \\ &+ \frac{1}{\rho_0 T}\left[\left(\frac{\partial \alpha_{ij}}{\partial T}\left(T - T_0\right) - \frac{\partial C_{ijkl}}{\partial T}\,E_{kl}\right)\dot{E}_{ij}\right] \\ &+ \frac{1}{\rho_0 T}\left[\frac{1}{2}\frac{\partial^2 C_{ijkl}}{\partial T^2}\,E_{ij}\ E_{kl} - \frac{\partial^2 \alpha_{ij}}{\partial T^2}\left(T - T_0\right)E_{ij} - 2\,\frac{\partial \alpha_{ij}}{\partial T}\,E_{ij}\right]\dot{T}\end{aligned} \tag{23}$$

Note that this complex expression reduces to the first two terms, appearing in [57,58], when the elasticity tensor and coefficient of thermal expansion are independent of temperature. Combining Eqs (13) and (23) yields finally the desired heat conduction equation

$$\rho_0\, C_v \frac{\partial T}{\partial t} - \frac{\partial}{\partial X_i}\left(k_{ij}^0\ \frac{\partial T}{\partial X_j}\right) = -T\ \alpha_{ij}\,\frac{\partial E_{ij}}{\partial t} + G \tag{24}$$

where G denotes a series of terms involving the derivatives of C_{ijkl} and α_{ij}. Specifically,

$$\begin{aligned}G &= \left(\frac{\partial \alpha_{ij}}{\partial T}\left(T - T_0\right) - \frac{\partial C_{ijkl}}{\partial T}\,E_{kl}\right)\frac{\partial E_{ij}}{\partial t} + \\ &\left[\frac{1}{2}\frac{\partial^2 C_{ijkl}}{\partial T^2}\,E_{ij}E_{kl} - \frac{\partial^2 \alpha_{ij}}{\partial T^2}\left(T - T_0\right)E_{ij} - 2\frac{\partial \alpha_{ij}}{\partial T}\,E_{ij}\right]\dot{T}\end{aligned} \tag{25}$$

The terms lumped in G can be considered as an additional latency effect, beside the first term on the right-hand-side of Eq. (24), as they all involve the strain. They differ from the

classical term (the first term on the right-hand-side of Eq. (24)) by their dependence on the variations of the structural properties with temperature.

The derivation of the governing equations for the generalized coordinates $q_n(t)$ and $\tau_n(t)$ is then achieved by introducing Eqs (9) and (10) in Eqs (11), (12), (18), (21), (24) and (25) and proceeding with a Galerkin approach. This process leads to the differential equations

$$\begin{aligned} &M_{ij}\,\ddot{q}_j + D_{ij}\,\dot{q}_j + K_{ij}^{(1)}\,q_j - K_{ijl}^{(th)}\,q_j\,\tau_l + \\ &\quad K_{ijl}^{(2)}\,q_j\,q_l + K_{ijlp}^{(3)}\,q_j\,q_l\,q_p = F_i + F_{il}^{(th)}\tau_l \end{aligned} \tag{26}$$

and

$$B_{ij}\,\dot{\tau}_j + \tilde{K}_{ij}\tau_j + K_{ijl}^{(st)}\,\dot{q}_j\,\tau_l = P_i + R_{ij}\tau_j\,. \tag{27}$$

Considering in particular the structural reduced order model, note that the coefficients $K_{ij}^{(1)}$, $K_{ijl}^{(2)}$, and $K_{ijlp}^{(3)}$, $K_{ijl}^{(th)}$ and $F_{il}^{(th)}$ are given as [57]

$$K_{mn}^{(1)} = \int_{\Omega_0} \frac{\partial \psi_i^{(m)}}{\partial X_k} C_{iklp} \frac{\partial \psi_l^{(n)}}{\partial X_p}\, d\underline{X} \tag{28}$$

$$K_{mnp}^{(2)} = \frac{1}{2}\left[\hat{K}_{mnp}^{(2)} + \hat{K}_{pmn}^{(2)} + \hat{K}_{npm}^{(2)}\right] \tag{29}$$

$$\hat{K}_{mnp}^{(2)} = \int_{\Omega_0} \frac{\partial \psi_i^{(m)}}{\partial X_j} C_{ijkl} \frac{\partial \psi_r^{(n)}}{\partial X_k} \frac{\partial \psi_r^{(p)}}{\partial X_l}\, d\underline{X} \tag{30}$$

$$K_{msnp}^{(3)} = \frac{1}{2}\int_{\Omega_0} \frac{\partial \psi_i^{(m)}}{\partial X_j} \frac{\partial \psi_i^{(s)}}{\partial X_k} C_{jklw} \frac{\partial \psi_r^{(n)}}{\partial X_l} \frac{\partial \psi_r^{(p)}}{\partial X_w}\, d\underline{X} \tag{31}$$

$$K_{mnp}^{(th)} = \int_{\Omega_0} \frac{\partial \psi_i^{(m)}}{\partial X_k} \frac{\partial \psi_i^{(n)}}{\partial X_j} C_{kjlr} \alpha_{lr} T^{(p)} d\underline{X} \tag{32}$$

$$F_{mn}^{(th)} = \int_{\Omega_0} \frac{\partial \psi_i^{(m)}}{\partial X_k} C_{iklp} \alpha_{lp} T^{(n)} d\underline{X} \quad . \tag{33}$$

Should the material properties depend on temperature, these coefficients will implicitly depend on the temperature distribution since they are dependent on the tensor C_{ijkl} and the product $C_{ijkl}\ \alpha_{kl}$. If the material properties are independent of temperature, these terms are constant throughout the analysis and will only have to be identified once. However, should the properties vary with temperature these findings notably complicate the reduced order modeling formulation as they imply that new coefficients would have to be recomputed at every time step. This difficulty can be bypassed by assuming a polynomial dependence of C_{ijkl} and α_{ij} on the temperature. For example, assuming this dependence being linear, one has

$$C_{ijkl} = C_{ijkl}^{(0)} - C_{ijkl}^{(1)}\ T \tag{34}$$

and

$$\alpha_{ij} = \alpha_{ij}^{(0)} - \alpha_{ij}^{(1)}\ T\ . \tag{35}$$

When propagating the temperature dependence through the terms in Eqs (28) and (32), it becomes more convenient to combine the expressions of $K_{ij}^{(1)}$ and $K_{ij,l}^{(th)}$ in order to determine a single expression for the linear stiffness coefficient's dependence on temperature. Following the substitution of Eqs (34) and (35) into Eqs (28)-(33)

demonstrates that the coefficients, $K_{ijl}^{(2)}$, and $K_{ijlp}^{(3)}$ would be linear in the thermal generalized coordinates τ_i, while $K_{ij}^{(1)}$ and $F_i^{(th)}$ would be cubic in these variables, as

$$K_{ij}^{(1)} = K_{ij,0}^{(1)} - K_{ij,l}^{(1)}\ \tau_l - K_{ij,lm}^{(1)}\tau_l\tau_m - K_{ij,lmn}^{(1)}\tau_l\tau_m\tau_n \tag{36}$$

$$K_{ijl}^{(2)} = K_{ijl,0}^{(2)} - K_{ijl,r}^{(2)}\tau_r \tag{37}$$

$$K_{msnp}^{(3)} = K_{msnp,0}^{(3)} - K_{msnp,l}^{(3)}\tau_l \tag{38}$$

$$F_i^{(th)} = -F_{i,l}^{(th)}\tau_l - F_{i,lr}^{(th)}\tau_l\tau_r - F_{i,lrs}^{(th)}\tau_l\tau_r\tau_s . \tag{39}$$

where

$$K_{mn,0} = \int_{\Omega_0} \frac{\partial\psi_i^{(m)}}{\partial X_k} C_{iklp}^{(0)} \frac{\partial\psi_l^{(n)}}{\partial X_p}\, d\underline{X} \tag{40}$$

$$K_{mn,r} = -\int_{\Omega_0} \left[\frac{\partial\psi_j^{(m)}}{\partial X_K}\frac{\partial\psi_j^{(n)}}{\partial X_i} C_{iklp}^{(o)}\alpha_{lp}^{(0)}T^{(r)} - \frac{\partial\psi_i^{(m)}}{\partial X_K} C_{iklp}^{(1)} \frac{\partial\psi_l^{(n)}}{\partial X_p} T^{(r)} \right] d\underline{X} \tag{41}$$

$$K_{mn,rs} = \int_{\Omega_0} \frac{\partial\psi_j^{(m)}}{\partial X_K}\frac{\partial\psi_j^{(n)}}{\partial X_i} \left[C_{iklp}^{(0)}\alpha_{lp}^{(1)}T^{(r)}T^{(s)} + C_{iklp}^{(1)}\alpha_{lp}^{(0)}T^{(r)}T^{(s)} \right] d\underline{X} \tag{42}$$

$$K_{mn,rsg} = -\int_{\Omega_0} \frac{\partial\psi_j^{(m)}}{\partial X_k}\frac{\partial\psi_j^{(n)}}{\partial X_i} C_{iklp}^{(1)}\alpha_{lp}^{(1)}T^{(r)}T^{(s)}T^{(g)}\, d\underline{X} \tag{43}$$

$$K_{mnp} = \frac{1}{2}\left[\hat{K}_{mnp} + \hat{K}_{pmn} + \hat{K}_{npm}\right] \tag{44}$$

$$\hat{K}_{mnp} = \int_{\Omega_0} \frac{\partial \psi_i^m}{\partial X_j} C_{ijkl}^{(0)} \frac{\partial \psi_r^{(n)}}{\partial X_k} \frac{\partial \psi_r^{(p)}}{\partial X_l} d\underline{X} \tag{45}$$

$$K_{mnp,g} = \frac{1}{2}\left[\hat{K}_{mnp,g} + \hat{K}_{pmn,g} + \hat{K}_{npm,g}\right] \tag{46}$$

$$\hat{K}_{mnp,g} = \int_{\Omega_0} \frac{\partial \psi_i^{(m)}}{\partial X_j} C_{ijkl}^{(1)} T^{(g)} \frac{\partial \psi_r^{(n)}}{\partial X_k} \frac{\partial \psi_r^{(p)}}{\partial X_l} d\underline{X} \tag{47}$$

$$K_{msnp} = \frac{1}{2} \int_{\Omega_0} \frac{\partial \psi_i^{(m)}}{\partial X_j} \frac{\partial \psi_i^{(s)}}{\partial X_k} C_{jklw}^{(0)} \frac{\partial \psi_r^{(n)}}{\partial X_l} \frac{\partial \psi_r^{(p)}}{\partial X_w} d\underline{X} \tag{48}$$

$$K_{msnp,g} = \frac{1}{2} \int_{\Omega_0} \frac{\partial \psi_i^{(m)}}{\partial X_j} \frac{\partial \psi_i^{(s)}}{\partial X_k} C_{jklw}^{(1)} T^{(g)} \frac{\partial \psi_r^{(n)}}{\partial X_l} \frac{\partial \psi_r^{(p)}}{\partial X_w} d\underline{X} \tag{49}$$

$$F_{m,n} = -\int_{\Omega_0} \frac{\partial \psi_i^{(m)}}{\partial X_k} C_{iklr}^{(0)} \alpha_{lr}^{(0)} T^{(n)} d\underline{X} \tag{50}$$

$$F_{m,ng} = \int_{\Omega_0} \frac{\partial \psi_i^{(m)}}{\partial X_k} \left[C_{iklr}^{(0)} \alpha_{lr}^{(1)} + C_{iklr}^{(1)} \alpha_{lr}^{(0)}\right] T^{(n)} T^{(g)} d\underline{X} \tag{51}$$

$$F_{m,ngh} = -\int_{\Omega_0} \frac{\partial \psi_i^{(m)}}{\partial X_k} C_{iklr}^{(1)} \alpha_{lr}^{(1)} T^{(n)} T^{(g)} T^{(h)} d\underline{X} \tag{52}$$

In Eq. (27), B_{ij} and $\tilde{K}_{ij}$ are the elements of the capacitance and conductance matrices of the reduced order model and $K_{ijl}^{(st)}$ is a linear latency term, dual of $K_{ijl}^{(th)}$. Further, the term P_i denotes the source term associated with the boundary conditions and the external flux while R_{ij} involves latency and change of geometry effects [16]. $K_{ijl}^{(st)}$

and R_{ij} are dependent on the temperature distribution. They also represent the feedback effect of the structural deformations on the temperature distribution. This effect is generally recognized as small for small to medium deformations and thus $K_{ijl}^{(st)}$ and R_{ij} will be neglected in the present analysis. The resulting heat conduction equation is

$$B_{ij}\ \dot{\tau}_j + \tilde{K}_{ij}\tau_j = P_i\ . \tag{53}$$

3.2 Basis Selection

3.2.1 Structural Basis

The selection of the structural basis functions $\underline{\psi}^{(n)}$ represents a key challenge of the reduced order modeling strategy: if the structural response is not well represented within this basis, the corresponding prediction of the reduced order model will in general be poor. The modes/basis functions needed for a nonlinear problem are certainly expected to include those used for the corresponding linear problem, but others are also anticipated to model the difference in physical behavior induced by the nonlinearity. This situation is particularly clear in shell-like structures subjected to transverse loadings in which the linear response is predominantly transverse while the tangential/in-plane displacement field plays a fundamental role (the "membrane-stretching" effect, see [29,38,39] for discussion) in large motions.

This issue was addressed in [54] through the inclusion in the basis of an additional set of basis functions referred to as dual modes aimed at capturing the membrane stretching effects. The key idea in this approach is to first subject the structure to a series

of "representative" static loadings, and determine the corresponding *nonlinear* displacement fields. Then, extract from them additional basis functions, the "dual modes", to append to the linear basis, i.e. the modes that would be used in the linear case. It was argued in [54] that the representative static loadings should be selected to excite primarily the linear basis modes and, in fact, in the absence of geometric nonlinearity (i.e. for a linear analysis) should only excite these modes. i.e. the applied load vectors $\underline{F}_{FE}^{(m)}$ on the structural finite element model should be such that the corresponding linear static responses are of the form

$$\underline{u}^{(m)} = \sum_i \alpha_i^{(m)} \ \underline{\psi}^{(i)} \tag{54}$$

which occurs when

$$\underline{F}_{FE}^{(m)} = \sum_i \alpha_i^{(m)} K_{FE}^{(1)} \underline{\psi}^{(i)} \tag{55}$$

where $\alpha_i^{(m)}$ are coefficients to be chosen with *m* denoting the load case number. A detailed discussion of the linear combinations to be used is presented in [54] but, in all validations carried out, it has been sufficient to consider the cases

$$\underline{F}_{FE}^{(m)} = \alpha_i^{(m)} K_{FE}^{(1)} \underline{\psi}^{(i)} \quad \text{i = dominant mode} \tag{56}$$

and

$$\underline{F}_{FE}^{(m)} = \frac{\alpha_i^{(m)}}{2} K_{FE}^{(1)} \left[\underline{\psi}^{(i)} + \underline{\psi}^{(j)} \right] \qquad i \text{ = dominant mode, } \ j \neq i \tag{57}$$

where a "dominant" mode is loosely defined as one expected to provide a large component of the panel response to the physical loading. The ensemble of loading cases

considered is formed by selecting several values of $\alpha_i^{(m)}$ for each dominant mode in Eq. (56) and also for each mode $j \neq i$ in Eq. (57). Note further that both positive and negative values of $\alpha_i^{(m)}$ are suggested and that their magnitudes should be such that the corresponding displacement fields $\underline{u}^{(m)}$ range from near linear cases to some exhibiting a strong nonlinearity.

The next step of the basis construction is the extraction of the nonlinear effects in the obtained displacement fields, which is achieved by removing from the displacements fields their projections on the linear basis. Finally, a proper orthogonal decomposition (POD) analysis of each set of "nonlinear responses" is then sequentially carried out to extract the dominant features of these responses which are then selected as dual modes, see [54] for full details.

The above dual mode construction has been very successfully applied to various beam and plate structural models, e.g. see [39,54-58,62-65], to capture the nonlinear interaction, both static and dynamic, between transverse and "in-plane" motions. Its application to the panel of Fig. 1 did provide a basis that represented much better the nonlinear response, especially in the in-plane (tangential) direction, than the one based on the linear modes but yet not well enough to obtain an accurate reduced order model prediction of the full order Nastran results. This observation suggested that the load cases of Eq. (56) and (57) do provide a very valuable platform to identify the nonlinear effects, but it also demonstrated that other, smaller components, are also present.

In addition to the dual modes, "tangent duals" were added to the basis in order to capture the remaining components of the displacement. First, the tangent stiffness matrix is acquired at the displacements $\underline{u}^{(m)}$ induced by the loading of Eqs (56) and (57). Next, a generalized eigenvector analysis of each matrix $\hat{K}^{(T)}(\underline{u}^{(m)})$ was performed yielding the vectors $\underline{\gamma}_j^{(m)}$ such that

$$\hat{K}^{(T)}(\underline{u}^{(m)})\,\underline{\gamma}_j^{(m)} = \lambda_j^{(m)} M_{FE}\,\underline{\gamma}_j^{(m)}. \tag{58}$$

Next, the eigenvectors $\underline{\gamma}_j^{(m)}$ that are most significantly excited by the loading were retained and made orthogonal to the linear and dual modes in the basis. Finally, a POD analysis of the ensemble of modes was carried out to extract the novel information in the eigenvectors $\underline{\gamma}_j^{(m)}$.

3.2.2 Thermal Basis

For the beam, the thermal basis functions are a product of a through thickness component and a spanwise component. The spanwise component of the basis is the thermal eigenvector and the through thickness component is either a linear or cubic function of the through thickness location.

For the panel, the thermal basis functions are composed of eigenvectors of the generalized eigenvalue problem involving the capacitance and conductance matrices at reference temperature. Additionally, the two-way coupled analysis required that the thermal basis be enhanced. Two different approaches were considered. First, an adaptive

approach was developed in order to construct the basis as the simulation was carried out. This involved the solution of an auxiliary problem with similarities to the full order, nonlinear thermal problem. The solutions of the auxiliary problem would then be used as a basis for the thermal ROM. Second, an alternative strategy to developing a thermal basis for the two-way coupled problem involved simulating the two-way coupling between the structural and thermal problem under a set of conditions which were representative of the conditions experienced during the ascent trajectory analysis. Structural displacements according to the linear structural modes were imposed while a constant Mach free stream flow was applied. The aerothermal analysis was performed in order to predict the heat flux acting on the panel under these conditions, and this flux was then applied to an unheated panel and a thermal simulation was then carried out. The resulting temperature fields acted as enrichments to the thermal basis which captured the coupling between the structural and thermal problems.

3.3 Identification of the Parameters of the Reduced Order Model

3.3.1 Structural Parameters

3.3.1.1 No Temperature Present

While Eqs (36)-(48) provide exact expressions for the coefficients of the structural reduced order model, they are not in a form that is convenient for evaluation from a finite element model in which only discretized values of the modes are available. This observation has led, as in prior investigations, to the consideration of *indirect* methods for the estimation of the coefficients from a series of static finite element

computations. In the absence of temperature variations, the STEP identification strategy of the coefficients $K_{ij}^{(1)}$, $K_{ijl}^{(2)}$, and $K_{ijlp}^{(3)}$ as initially proposed by Muravyov and Rizzi [34] and modified by [54] has often been utilized.

In the STEP algorithm, the entire displacement field of the structure is imposed and the required static force distribution is obtained from the finite element code. The corresponding modal forces are then evaluated by projection on the basis. Appropriately selecting the displacement fields to be imposed can lead to a particularly convenient identification of the stiffness coefficients. Specifically, the imposition of displacements proportional to the basis function $\underline{\psi}^{(n)}$ only, i.e.

$$\underline{u} = q_n \ \underline{\psi}^{(n)} \qquad \underline{\hat{u}} = \hat{q}_n \ \underline{\psi}^{(n)} \qquad \underline{\tilde{u}} = \tilde{q}_n \ \underline{\psi}^{(n)} \tag{59}$$

leads from Eq. (3) to the 3 sets of equations

$$\begin{aligned} &K_{in}^{(1)} \ q_n + K_{inn}^{(2)} q_n^2 + K_{innn}^{(3)} \ q_n^3 = F_i \\ &K_{in}^{(1)} \ \hat{q}_n + K_{inn}^{(2)} \hat{q}_n^2 + K_{innn}^{(3)} \ \hat{q}_n^3 = \hat{F}_i \\ &K_{in}^{(1)} \ \tilde{q}_n + K_{inn}^{(2)} \tilde{q}_n^2 + K_{innn}^{(3)} \ \tilde{q}_n^3 = \tilde{F}_i \end{aligned} \tag{60}$$

in which no sum over the index *n* is to be understood and for *i* = 1, ..., *M*. Moreover,

$$F_i = \underline{\psi}^{(i)T} \underline{F}, \quad \hat{F}_i = \underline{\psi}^{(i)T} \underline{\hat{F}}, \quad \tilde{F}_i = \underline{\psi}^{(i)T} \underline{\tilde{F}} \tag{61}$$

where $\underline{F}$, $\underline{\hat{F}}$, and $\underline{\tilde{F}}$ are the force distributions needed to induce the three displacements fields of Eq. (59). In fact, these 3 sets of equations permit the direct evaluation of the

coefficients $K_{in}^{(1)}$, $K_{inn}^{(2)}$, and $K_{innn}^{(3)}$ for all *i*. Repeating this effort for $n = 1, ..., M$ thus yields a first set of stiffness coefficients.

Proceeding similarly but with combinations of two basis functions, i.e.

$$\underline{u} = q_n \, \underline{\psi}^{(n)} + q_m \, \underline{\psi}^{(m)} \quad m \geq n \tag{62}$$

leads to equations involving the three coefficients $K_{inm}^{(2)}$, $K_{innm}^{(3)}$, and $K_{inmm}^{(3)}$. Thus, imposing three sets of displacements of the form of Eq. (62) provides the equations needed to also identify $K_{inm}^{(2)}$, $K_{innm}^{(3)}$, and $K_{inmm}^{(3)}$.

Finally, imposing displacement fields as linear combinations of three modes, i.e.

$$\underline{u} = q_n \, \underline{\psi}^{(n)} + q_m \, \underline{\psi}^{(m)} + q_r \, \underline{\psi}^{(r)} \quad r \geq m \geq n \ , \tag{63}$$

permits the identification of the remaining unknown coefficients, i.e. $K_{inmr}^{(3)}$.

An alternate approach has also been proposed [65], which relies on the availability of the final *tangent stiffness matrix* for each imposed displacement case. The advantage of this approach is that an *M* x *M* matrix is obtained for each solution and thus a reduction of the computational effort to $O(M^2)$ vs. $O(M^3)$ for the algorithm of Eqs (59)-(63) is achieved. The specific details of this algorithm are developed below.

Note first that the *iu* component of the reduced order tangent stiffness matrix can be derived from the cubic stiffness operator of Eq. (26) as

$$K_{iu}^{(T)} = \frac{\partial}{\partial q_u}\left[K_{ij}^{(1)} q_j + K_{ijl}^{(2)} q_j q_l + K_{ijlp}^{(3)} q_j q_l q_p\right]$$
$$= K_{iu}^{(1)} + \left[K_{iju}^{(2)} + K_{iuj}^{(2)}\right] q_j + \left[K_{ijlu}^{(3)} + K_{ijul}^{(3)} + K_{iujl}^{(3)}\right] q_j q_l \tag{64}$$

It was proposed in [28] to determine the stiffness coefficients $K_{ij}^{(1)}$, $K_{ijl}^{(2)}$, and $K_{ijlp}^{(3)}$ by imposing the matching, for a series of deformed configurations, of the reduced order tangent stiffness matrix with the projection on the basis of its finite element counterpart $\hat{K}^{(T)}$. That is,

$$K^{(T)}(\underline{q}^{(p)}) = \Psi^T \hat{K}^{(T)}(\underline{u}^{(p)})\,\Psi \tag{65}$$

where the displacement fields $\underline{u}^{(p)} = \Psi \underline{q}^{(p)}$, for a series of p = 1, ..., P deformed configurations.

The first such configuration is the undeformed one, i.e. $\underline{u} = \underline{0}$, for which $K^{(T)}$ is simply the linear stiffness matrix $K^{(1)}$ and thus

$$K^{(1)} = \Psi^T \hat{K}^{(T)}(\underline{0})\,\Psi \tag{66}$$

The next set of deformed configurations, $\underline{u}^{(p)}$, selected here are those of the imposed displacement scheme, Eqs (59) and (62). Consider first the situation in which the imposed displacement is along a single basis function, i.e. $\underline{u} = q_j\ \underline{\psi}^{(j)}$. The corresponding ROM tangent stiffness matrix can then be written as (no sum on j)

$$K_{iu}^{(T)} = K_{iu}^{(1)} + \left[K_{iju}^{(2)} + K_{iuj}^{(2)}\right] q_j + \left[K_{ijju}^{(3)} + K_{ijuj}^{(3)} + K_{iujj}^{(3)}\right] q_j^2 \tag{67}$$

In this regard, note that the elements $K^{(2)}_{ijl}$ and $K^{(3)}_{ijlp}$ can be assumed to be zero unless $p \geq l \geq j$ and thus the above equation is equivalent to three conditions

$$\left[\Psi^T \hat{K}^{(T)} \Psi\right]_{iu} = K^{(1)}_{iu} + K^{(2)}_{iju} q_j + K^{(3)}_{ijju} q^2_j \qquad j < u$$

$$\left[\Psi^T \hat{K}^{(T)} \Psi\right]_{iu} = K^{(1)}_{iu} + 2\,K^{(2)}_{iuu} q_u + 3\,K^{(3)}_{iuuu} q^2_u \qquad j=u \tag{68a,b,c}$$

$$\left[\Psi^T \hat{K}^{(T)} \Psi\right]_{iu} = K^{(1)}_{iu} + K^{(2)}_{iuj} q_j + K^{(3)}_{iujj} q^2_j \qquad j > u$$

from which the coefficients $K^{(2)}_{ijl}$, $K^{(3)}_{ijjl}$, and $K^{(3)}_{ijll}$ can be estimated given the linear stiffness coefficients obtained from Eq. (63).

To complete the identification of the reduced order model, it remains to evaluate the coefficients $K^{(3)}_{ijlu}$ for $j \neq l$, $j \neq u$, and $u \neq l$. They can be evaluated from the knowledge of $K^{(T)}_{iu}$ corresponding to a displacement field which involves both basis functions j and l, i.e. of the form of Eq. (61). Then, $K^{(T)}_{iu}$ is given by Eq. (64) in which no summation on j and l applies. Specifically, for $u > l > j$, one has

$$\begin{aligned}\left[\Psi^T \hat{K}^{(T)} \Psi\right]_{iu} = K^{(1)}_{iu} &+ \left[K^{(2)}_{iju}\, q_j + K^{(2)}_{ilu}\, q_l\right] \\ &+ \left[K^{(3)}_{ijlu}\, q_j\, q_l + K^{(3)}_{ijju}\, q^2_j + K^{(3)}_{illu}\, q^2_l\right]\end{aligned} \tag{69}$$

in which all terms are known except $K^{(3)}_{ijlu}$.

Lastly, the remaining parameters of the model of Eq. (26), i.e. the modal masses M_{ij}, damping coefficients D_{ij}, and modal forces F_i are determined from the finite element model of the structure as follows

$$M_{ij} = \underline{\psi}^{(i)T} \underline{\underline{M}}_{FE} \underline{\psi}^{(j)} \tag{70}$$

$$D_{ij} = \underline{\psi}^{(i)T} \underline{\underline{D}}_{FE} \underline{\psi}^{(j)} \tag{71}$$

$$F_i = \underline{\psi}^{(i)T} \underline{F}_{FE} \tag{72}$$

where $\underline{\underline{M}}_{FE}, \underline{\underline{D}}_{FE}$, and $\underline{F}_{FE}$ are the global mass matrix, damping matrix, and forces applied to the full finite element model.

Note finally, that the modal forces F_i will in general be affected by the "pull back" operation. However, this issue was not addressed here because the displacements of the beams and panels considered in this investigation did not exceed a few thicknesses.

3.3.1.2 Temperature Present – Temperature Independent Properties

So far, a method for determining the coefficients in the absence of a nonzero temperature field has been provided. When the structure is subjected to thermal loading, and when the elasticity tensor and coefficient of thermal expansion do not vary with temperature, the linear stiffness term has a linear dependence on temperature. In fact, the linear stiffness can be expressed as follows:

$$K_{ij}^{(1)} = K_{ij,0}^{(1)} + K_{ij,r}^{(1)} \tau_r \tag{73}$$

with $K_{ij,0}^{(1)}$ being the linear stiffness in the absence of temperature and $K_{ij}^{(1)}$ being the linear stiffness in the presence of temperature. In order to determine the value of $K_{ij,r}^{(1)}$, temperature fields proportional to each thermal mode as

$$T(\underline{X}) = \tau_r T^{(r)}(\underline{X}) \tag{74}$$

are imposed on the structure. With each temperature field applied, $K_{ij}^{(1)}$ could be found using either of the methods previously described. Since τ_r is a known scalar value, the only unknown left is $K_{ijl,r}^{(2)}$, which is directly solved for in Eq. (73). The thermal moment term on the right hand side of Eq. (26) is determined as

$$F_{il}^{(th)} = \underline{\psi}^{(i)T} \underline{\underline{F}}_{FE}^{(th)} \ . \tag{75}$$

$\underline{\underline{F}}_{FE}^{(th)}$ is the force induced by the application of each thermal mode to the structure.

3.3.1.3 Temperature Present – Temperature Dependent Properties

For the beam model the elasticity tensor and coefficient of thermal expansion will vary with temperature. In order to determine the temperature dependent terms given in Eqs (36)-(39), a method similar to the one specified above will be used. A series of temperature fields, which will result from combinations of thermal modes, will be imposed on the system, and the desired stiffness and force terms will be acquired using the methodology specified above. A system of linear equations will result in which the temperature dependent parameters of Eqs (36)-(39) will be solved for.

In all these equations, the terms with a subscript of 0 denote parameters that are not connected to the thermal generalized coordinates. These terms are found using the method described in Section 3.3.1.1, in which the reference temperature is enforced on the structure, with the elasticity tensor being independent of temperature and the coefficient of thermal expansion being equal to zero.

As seen in Eqs (37)-(38) the cubic and quadratic stiffness terms depend linearly on temperature, due to the presence of the elasticity tensor. Looking specifically at the quadratic stiffness, Eq. (37) can be rearranged as follows:

$$\left(K_{ijl}^{(2)} - K_{ijl,0}^{(2)}\right) = K_{ijl,r}^{(2)}\tau_r \tag{76}$$

In order to determine the value of $K_{ijl,r}^{(2)}$, temperature fields proportional to each thermal mode as

$$T(\underline{X}) = \tau_r T^{(r)}(\underline{X}) \tag{77}$$

are imposed on the structure, with the elasticity tensor varying with temperature. With each temperature field applied, the method described in Section 3.3.1.1 was applied in order to find $K_{ijl}^{(2)}$. Since τ_r is a known scalar value, the only unknown left is $K_{ijl,r}^{(2)}$, which is directly solved for. In the same way, the terms that define the cubic stiffness coefficient, $K_{ijlp,r}^{(3)}$,can be found.

The linear stiffness coefficients and thermal moment terms have a cubic dependence on temperature. Further, they can be rearranged to have the same form as

specified in Eq. (60) but with the thermal generalized coordinates τ_j as opposed to their structural counterparts q_j, e.g.

$$\left(K_{ij}^{(1)} - K_{ij,0}^{(1)}\right) = -K_{ij,l}^{(1)}\,\tau_l - K_{ij,lm}^{(1)}\tau_l\tau_m - K_{ij,lmn}^{(1)}\tau_l\tau_m\tau_n \quad . \tag{78}$$

Based on the similarity between Eqs (60) and (78), temperature fields will now be applied as the displacement fields were applied in the STEP method. Thus, the first step is to estimate the parameters $K_{ij,l}^{(1)}$, $K_{ij,ll}^{(1)}$, and $K_{ij,lll}^{(1)}$. Applying a temperature field proportional to a single thermal basis function, i.e.

$$T^{(r)}\left(\underline{X}\right) = \tau_l^{(r)} T^{(l)}\left(\underline{X}\right) \qquad r = 1,2,3 \tag{79}$$

for each value of *l* in turn results in

$$\left(K_{ij}^{(1)} - K_{ij,0}^{(1)}\right) = -K_{ij,l}^{(1)}\,\tau_l - K_{ij,ll}^{(1)}\tau_l\tau_l - K_{ij,lll}^{(1)}\tau_l\tau_l\tau_l \tag{80}$$

As each temperature field is applied to the system, which has both the elasticity tensor and the coefficient of thermal expansion varying linearly with temperature, the method described in 3.3.1.1 is again applied in order to determine $K_{ij}^{(1)}$. Since τ_l is a known scalar, what results is a system of 3 linear equations in which there are 3 unknowns, $K_{ij,l}^{(1)}$, $K_{ij,ll}^{(1)}$, and $K_{ij,lll}^{(1)}$.

The next step is the estimation of the parameters $K_{ij,lr}^{(1)}$, $K_{ij,lrr}^{(1)}$, and $K_{ij,llr}^{(1)}$, for $l \neq r$, which appear in the model through the generalized coordinates τ_r and τ_l. These parameters can be found following a similar procedure as the first step but with the application of the temperature fields that are of the form

$$T^{(p)}(\underline{X}) = \tau_l^{(p)} T^{(l)}(\underline{X}) + \tau_r^{(p)} T^{(r)}(\underline{X}) \qquad p = 1,2,3. \tag{81}$$

The third and last step involves the determination of the parameters $K^{(3)}_{ij,lrs}$, for *l*, *r*, and *s* all different. The temperature field imposed on the system in order to find this parameter is of the following form.

$$T(\underline{X}) = \tau_l T^{(l)}(\underline{X}) + \tau_r T^{(r)}(\underline{X}) + \tau_s T^{(s)}(\underline{X}) \tag{82}$$

The temperature dependent parameters of Eq. (39), which describes the thermal moment term, can be found in the same manner.

3.3.2 Thermal Parameters

When the specific heat and thermal conductivity do not change with temperature the components of Eq. (27) are evaluated in a straightforward manner, as shown in Eqs (83) and (84),

$$B_{ij} = T^{(i)} \underline{\underline{B}}_{FE} T^{(j)} \tag{83}$$

$$\tilde{K}_{ij} = T^{(i)} \underline{\underline{\tilde{K}}}_{FE} T^{(j)}, \tag{84}$$

where $\underline{\underline{B}}_{FE}$ and $\underline{\underline{\tilde{K}}}_{FE}$ are the capacitance and conductance matrix from the finite element model.

A different approach has to be taken to determine the components of the capacitance and conductance matrix when the specific heat and thermal conductivity change with temperature, as it does with the panel. With regards to specific heat, it should first be noted that this is an isotropic property. With this in mind, the capacitance matrix was found for every individual element at the reference temperature. The average

temperature was found for each element and then the ratio of the current value of specific heat to the value of specific heat at reference temperature was found. The capacitance matrix for each element was multiplied by its associated ratio of specific heat, and then all the elemental capacitance matrices were assembled into the global matrix.

Thermal conductivity is isotropic in the elements that comprise the stiffeners of the panel, which is why the procedure just described was applied to these elements. However, thermal conductivity is not an isotropic property in the elements that comprise the skin of the panel, since the inplane conductivity changes with temperature while the through thickness conductivity does not. Because of this, a database of conductance matrices of a single element was found at every temperature listed in Table 3, which depicts the relationship between the specific heat with temperature. Due to the uniformity of the shape of the skin elements, only one master element was needed. Within the conductance matrix of this master element there are only six unique numerical values. The average temperature was found for each skin element and the element's conductance matrix was found by interpolating the values of the six unique components of the master element matrix between the temperatures listed in Table 3. This was done for every skin element and then the global conductance matrix was assembled. Then, the modal conductance and capacitance matrices could be determined, as shown in Eqs (85) and (86).

$$B_{ij} = T^{(i)} \underline{\underline{B}}_{global} T^{(j)} \tag{85}$$

$$\tilde{K}_{ij} = T^{(i)} \underline{\underline{\tilde{K}}}_{global} T^{(j)} \tag{86}$$

Finally, the force term, P_i, is composed of thermal loads stemming from the aerodynamics, as well as radiation. The convection boundary condition described by Eq. (4) can be rewritten as

$$Q_{aero} = h_{conv} T_{aw} - h_{conv} T_w \quad . \tag{87}$$

The term multiplying wall temperature, T_w, was moved to the left hand side of the thermal governing equation and added to the conductance matrix. The term involving adiabatic wall temperature, T_{aw} , was evaluated for each element. This term was then added to the flux from radiation, which was calculated according to Eq. (5) using the average temperature of each element. The element flux was then converted to nodal flux. In order to do this a unit value of heat flux was applied to an element on the skin of the finite element model while its temperature was held constant. The nodal reaction flux to this unit flux acting on the element was then acquired. The total flux acting on each element was then used to scale the nodal reaction flux and these values from each element were then assembled into a global nodal flux vector, $\underline{P}_{global}$. Then, the modal flux was determined using Eq. (88).

$$P_i = \underline{T}^{(i)T} \underline{P}_{global} \tag{88}$$

CHAPTER 4 – RESULTS

4.1 Results for the Thermal ROM of the Representative Panel

4.1.1 One-Way Coupled Analysis

The first issue to be addressed is the construction of the thermal reduced order basis. The temperature fields which are to be represented are those obtained in the one and two-way coupled, constant rate ascent trajectory analysis of [10] with the 10% spring boundary condition (maximum), in which the *flow and its convection only act on the skin (top) of the panel*. Accordingly, there is no heating taking place on the stiffeners and the heat must thus flow on them from the fold lines, where skin and stiffeners meet, to the free ends. Further, in the one-way coupled analysis, the heat convection is fairly constant through the skin resulting in a reasonably uniform temperature distribution. These comments are well reflected on the temperature distribution of Fig. 3(a) which was obtained after 300 s of analysis.

Note that Fig. 3 is a "developed" 2D image of the entire panel. The stiffeners on the side have been "folded" upwards so that they lie in plane with the skin of the panel. The *y* domain from 0 to 10 inches represents the skin of the panel, while the regions less than 0 and greater than 10 represent the two stiffeners. The flow moves from left to right. The variation of temperature in the direction of the flow is mild. It is also in the *y* direction except in the stiffener domains where it is severe.

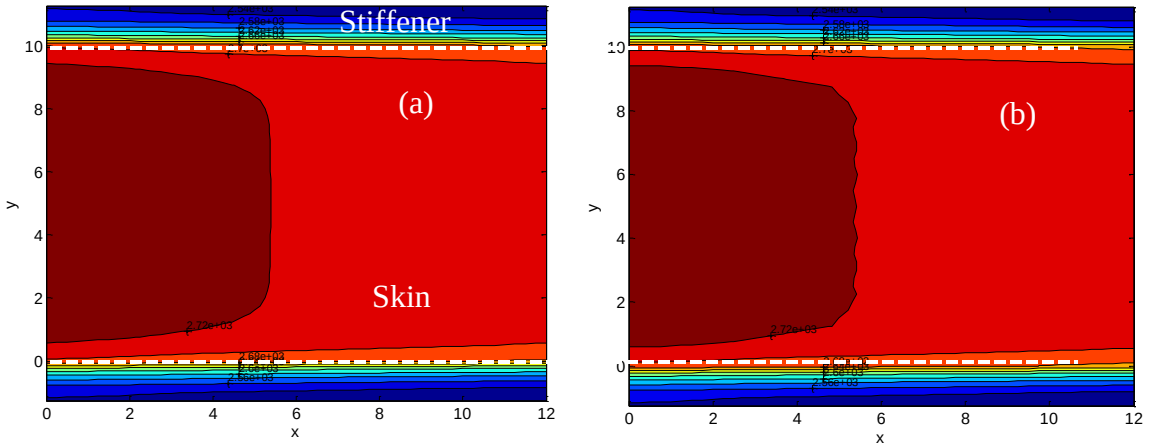

Figure 3. Temperature on Panel at Last Time Step. Results From Nastran (a) and Thermal Reduced Order Model (b)

As broadly described above, the eigenvectors of the generalized conductance capacitance eigenvalue problem were first chosen to construct a thermal basis to represent the temperature fields occurring in the one-way coupled analysis. The sufficiency of the basis was assessed by projecting the desired temperature field of Figure 3(a) onto the thermal basis. It was found, however, that the dominant eigenvectors did not produce fast enough convergence. This is not too surprising, given the sharp temperature gradient at the stiffener that would be very difficult for these eigenvectors to represent.

The differences between the boundary conditions of the skin and stiffeners, specifically the skin's exclusive exposure to the flow, necessitates that the basis account for the interaction of the aerodynamics and the heat convection acting on the exposed surface. So, in addition to the eigenvectors of the entire panel, another set of modes was generated from the conductance-capacitance generalized eigenvalue problem of the panel when the fold line connecting the skin and the panel was constrained to constant temperature.

In the end, 20 eigenvectors from the full model and 7 eigenvectors from the constrained model were selected for the final thermal basis for the one-way coupled analysis, totaling 27 modes. Figure 3 (b) shows the temperature field representation error,

$$\varepsilon_{rep,T} = \frac{\left\| \underline{T} - \underline{T}_{proj} \right\|}{\left\| T \right\|}, \tag{89}$$

obtained by subtracting from the temperature distribution at six points in the analysis its projection on the thermal basis, as in Eq. (89). It should be noted that the average temperature at each timestep is subtracted out of the temperature fields of Eq. (89). This was done so that the large average temperature would not inhibit the observation of errors in temperature variations about the mean temperature. This error was computed from the data of [10] at every 10 seconds of the 300 seconds of analysis. The error in the very beginning is large relative to the error throughout the rest of the analysis, however, significant error in the temperature fields in the beginning of the analysis proved to have little influence over the prediction of temperature and displacements throughout the rest of the analysis, which are a higher priority considering the increased temperature and displacements observed at these later times.

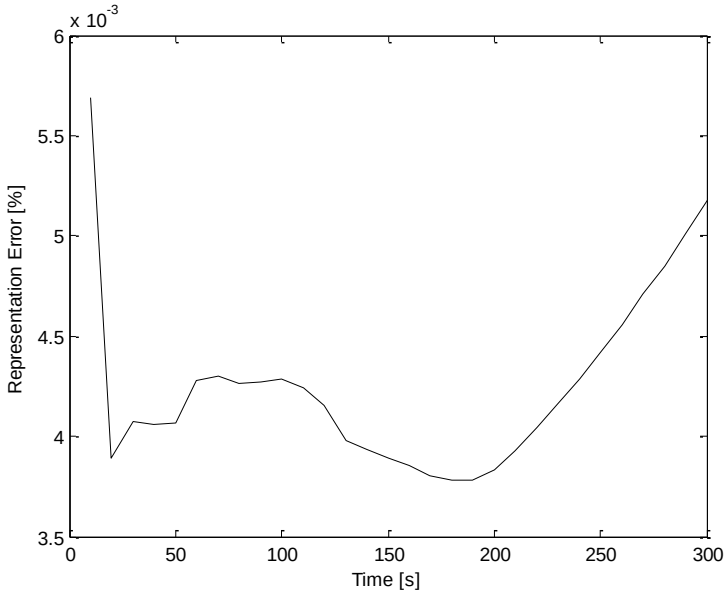

Figure 4. Representation Error of 27 Mode Basis Over 300 Second Analysis

A one-way coupled thermal simulation of the constant rate ascent trajectory analysis was performed using the thermal reduced order model for 300 seconds and resulted in errors shown in Fig. 5, when comparing the predicted results to the results in [10] at every 10 seconds of analysis. The error for the final time step is 1.0% and the full temperature field predicted by the ROM can be seen in Fig. 3(b).

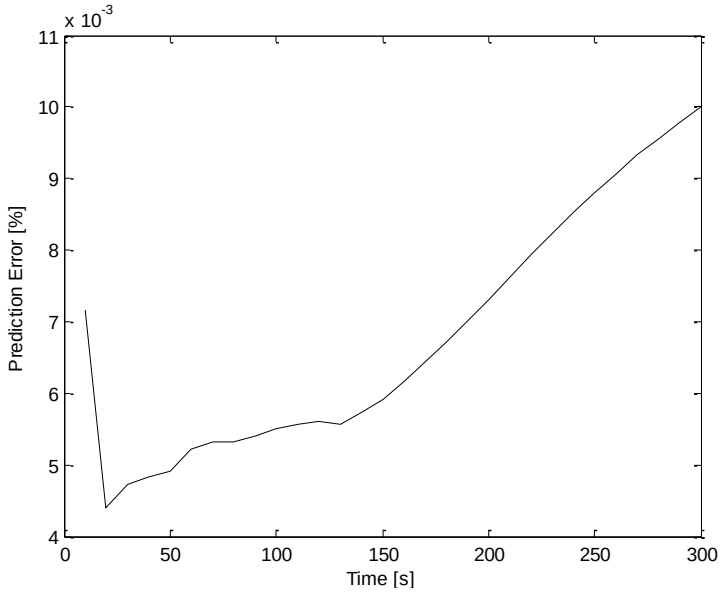

Figure 5. Prediction Error of 27 Mode Thermal Model at Every 10 Seconds

4.1.2 Two-Way Coupled Analysis: Adaptive Basis

The 27-mode basis constructed above for the one-way coupled case was assessed to represent the temperature distribution of the two-way problem with full aero-thermo-structural interaction. This assessment was carried out by projecting the known results from [10] onto the thermal ROM basis. Shown in Fig. 6 are the corresponding norm errors, i.e. representation errors.

Interestingly, the representation error remains very low for approximately the first third of the time history and thus the single discipline basis would be fully appropriate in that time period to predict the temperature even in this multidisciplinary situation. Yet, with the increasing flow speed and thus temperature, the structural deformations grow and start to affect sufficiently the flow and, in turn, the convection leading to a *qualitative* change in temperature distribution. This behavior coincides with the rapid increase in the representation errors, i.e. the temperature distribution is no longer well representable by the 27-modes basis. Given the complexity of this interaction, it is proposed here to devise a strategy to adapt the thermal basis to the changing physics of the problem induced by the evolving aero-thermo-structural coupling.

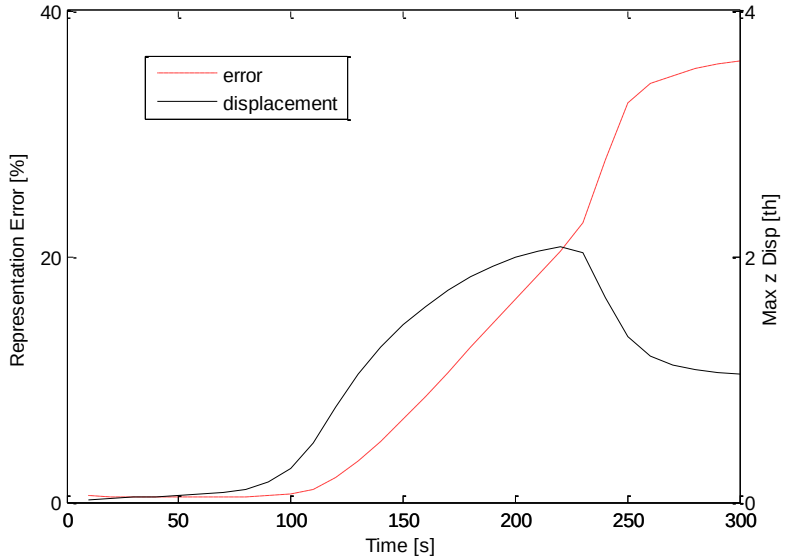

Figure 6. Representation Error of Thermal ROM Basis for Two-Way Coupled Analysis and Time History of Maximum Panel Displacement Into the Flow.

Fig. 7 (a) and (b) show the temperature fields predicted after 300 seconds of the one-way and two-way coupled analysis. Clearly, there are dramatic differences between the one and two-way coupled analyses, with the latter generating a more complex temperature distribution than its one-way counterpart. Note again that the panel has been "flattened" so that the stiffeners have been brought up to the same plane as the skin, producing a 2-D presentation of the 3-D structure. The regions above y=10 and below y=0 are the stiffeners, and the flow moves from left to right.

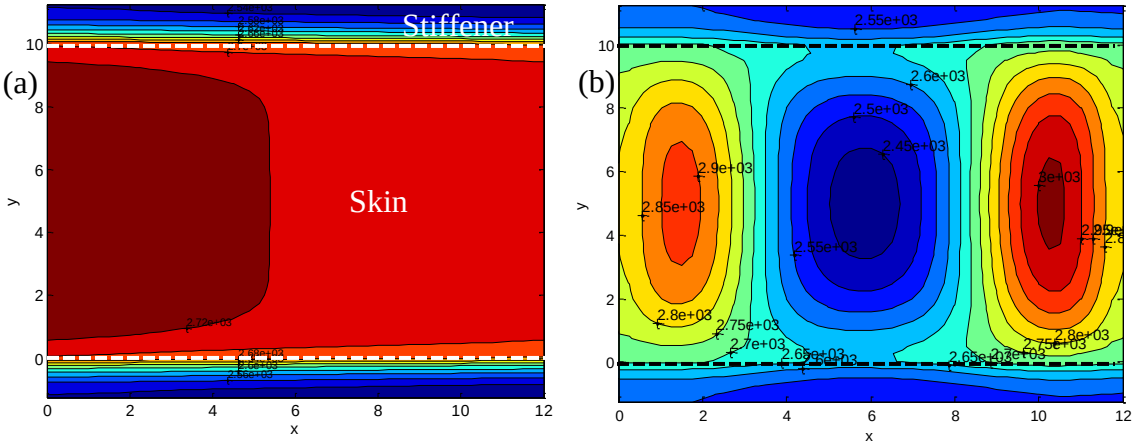

Figure 7. Temperature of the Panel After 300 Seconds of (a) One-Way Coupled Analysis and (b) Two-Way Coupled Analysis.

Adapting the thermal basis requires having relevant data. Yet, it is also desired not to solve the full order problem or not solve it often, as not to increase significantly the cost of the reduced order modeling computations. To address this situation, it is proposed here to proceed with the adaptation on a simpler yet similar problem, referred to as the auxiliary problem. It is proposed here that this auxiliary problem be of the heat conduction on the panel *without radiation* and *with constant conduction and capacitance properties*. The equations governing this problem are thus linear and contain constant coefficients, i.e. they have a very efficient solution. The purpose of the auxiliary problem will be to determine the changes to the basis functions to be carried out.

The following discussion will then focus on (1) demonstrating the validity of the proposed auxiliary problem and (2) investigating how and how often the basis should be updated. To validate the auxiliary problem, an unsteady analysis of it was performed over the same time span (300 seconds) as the complete analysis. Snapshots of the temperature fields produced by this linear analysis with the fluxes obtained from the full order analysis of [10] were generated and were projected on the basis. If the auxiliary problem is a meaningful substitute for the full, nonlinear problem, the residuals of these linear analyses should contain meaningful information on how to modify the thermal basis functions.

This information was extracted through a proper orthogonal decomposition (POD) of the residuals and the corresponding dominant eigenvectors were determined and assessed as potential basis functions for the reduction of the representation error of

the *full* (two-way coupled) temperature distribution. If this process leads to a good representation of this latter temperature field, then the auxiliary problem is indeed appropriate for the adaptation of the basis.

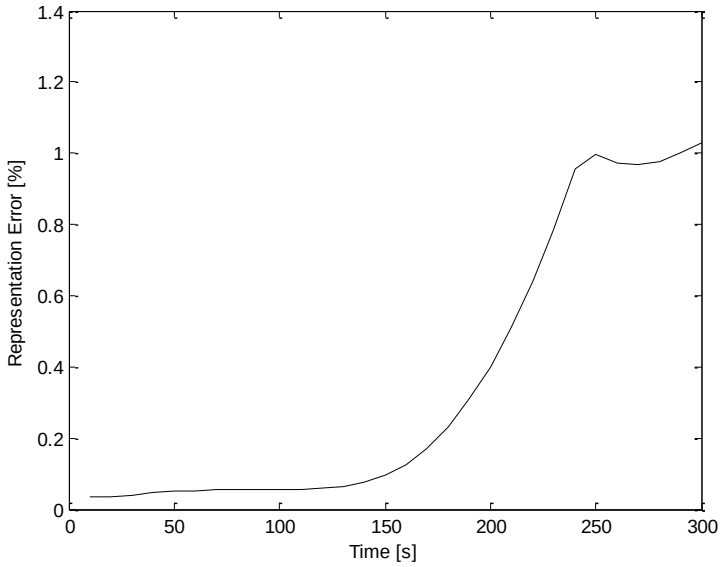

Figure 8. Representation Error of Enhanced Thermal ROM Basis for Two-Way Coupled Analysis.

Shown in Fig. 8 is the representation error occurring at every 10 seconds of the 300 second analysis when the 30 most dominant POD eigenvectors are added to the original 27 thermal modes. The error of 35% observed in Fig. 6 has now been reduced to approximately 1% demonstrating that the linear analysis does have the capability to produce enrichments to the basis that can capture the desired temperature fields. It is thus concluded, for this problem at least, that the linear conduction problem with temperature independent properties is an appropriate auxiliary problem.

The next question to be addressed is how and how often the thermal basis should be adapted. Presented here are a number of options that were evaluated. In all of them, the auxiliary problem was solved only at regular time intervals and for a few consecutive

time steps. That is, the auxiliary problem is only performed at specific windows of time along the flight trajectory. The first approach placed enrichment times at every 40 seconds, after the first 100 seconds of analysis had passed. To have consistent data, the solution of the auxiliary problem analysis is performed over N consecutive time steps yielding N temperature fields which are then processed to extract thermal basis enrichments.

Much of the present study was carried out with blocks of N =12 sets of consecutive temperatures. They were separated into three windows of four seconds each, and a POD analysis was performed on each set. The consistency of the eigenvectors from one window to another was assessed with the modal assurance criterion (MAC), which is the measure of co-linearity of two vectors. For the vectors $\underline{x}$ and $\underline{y}$, the MAC number would be defined as

$$MAC = \frac{\left| \underline{x} \cdot \underline{y} \right|}{\left\| \underline{x} \right\| \left\| \underline{y} \right\|} . \tag{90}$$

The MAC numbers of the three sets of POD modes were then computed and the POD modes that maintained a presence throughout the 12 seconds of analysis would be kept. Initially, a MAC number of 0.9 was used to affirm the presence of a mode in multiple sets of data, and this resulted in the addition of two modes at every enrichment time for a total of 37 modes by the end of the analysis. The two enrichment modes that were added were present in all of the POD mode sets, but were chosen from the POD modes acquired through the first window of four seconds of the auxiliary analysis. It was found through experience that POD modes from the first POD set produced slightly better reduction in

representation error than the latter two POD sets. Shown in the following figures is the representation error when the temperature fields from [10] are projected onto the modal basis, as it evolves in time. The legend entry titled "set 100" relates to the enrichments of the basis found using the auxiliary solution starting after the 100^{th} time step, i.e. from the auxiliary solution in the interval [101,112] seconds and added to the basis from the time of 113 seconds. The solid black line provides at every time the projection error on the most up-to-date basis.

The strategy described above was found to be quite successful in reducing the representation error. Shown in Fig. 9 are the results obtained when a MAC of 0.9 is required for consistency over the three windows of four seconds. The maximum error is 6.1% and occurs at 270 seconds, while the final error (i.e. at the final time of 300s) is 2.9%. These results are significantly better than the 35% of the original model! When the MAC number requirement for keeping a POD mode was reduced to 0.8, only one additional enrichment was added, bringing the total of these modes over the entire time to 11. Figure 10 shows the resulting representation errors: the maximum error of 3.4% occurs at 270 seconds and the final error is 1.3%.

A dynamic adaptation of the reduced order model basis would not only bring in new basis functions but it would also lead to the removal of others. To understand better which modes would be candidate for removal, i.e. those of the original basis or some of the enrichments added at earlier times, the influence of each mode in capturing the desired temperature fields was investigated. The magnitudes of the projections of the temperature on the basis functions, which equal the representation error reduction

induced by each of these basis functions, are presented as bar graphs in Figs 11-13 for the temperature distributions obtained at 100, 200, and 300 seconds. It is seen from this data that several of the thermal modes of the original 27 mode basis remain significant throughout the 300 second analysis while many of them stop contributing significantly and are thus candidates for removal. Further, the enrichment modes added at one time appear to remain strong contributors in later times and thus should be kept throughout. Note the addition/removal of thermal basis functions implies changes in the thermoelastic part of the structural ROM which would need to be updated. Further, small changes in the structural basis would also be expected to take place and that cost should be factored in the adaptation process but was not addressed here.

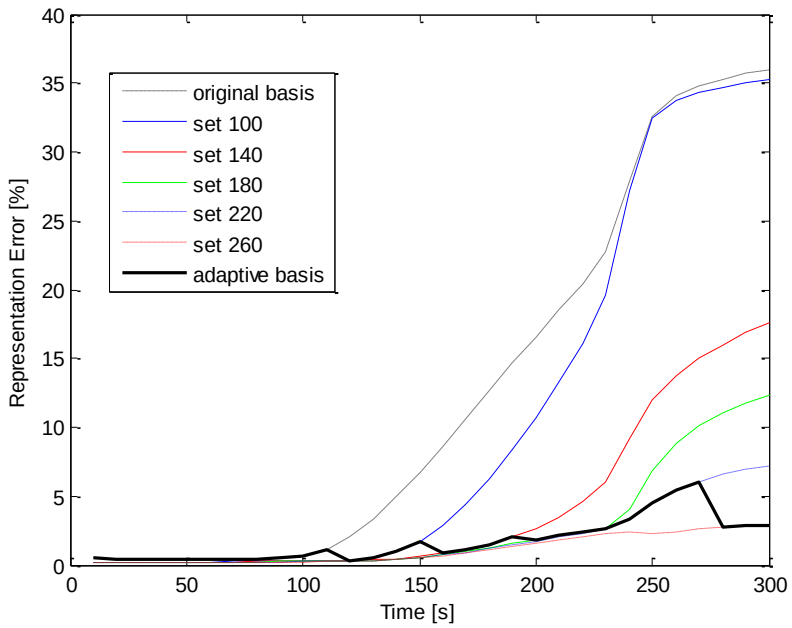

Figure 9. Representation Error of the Adaptive Basis Using a Selection Criterion of a MAC of 0.9.

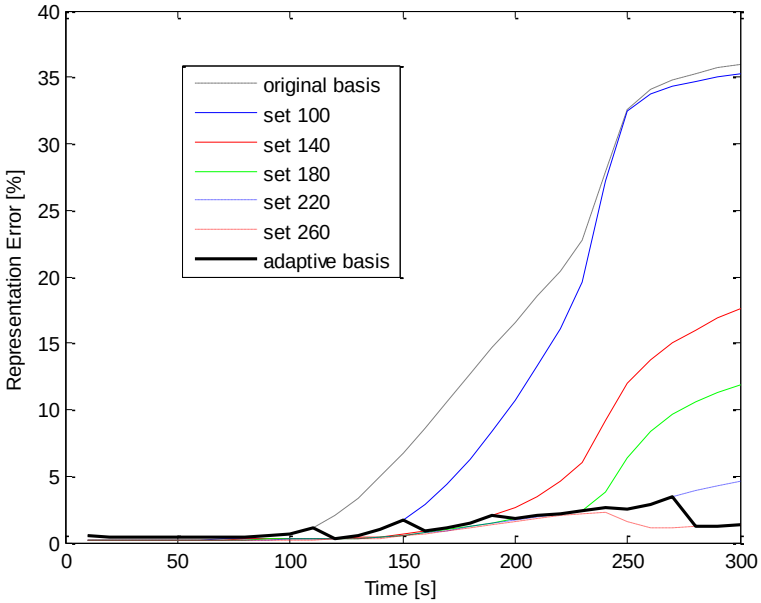

Figure 10. Representation Error of the Adaptive Basis Using a Selection Criterion of a MAC of 0.8.

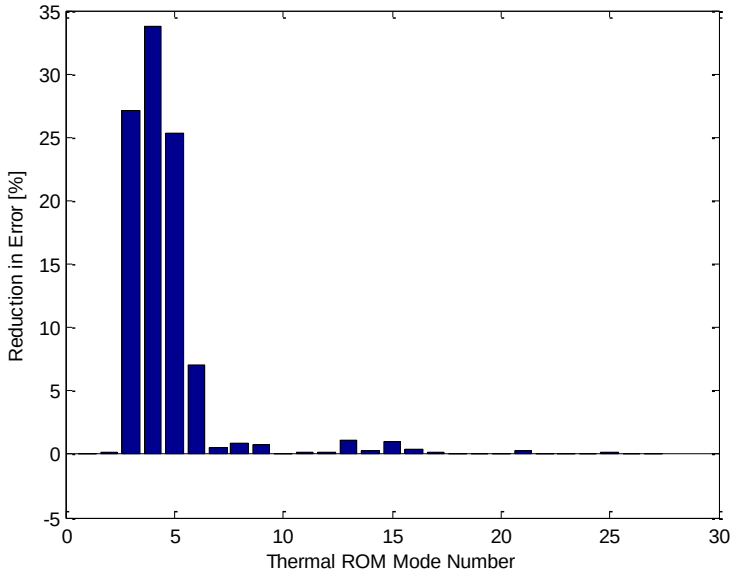

Figure 11. Representation Error Reduction by Each Thermal Mode With the Temperature Field of the Full Order Solution at 100 Seconds.

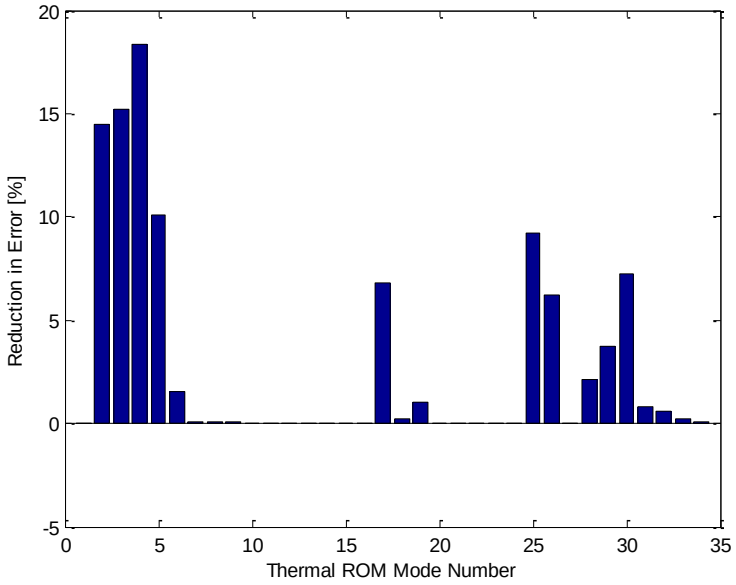

Figure 12. Representation Error Reduction by Each Thermal Mode With the Temperature Field of the Full Order Solution at 200 Seconds.

Finally, the original mode 26 appears to play a uniquely significant role. This mode was selected in the thermal basis for the one-way coupled problem, and is not an enrichment from the auxiliary problem. As shown in Fig. 14, this is a skin mode, in which the stiffener has been decoupled from the response of the skin where the only nonzero temperatures are seen. Similarities between this mode and the true temperature field, shown in Fig. 2(b), are clearly seen and explain the strong influence that this mode has on the representation of the true temperature field, especially at later times.

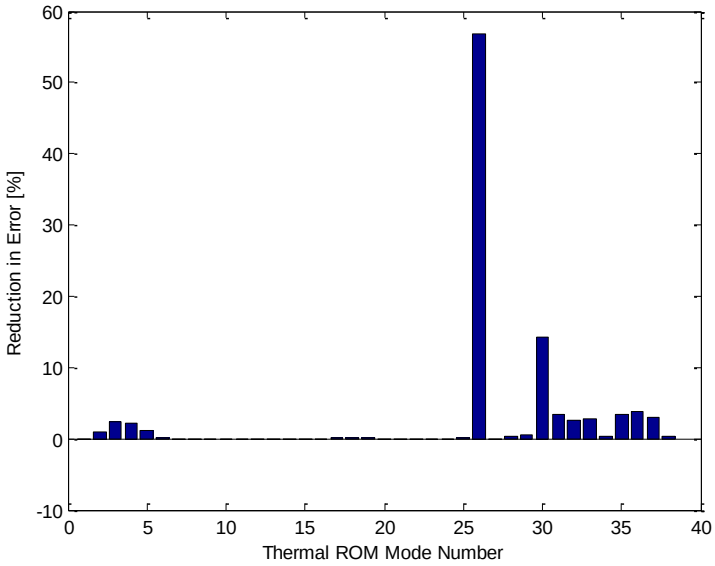

Figure 13. Representation Error Reduction by Each Thermal Mode With the Temperature Field of the Full Order Solution at 300 Seconds.

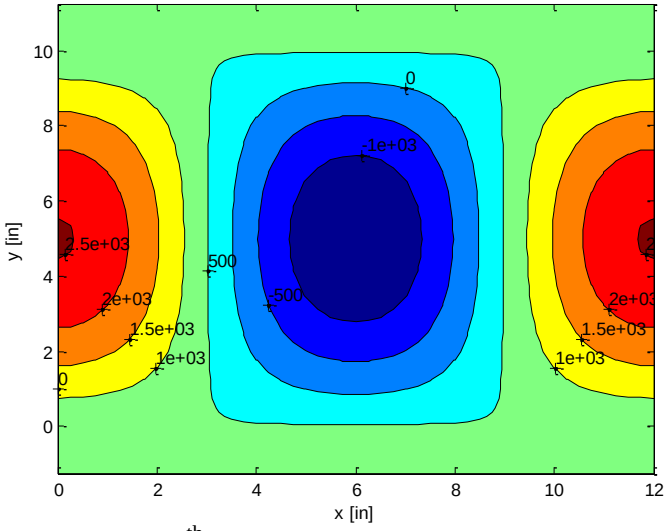

Figure 14. 26th Mode of the Thermal ROM Basis.

Another strategy for determining the enrichment was investigated in which the data entire of the 12-second window was used in a single POD analysis, as opposed to the split into three windows of four seconds each. The three dominant POD modes of the 12-second data were selected at every enrichment location, resulting in 15 additional modes. The corresponding representation errors are shown in Fig. 15: the maximum error is 2.2%

and occurs at 270 seconds, while the final error is 1.3%. These values are slightly smaller than those obtained with the three windows of four seconds each with the 0.8 MAC threshold but four additional modes were added.

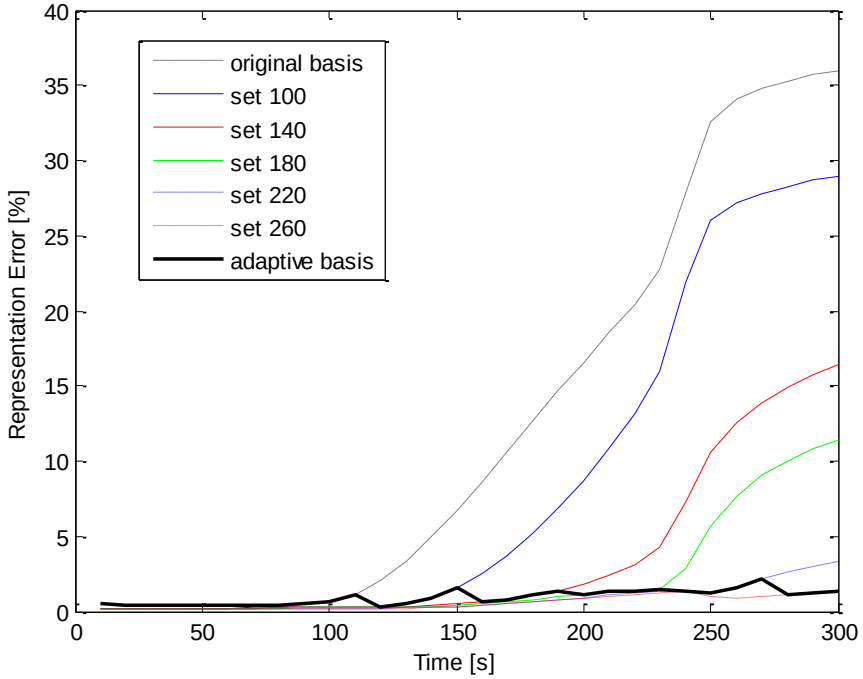

Figure 15. Representation Error When Adaptive Basis is Enriched Using the Dominant POD Modes of a Single Window of 12 Seconds of Data.

It is seen in Figs 9, 10, and 15 that the largest representation error typically occurs in the neighborhood of 270 seconds which coincides somewhat with a shift in the structural response shape. This peak error should be reduced if an enrichment was sought more often than every 40 seconds. Assessing and enriching the basis more often clearly leads to an increased computational effort and thus this strategy would not be desirable unless it led to very significant error reduction benefits. To assess these potential benefits, the enrichment times were made more frequent, i.e. to occur every 20 seconds. The first enrichment location was kept at 101 seconds and so was the window length of 12

seconds. POD analyses were performed on three sets of solutions, comprised of four temperature fields each. POD modes with MAC numbers between these three sets of modes that maintain a value above 0.8 over the 12 seconds were retained. This strategy produced a 15 mode total enrichment to the basis and led to a maximum error of 4.4% occurring at 250 seconds and a final error of 1.9%, see Fig. 16. Surprisingly, these results are worse than their counterparts for enrichment times of 40 seconds and with a larger basis. This observation would suggest that the enrichments were not well captured, possibly because the errors were not large enough to be consistent.

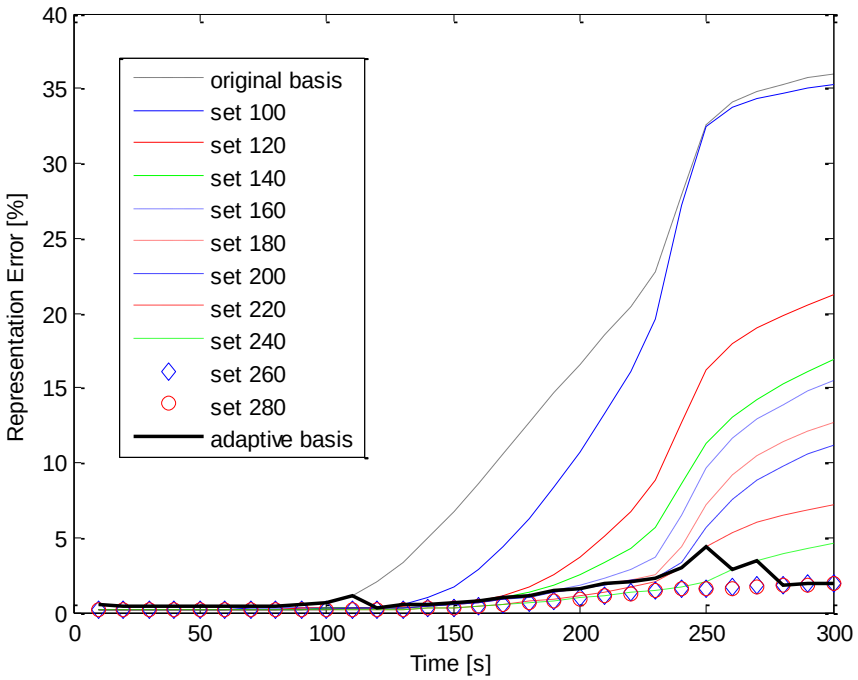

Figure 16. Representation Error of Adaptive Thermal Basis When it is Enriched Every 20 Seconds Using a MAC Criterion of 0.8.

In the above discussion, the auxiliary problem has involved the capacitance and conductance matrices found at reference temperature. Given the large changes in temperature and in those properties over the analysis time of 300s, it was questioned whether better results, i.e. basis functions better capturing the temperature distribution,

could be obtained by varying the capacitance and conductance matrices to reflect the general heating up of the panel. To assess this possibility, the conductance and capacitance matrices were constructed using the temperature field at the beginning, middle, and final time step of the 12-second enrichment analysis. Based on representation errors, there did not appear to be any significant differences between the three different approaches. In all of these cases, three sets of POD modes were found at every enrichment time. After MAC numbers were calculated for the three sets of modes the POD modes that maintained MAC numbers above 0.8 were used to enrich the basis which was done every 40 seconds. Shown in Fig. 17 are the representation errors over the 300 seconds of analysis when the conductance and capacitance matrices are updated with the temperature field at the beginning of the 12 second enrichment location. The maximum error of 3.5% occurs at 270 seconds, and the final error is 1.0%. These results are essentially similar to those obtained with the temperature-independent auxiliary problem suggesting that there is little benefit in this case to update the conductance and capacitance matrices of the auxiliary problem.

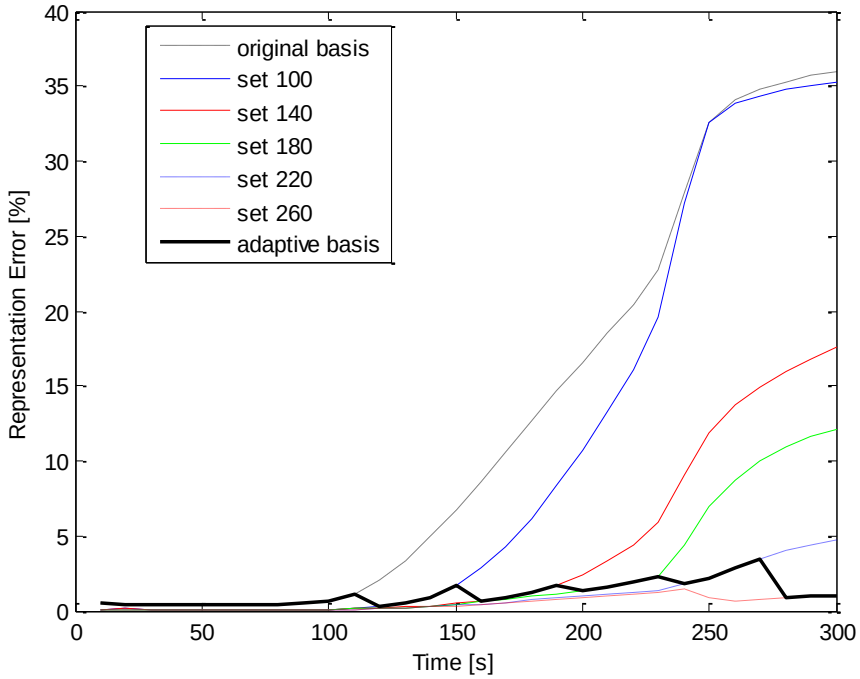

Figure 17. Representation Error of Adaptive Thermal Basis When the Conductance and Capacitance Matrix are Updated at the Beginning of Every Enrichment Location.

Clearly, this approach provides a significant benefit to the reduced order modeling basis under these conditions. It should be noted however, that these results present a best case scenario. The auxiliary problem here utilizes the correct initial temperatures as provided by the two-way analysis thermal results in [10] and thus, the error will increase once the thermal ROM simulation is performed. Nevertheless, this approach has shown the capability to improve upon the performance of the thermal ROM basis.

4.1.3 Two-Way Coupled Analysis: Enriched Basis

A separate approach for developing a thermal basis for the two-way coupled problem is now addressed. The heat flux that the panel is subjected to is dependent on the deflection of the panel into the flow and that transverse deflection is reasonably assumed to be composed of a combination of normal modes. In order to develop a thermal basis

that accounts for the coupling between the displacement and temperature fields, the panel would be displaced according to the shape of each of the normal structural modes and would then be subjected to the type of flow experienced in the expected flight profile. The heat flux predicted by the aerodynamic heating model would then be applied to the panel, and the resulting temperature fields would be used to enrich the thermal basis.

Many parameters could be varied, such as the Mach number applied, length of thermal simulation, displacement level, etc. For the initial attempt, properties were selected which were typical of those experienced throughout the analysis. A Mach number of 7 was selected, which is the average Mach number of the flight trajectory under investigation, and a maximum displacement of 2 thicknesses was assumed when the panel was displaced according to the shape of each linear mode. In the one-way and two-way coupled analysis the maximum transverse displacement is 2.6 and 2.1 thicknesses, respectively, indicating that the displacement level is reasonable. Having subjected the panel to the flow, the heat flux acting on the skin was determined using the aerodynamic heating model. Beginning at reference temperature, the heat flux was then used to simulate the linear, transient heating of the panel for 10 seconds, storing the temperature field occurring on the panel every 0.2 seconds, for a total of 50 temperature fields. Carrying out the simulation longer than 10 seconds did not increase the effectiveness of the resulting thermal enrichments. A POD analysis was then performed on the 50 temperature fields. This process was then repeated for every linear structural mode. In order to select the POD modes to be added to the thermal basis, the temperature fields at 200, 250, and 300 seconds of the two-way coupled analysis in [10] were then

projected onto the thermal basis as the POD vectors from every set were added, one by one, to the original 27 mode basis. The POD modes that caused a significant drop in error were retained in the basis. 12 additional modes were retained when a minimum error drop of 0.3% was required for retention, resulting in a basis of 39 modes that brought the maximum error down to 3.38%. Fig. 18 shows the representation error over the 300 seconds of two-way coupled simulation results.

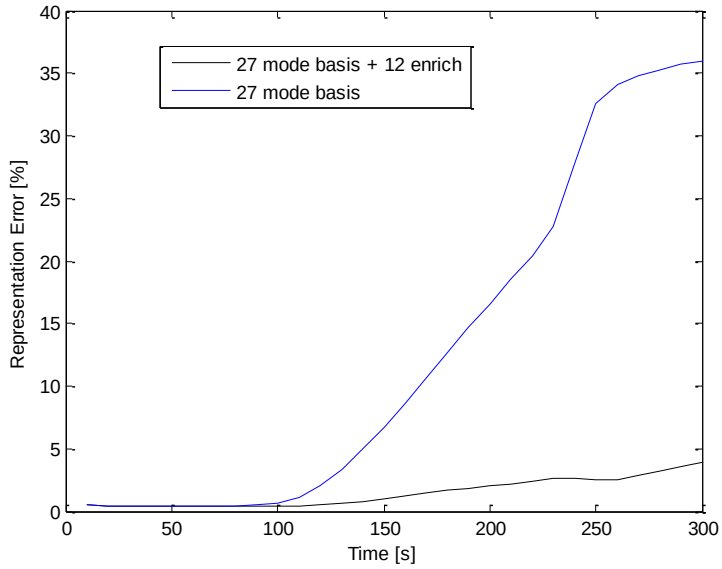

Figure 18. Thermal Representation Error of 39 Mode Basis Over 300 Seconds.

The minimum drop in error required for retention of an enrichment mode is another variable that can be modified, but it was found that the current requirement provided a good balance of accuracy and total number of modes. If, for instance, the minimum error drop was changed to 0.1%, the total number of modes in the thermal basis would be increased to 57, and the maximum error would have been reduced to 1.57%. It was decided that a smaller basis of 39 modes with an error of 3.92 was more desirable.

Next, it was desired to understand the influence that the Mach number of the free stream flow would have on the thermal enrichment modes. In addition to the Mach 7 case outlined above, a free stream flow of Mach 2 and 12 were also used in order to assess the differences between the enrichments found from the low, mid, and high speed flow. A description of the results are shown below in Table 6, where the total number of modes and resulting errors are shown for the various Mach levels used.

Table 6. Effect of Mach on Enrichment Modes

Free Stream Mach	Minimum Error Criteria	Number of Modes	Error at 200 Seconds	Error at 250 Seconds	Error at 300 Seconds
2	0.5%	38	3.3	3.7	4.6
2	0.3%	42	2.3	3.3	4.2
7	0.5%	32	2.8	3.0	4.6
7	0.3%	39	1.8	2.6	3.4
12	0.5%	33	2.8	3.0	4.2
12	0.3%	36	1.9	2.4	4.0

The differing number of total modes makes it a challenge to compare the results between the 3 different Mach numbers selected, but it is apparent that the basis produced from Mach 7 and Mach 12 flow are more effective than the basis produced from Mach 2 flow. These results would seem appropriate, considering that the portion of the flight trajectory that is most difficult to model lies in the region where Mach 7 and Mach 12 flow occur. No apparent advantage is seen in either the Mach 7 or 12 data over the other.

It was desired to see the influence of the nonlinear aspects of the thermal problem on the efficacy of the enrichment modes, and whether or not the nonlinearity could bring the error down significantly more than the 3 to 4% previously acquired. In order to do this, the same analysis was performed, but with radiation included in the 10 second thermal simulation. Here, the Mach 12 flow was used and 50 POD modes were created

from this simulation for each linear structural mode imposed. These POD modes were added to the modes found using the linear thermal simulation. The thermal results from the two-way analysis at 200, 250, and 300 seconds were projected onto these modes, one-by-one, and the dominant modes were added to the original basis of 27 thermal eigenvectors. Table 7 shows these results.

Table 7. Enrichment Modes From Thermal Simulation Including Radiation

Minimum Error Criteria	Number of Modes	Error at 200 Seconds	Error at 250 Seconds	Error at 300 Seconds
0.5%	39	1.7	2.1	3. 7
0.3%	44	1.4	1.9	2. 8

Comparing the results in table 7 with those of table 6, it is concluded that the inclusion of radiation does not bring new, needed information to the basis.

The other nonlinear aspect of the thermal problem is the temperature dependent specific heat and conductivity. These properties were included in the 10 second thermal simulation assuming Mach 12 flow, and the 50 resulting thermal POD vectors were added to the 50 POD vectors from the linear thermal analysis. Again, temperature fields from the two-way thermal analysis were projected onto these modes and the ones causing a drop in error greater than the minimum requirement were retained in the basis. Table 8 shows the results for this basis.

Table 8. Enrichment Modes From Thermal Simulation Including Radiation and Temperature Dependent Properties

Minimum Error Criteria	Number of Modes	Error at 200 Seconds	Error at 250 Seconds	Error at 300 Seconds
0.5%	39	1.8	2.5	3.9
0.3%	47	1.6	2.2	3.3

It is apparent from these results that the inclusion of nonlinear properties do not bring anything new to the basis.

The displacements of the panel occurring during the fully coupled analysis will be a combination of the transverse modes that are being used to find these thermal enrichments. Thus far, the principle of superposition has been assumed, in that the temperature fields produced by imposing each linear structural mode can add to represent the temperature field produced by a displacement that is a combination of these structural modes. Here, an approach is used that attempts to assess whether or not the nonlinear aspects of the problem inhibit the assumption of superposition that is used thus far in the analysis. It should be noted that the displacements are dominated by the first normal mode in the one-way coupled analysis, and both the first and second normal modes in the two-way coupled analysis.

Displacements of the panel were imposed which were a combination of the first structural mode and every other linear structural mode, totaling 16 displacement fields. The aerodynamic analysis was carried out assuming a free stream flow of Mach 12, and the resulting heat flux acting on the panel was used in a linear transient analysis to simulate the heating on the panel for 10 seconds. This process was then repeated using combinations of the second normal mode, and every other normal mode in the basis. Both of these sets of enrichments were then added to the enrichment set that was constructed when using each linear mode on its own, without combinations. The temperature fields from the two-way coupled analysis at 200, 250, and 300 seconds were then projected onto these modes and the effective modes were added to the basis. The resulting bases produced the results shown in Table 9.

Table 9. Enrichment Modes From Thermal Simulation Including Radiation and Temperature Dependent Properties

Minimum Error Criteria	Number of Modes	Error at 200 Seconds	Error at 250 Seconds	Error at 300 Seconds
0.5%	33	2.8	3.0	4.2
0.3%	36	1.9	2.4	4.0

As can be seen, the results shown in Table 9 match almost exactly the results found in Table 6, in which the thermal enrichments were found using individual structural modes, as opposed to structural mode combinations. Thus, it was concluded that using combinations of structural modes brought no new, useful information to the basis.

In all previous attempts at acquiring enrichment modes the transient thermal analysis was carried out for ten seconds with the same heat flux. In the original analysis of [10], the thermal loading was updated at every half second. The next effort to develop enrichment modes involves carrying out a 10 seconds thermal analysis in which the heat flux is updated every half second, while the displacement remains fixed according to the shape of each linear mode. This simulation assumes an initial Mach 7 freestream flow, and the Mach number was increased linearly to 7.33 over the 10 seconds. A POD analysis was performed on the resulting temperature fields, and the temperature fields of the two-way coupled analysis were projected onto them. The POD modes that caused a reduction in representation error greater than a predetermined percentage were retained and added to the original 27 mode thermal ROM. Table 10 presents the results for the final basis.

Table 10. Enrichment Modes From Thermal Simulation With Updated Loading

Minimum Error Criteria	Number of Modes	Error at 200 Seconds	Error at 250 Seconds	Error at 300 Seconds
0.5%	40	3.0	2.7	3.4
0.3%	46	2.7	2.3	2.7

Next, an analysis was carried out in which a free stream flow of Mach 12 was used and the panel was displaced to a maximum of 0.2 thickness, one tenth of what has been used previously, in order to see the effect of smaller displacements on the enrichment modes. After the linear thermal transient simulation was performed, a POD analysis was performed on the temperature fields and the POD modes that produced a significant drop in error were added to the basis. The results of this new basis can be seen in Table 11.

Table 11. Enrichment Modes From Small Structural Displacement

Minimum Error Criteria	Number of Modes	Error at 200 Seconds	Error at 250 Seconds	Error at 300 Seconds
0.5%	33	2.8	3.0	4.2
0.3%	36	1.9	2.4	4.0

No difference is observed between the basis developed at smaller and larger displacements.

Considering all of the bases developed, it was decided that the 39 mode basis which was constructed from the structural induced thermal enrichments with a free stream flow of Mach 7 would be used. The cost to assemble these enrichment modes is minimal, considering a linear thermal analysis is utilized. The Mach 7 flow is the average Mach number of the flows experienced in the analysis, and the 2 thickness displacement is within the range of displacements expected during the analysis.

It was desired to find what additions to the basis were necessary in order to bring the representation error down below 1%. In order to do so, the temperature field from every second of the 300 second analysis was projected onto the new 39 mode basis, and the difference between the projected temperature and true temperature were stored. A POD of these 300 residual vectors was then performed, and the dominant POD modes

were added to the 39 mode basis in order to determine their effect on the capturing of the true temperature fields. Figure 19 shows the error of the original 39 mode basis from 100 to 300 seconds, as well as the error from the bases which include various numbers of POD modes.

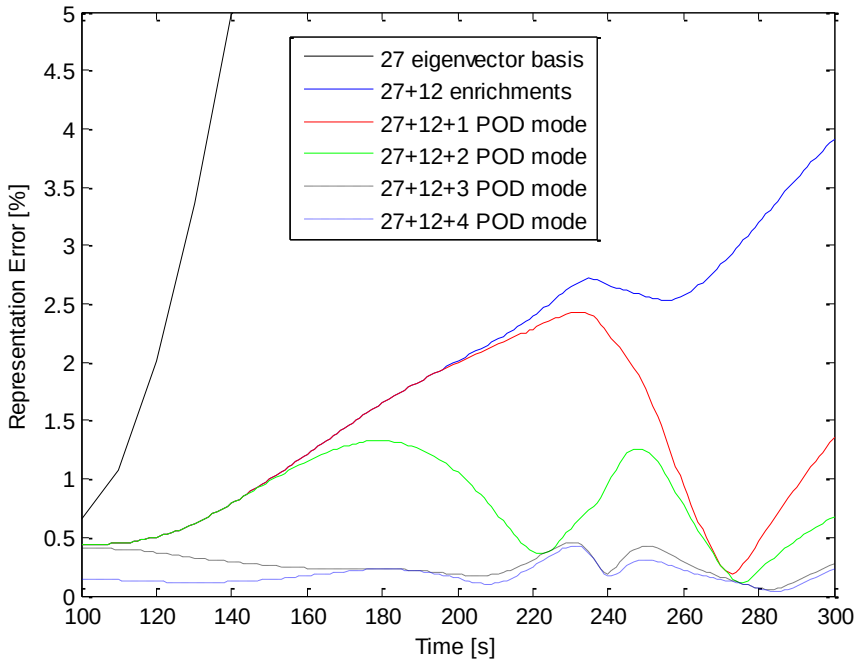

Figure 19. Thermal Representation Error When POD Modes Are Added to Thermal Basis.

As can be seen, the basis with 3 POD modes brings the maximum error down below half a percent. This new 42 mode basis will be used in model building in addition to the 39 mode basis.

To give perspective on the efficiency of the enriched basis, it was desired to see how the eigenvectors of the capacitance-conductance eigenvalue problem would fare in representing the temperature fields in the two-way coupled analysis. The previous thermal basis selected for the one-way coupled analysis was comprised of 27 eigenvectors. As described in section 4.1.1, the eigenvectors of the full model, as well as

the constrained model were used in the creation of the basis. The temperature fields occurring at 200, 250, and 300 seconds of the two-way coupled analysis will be projected onto the remaining thermal eigenvectors, and the ones creating an error drop greater than a predetermined value will be retained in the basis. The following results in Table 12 were observed.

Table 12. Basis Composed of Eigenvectors

Minimum Error Criteria	Number of Modes	Error at 200 Seconds	Error at 250 Seconds	Error at 300 Seconds
0.5%	53	2.7	3.5	3.6
0.3%	46	1.9	2.2	2.5

The results indicate that using eigenvectors exclusively to form the basis for the two-way coupled analysis is far less efficient than using the previously investigated enrichment modes.

With the basis selected, it was next desired to check the accuracy of results found from a thermal model built using this basis. This was done independently of a structural ROM by carrying out the 300 second, two-way coupled simulation using the previously defined aerodynamic model, the full order Nastran structural model, and the thermal reduced order model. First, results will be presented using the 39 mode thermal model. The error in the temperature field at every second of the two-way 300 second analysis, as compared to the results in [10], are presented below in Figure 20.

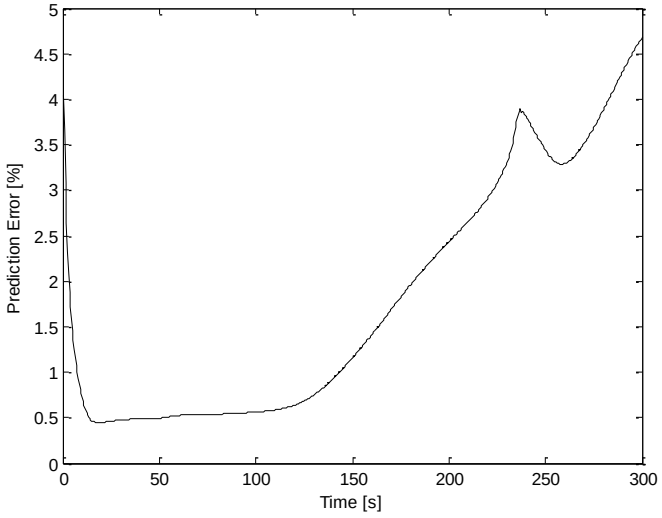

Figure 20. Thermal Prediction Error Over 300 Seconds for 39 Mode Thermal ROM.

The error in the structural displacement fields were also found with respect to the structural results in [10] and are presented in Figure 21.

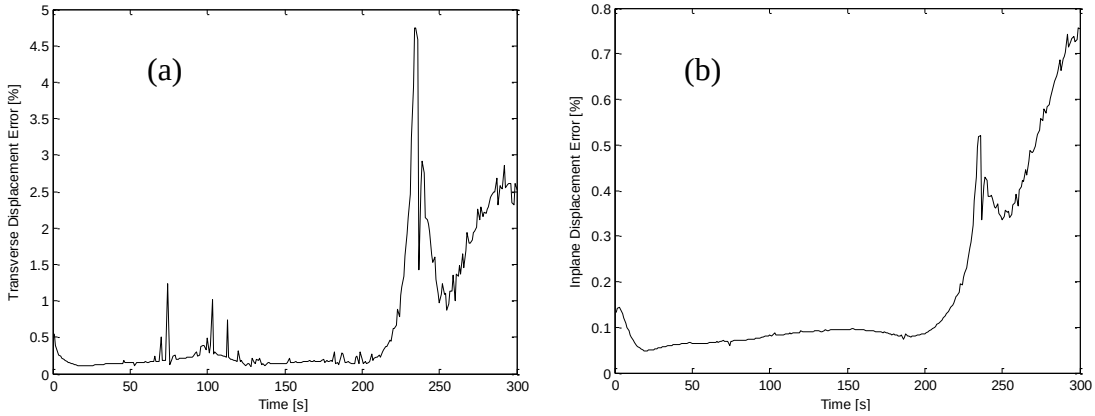

Figure 21. (a) Transverse and (b) Inplane Structural Prediction Error When Predicting Temperature Fields Using the 39 Mode ROM.

Although an error of approximately 5% is seen in the thermal results, this corresponds to a final transverse displacement error of approximately 2.5%. The maximum of nearly 5% at 240 seconds corresponds to a period of time when the panel shifts from having a peak at the center and being dominated by the first structural mode, to having a peak at the front of the panel and being dominated by the second structural mode. This transition

phase proved difficult to predict accurately, but the model resumes accurate predictions after this phase.

Next, the same simulations, which involve the previously described aerodynamic model, the full order Nastran structural model, and the reduced order thermal model, were carried out with the 42 mode thermal model. The thermal and structural errors over the 300 seconds of analysis are shown in Figs 22 and 23, respectively.

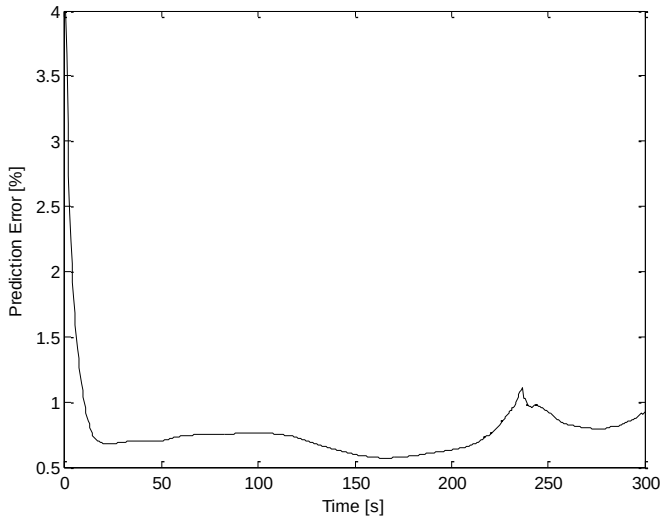

Figure 22. Thermal Prediction Error Over 300 Seconds for 42 Mode Thermal ROM.

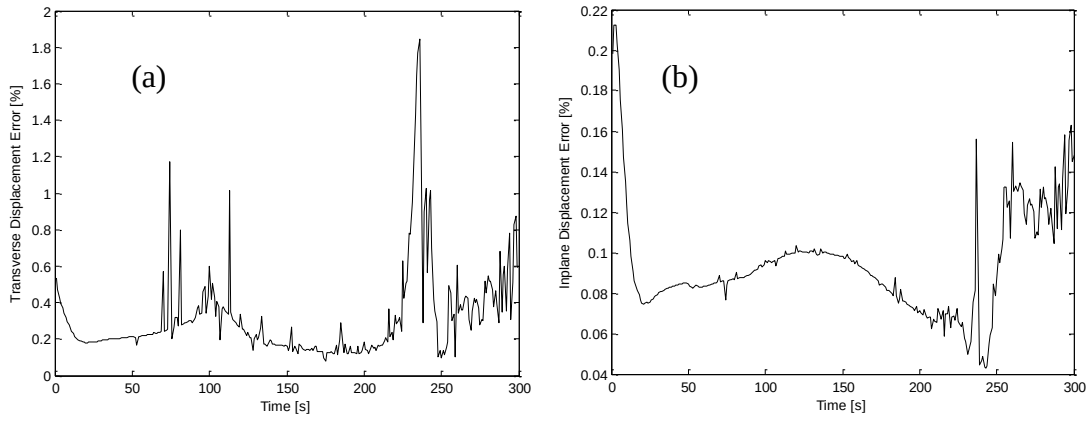

Figure 23. (a) Transverse and (b) Inplane Structural Prediction Error When Predicting Temperature Fields Using the 42 Mode ROM.

The 42 mode thermal model produces results that are significantly improved over the 39 mode model. The thermal error is mostly kept under 1% and the transverse structural error is also below 1% in all but a few portions of the analysis. The inplane error is kept very low.

4.2 Results for the Structural ROM of the Representative Panel

4.2.1 Validation in Isothermal Conditions

The first step taken in the construction of the fully coupled structural model was to develop and validate an isothermal model. In order to assess the effectiveness of the basis as it is constructed, a series of displacements, static displacements as well as "snapshots" of dynamic behavior, were projected onto the chosen basis. The static cases were produced using uniform pressure on the top of the panel, and the results ranged in displacements from about 0.7 to 2.2 thicknesses. The dynamic data was found by subjecting the panel to a white noise excitation, the sound pressure level (SPL) of which was 171 dB with a frequency band of 2 kHz. This produced a maximum deflection of about 3.2 thicknesses. A set of 101 "snapshots" of this data were selected.

Focusing first on the selection of a set of the linear modes of the panel, it was noted that 30 linear modes are present in the chosen frequency band with 16 of them participating in the response. With this first component of the basis, the average transverse and inplane representation errors were 0.81% and 48.17%, respectively, for the 101 dynamic snapshots considered. This error here is computed as the norm of the difference between the finite element predicted displacements and the projection of this

displacement onto the basis, divided by the norm of the finite element predicted displacement, i.e.

$$\varepsilon_{rep} = \frac{\left\| \underline{u} - \underline{u}_{proj} \right\|}{\left\| \underline{u} \right\|}. \tag{91}$$

In addition to the 16 in band modes, 5 out of band linear modes were found to participate. With these additional modes, the average transverse and inplane representation error for the dynamic data was improved to 0.63% and 48.06%, respectively.

In order to capture the nonlinear motion of the response, 24 duals were added to the basis. All of these duals were found using mode 1 as the dominant mode. The resulting 45-mode basis led to average representation errors of 0.16% transverse and 2.48% inplane. The displacements that these duals were derived from were also used to find 81 tangent duals. These tangent duals were added to the basis, which resulted in 126 modes and average transverse and inplane errors of 2.72E-4% and 0.50%. Clearly then, a basis developed from the methodologies outlined above can span the desired space. It was further expected that less than 126 modes would be truly necessary. To reduce the number of modes, the dynamic and static snapshots were projected onto the 126 mode basis and a POD analysis was done of the resulting projection coefficients for the basis (excluding the in-band linear modes). This analysis produced a new combination of modes that captures the dynamic response more efficiently; a 32 mode basis was found sufficient. This 32 mode basis then consisted of the 16 in-band linear modes, as well as the first 16 of the POD eigenvectors of the dual and tangent dual modes. This basis

produced average transverse and inplane errors of 0.1% and 2.39%. The progress made by each subsequent addition to the basis is shown below in Table 13.

Table 13. Average Dynamic Representation Error of Panel

	Transverse Error (%)	Inplane Error (%)
16 modes	0.81	48.17
21 modes	0.63	48.06
45 modes	0.16	2.48
126 modes	2.72 E-4	0.50
32 modes	0.1	2.39

The parameters of the reduced order model based on these 32 modes were next identified by the tangent stiffness matrix approach. The predictive capabilities of the ROM were assessed first under static, uniform loading applied to the top of the panel. Under a static loading of 3 psi in the upward direction, which yields a maximum displacement of about 2.3 thicknesses, the model had 0.30% error in the transverse direction and 1.12% error in the inplane direction when compared to Nastran. With a loading of 3 psi in the downward direction, which resulted in about 2.4 thickness displacement, a transverse error of 0.61% and inplane error of 0.57% was obtained. These results, including those obtained under smaller loading, can be seen in Table 6 below. To support these numbers, shown in Figs 24 and 25 is a comparison of the transverse and inplane displacements of the panel predicted by the reduced order model with those obtained by Nastran. As suggested by the low error levels, the match is indeed very good.

Table 14. Prediction Errors of Panel

	Transverse Error (%)	Inplane Error (%)
1 psi up	.22	1.60
1 psi down	.29	0.70

3 psi up	.30	1.12
3 psi down	.61	.57

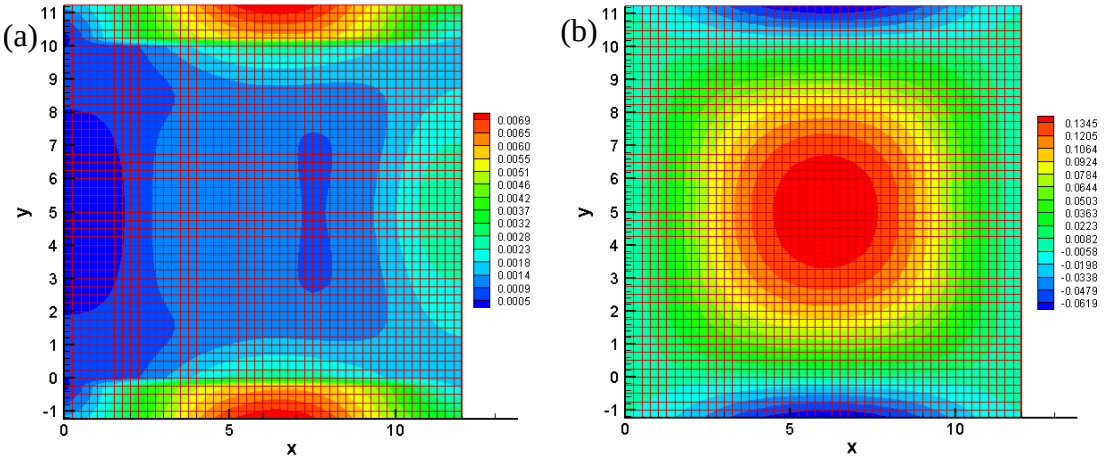

Figure 24. (a) Magnitude of Inplane Displacement and (b) Transverse Displacement From 3 psi Upward Loading. Units in Inches. Results From 32 Mode ROM.

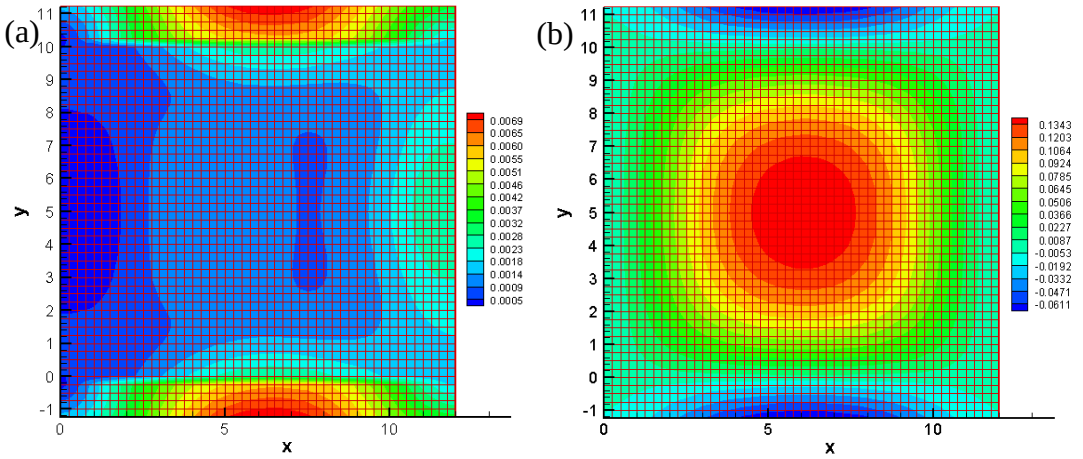

Figure 25. (a) Magnitude of Inplane Displacement and (b) Transverse Displacement From 3 psi Upward Loading. Units in Inches. Results From Nastran Nonlinear.

Next, the ability of the ROM to predict the dynamic response was assessed by subjecting the panel to a white noise excitation of 145 dB and a frequency band of 2 kHz. This excitation resulted in a standard deviation of transverse displacement at the beam center of 0.0165 inches, or approximately a quarter panel thickness. This displacement level is non-linear, although only mildly. Figure 26 shows the power spectral density of

the transverse deflection at the beam center for both the reduced order model and Nastran SOL 400. Figure 27 shows its counterpart for the deflection in the *x* (T1) direction at the center. Note that a boundary condition is enforced at the panel center that restricts motion in the T2 direction. Clearly, an excellent match of the Nastran results is obtained at this mildly nonlinear response level.

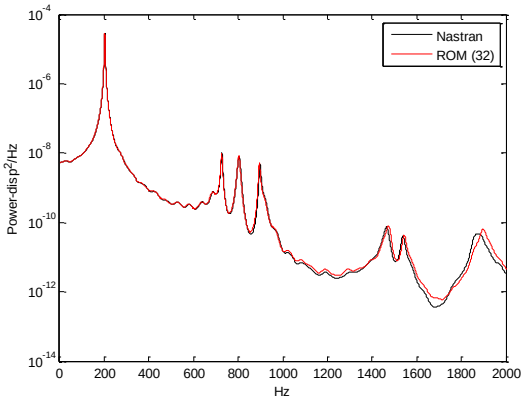

Figure 26. Power Spectral Density of the Transverse Deflection at Panel Center, 145 dB.

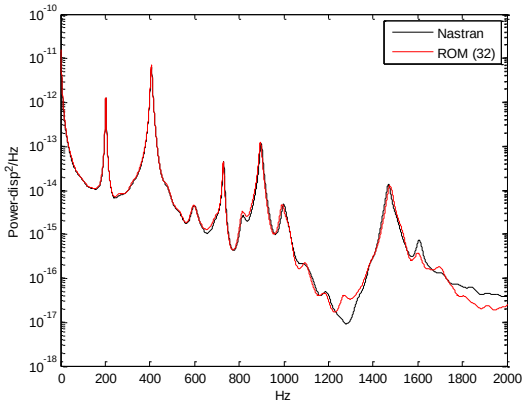

Figure 27. Power Spectral Density of the Inplane Deflection at Panel Center, 145 dB.

To continue the assessment of the reduced order model accuracy, a white noise excitation of 155 dB in the same frequency band of 2 kHz was applied. This resulted in a standard deviation of transverse displacement at the beam center of 0.69 thicknesses. The

spectra of the T3 and T1 deflection can be seen in Figs 28 and 29, respectively, with their Nastran counterparts and a very good match with these results is again obtained.

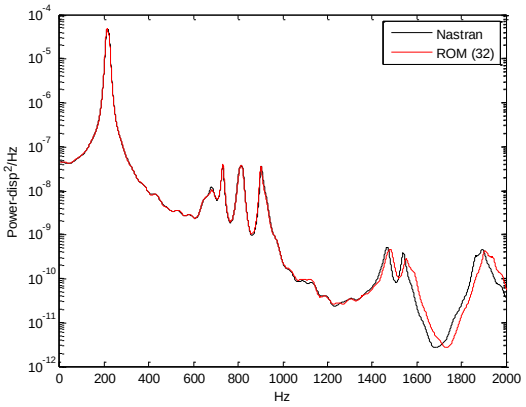

Figure 28. Power Spectral Density of the Transverse Deflection at Panel Center, 155 dB.

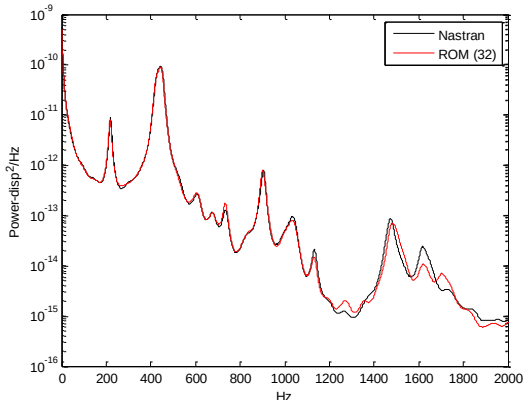

Figure 29. Power Spectral Density of the Inplane Deflection at Panel Center, 155 dB.

4.2.2 Validation with Uniform Temperature Field

It should be noted, first, that contrary to the structural model in [10], the structural ROM constructed here did not include a temperature dependent coefficient of thermal expansion (CTE). Instead, the value of CTE was held constant at its value at the reference temperature of 530 R, which is 5.84 E-7. The construction and validation of a structural reduced order model that includes temperature dependent material properties is carried out with the panel in Section 4.2.6.

As discussed in Section 3.2.1, it was necessary to enrich the structural-only basis to account for the displacements induced by the thermal expansion. This construction and its validation were performed in two different steps. It was assumed in a first step that the temperature distribution was uniform and the single enrichment corresponding to the static linear response to this uniform temperature change was determined. This effort thus led to a 33 structural mode basis.

Next, structural basis enrichments were developed to capture the thermal expansion induced by the remaining 26 thermal modes of the thermal basis of Section 4.1. Since adding 26 modes to the basis was not desirable, a POD analysis was performed on these 26 displacement sets and the first four POD modes were found to sufficiently improve the ability of the structural basis to represent the desired displacement field. The structural basis included these four modes in addition to the 33 modes previously described. The resulting 37 mode basis gave a transverse representation error of 0.17 % and inplane representation error of 0.11 % when the structural response from the final temperature field of Figure 3(a) predicted by the finite element model was projected onto the basis.

The validation of the structural reduced order models was carried out first under uniform temperature fields and without applied pressure. Shown in Figs 30(a) and (b) are the predicted transverse displacement and magnitude of inplane displacement, respectively, by the reduced order model while the corresponding figures for the Nastran predictions are on Figs 31 (a) and (b). The matching between these two sets of figures is excellent, the transverse norm error is 0.54% and the inplane one is 0.05%. It is

interesting to note that the inplane response at the center of the panel near the leading edge is close to zero, which is intuitive given the boundary conditions. The magnitude of the inplane displacement grows larger near the edges, where thermal expansion has caused the most displacement. The discontinuity at the stiffener is due to the expansion in the *y* direction being defined as transverse for the stiffener vs. inplane for the skin. This is also the reason for the sudden appearance of large transverse motion in the stiffener in Fig. 30 (b). Positive transverse motion in the stiffener is defined as motion away from the skin, as opposed to motion that would place the stiffener under the skin.

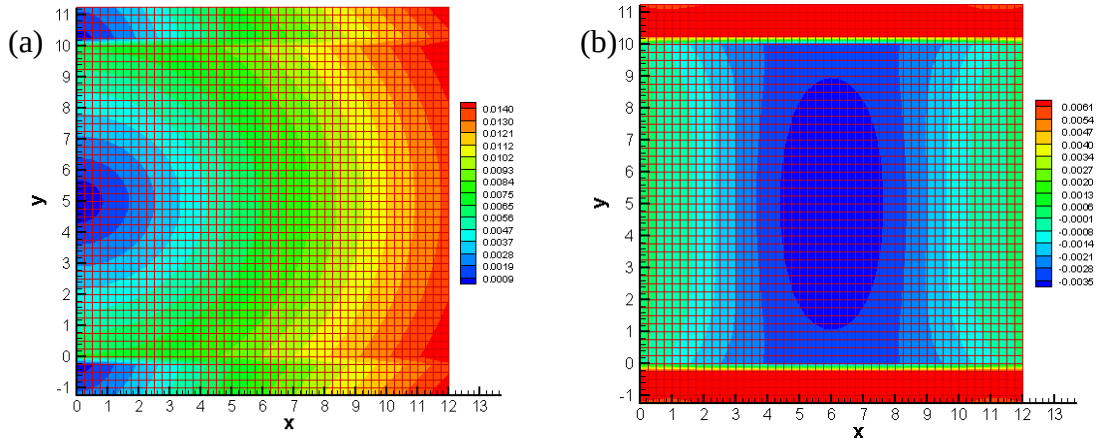

Figure 30. (a) Magnitude of Inplane Displacement and (b) Transverse Displacement From Uniform Temperature Field of 2700 R. Units in Inches. Results From 33 Mode ROM.

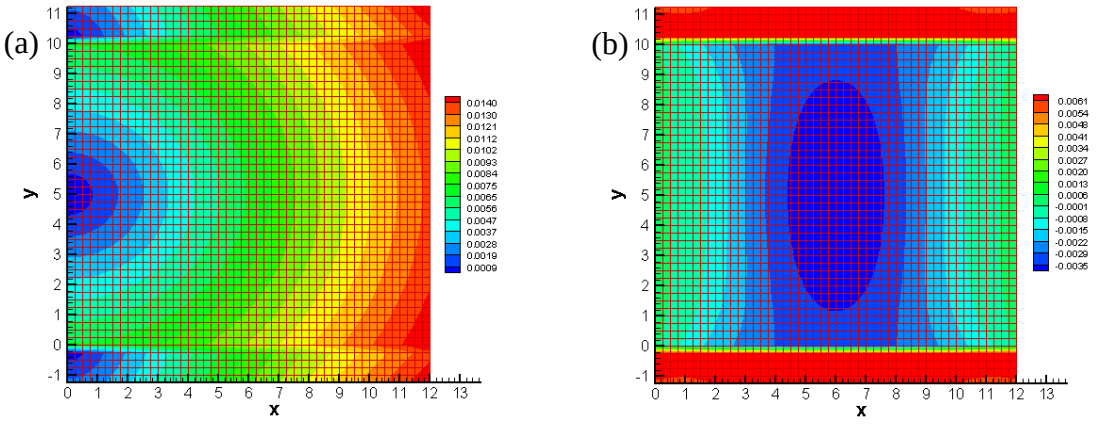

Figure 31. (a) Magnitude of Inplane Displacement and (b) Transverse Displacement From Uniform Temperature Field of 2700 R. Units in Inches. Results From Nastran Nonlinear.

Additional comparisons between responses predicted by the ROM and Nastran were carried out with the uniform temperature increase of 2700 R when the panel skin (not stiffener) was also subjected to a uniform pressure, see Table 15 for error comparisons and Figs 32 and 33 for an upward pressure load of 3 psi. Again, an excellent matching between Nastran and ROM results is obtained with displacements varying between approximately -3 and +3 thicknesses.

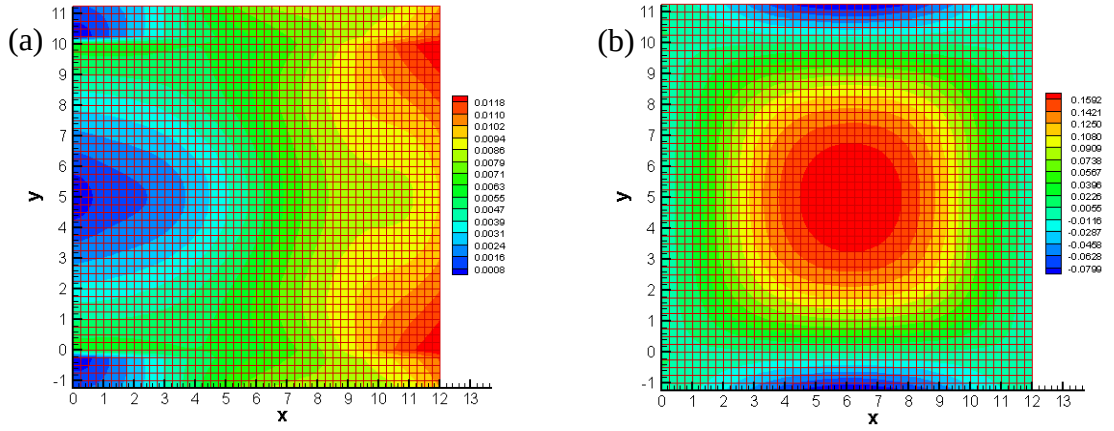

Figure 32. (a) Magnitude of Inplane Displacement and (b) Transverse Displacement From Uniform Temperature Field of 2700 R and 3 psi Upward Loading. Units in Inches. Results From 33 Mode ROM.

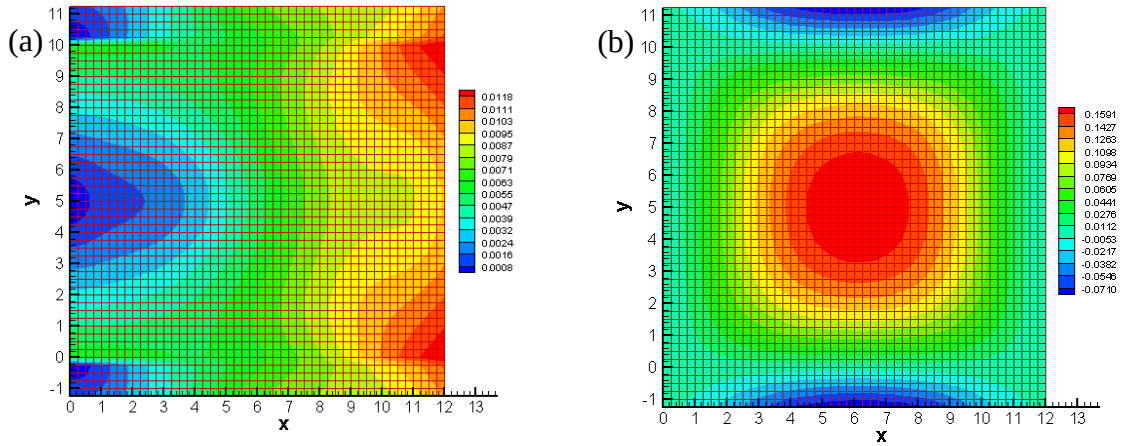

Figure 33. (a) Magnitude of Inplane Displacement and (b) Transverse Displacement From Uniform Temperature Field of 2700 R and 3 psi Upward Loading. Units in Inches. Results From Nastran Nonlinear.

Table 15. Results From 2700 R Uniform Temperature and Pressure Loads. 33 Mode ROM.

	Transverse error [%]	Inplane error [%]	Nastran center disp. [thick.]	ROM center disp. [thick]
3 psi down	.38	.50	-2.98	-2.98
2 psi down	.29	.20	-2.49	-2.49
1 psi down	.49	.13	-1.80	-1.81
0 psi	.54	.05	-.065	-.064
1 psi up	.51	.52	1.62	1.62
2 psi up	.33	1.1	2.25	2.25
3 psi up	1.6	3.2	2.69	2.70

4.2.3 Validation with Non-Uniform Temperature Field

The validation of the enriched structural basis proceeded finally with the 37 mode model of section 4.2.2 and the temperature field of Fig. 3(b), determined by the thermal ROM. The displacement field induced by this temperature distribution without and with additional uniform pressure on the panel skin was computed by the ROM and by Nastran, see Figs 34-37 and Table 16. The observations drawn in connection with the uniform temperature are found to be applicable again here: an excellent matching between ROM and Nastran predictions is consistently observed.

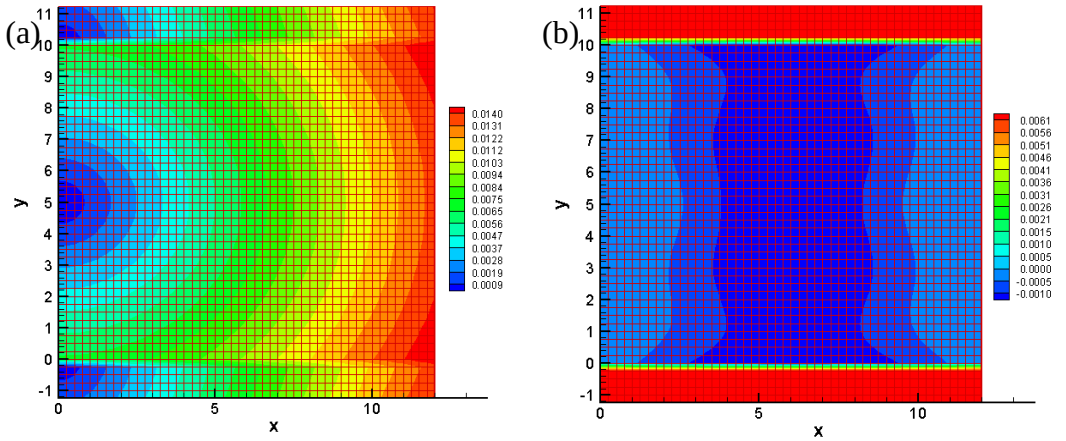

Figure 34. (a) Magnitude of Inplane Displacement and (b) Transverse Displacement From Final Temperature Field. Units in Inches. Results are From 37 Mode ROM.

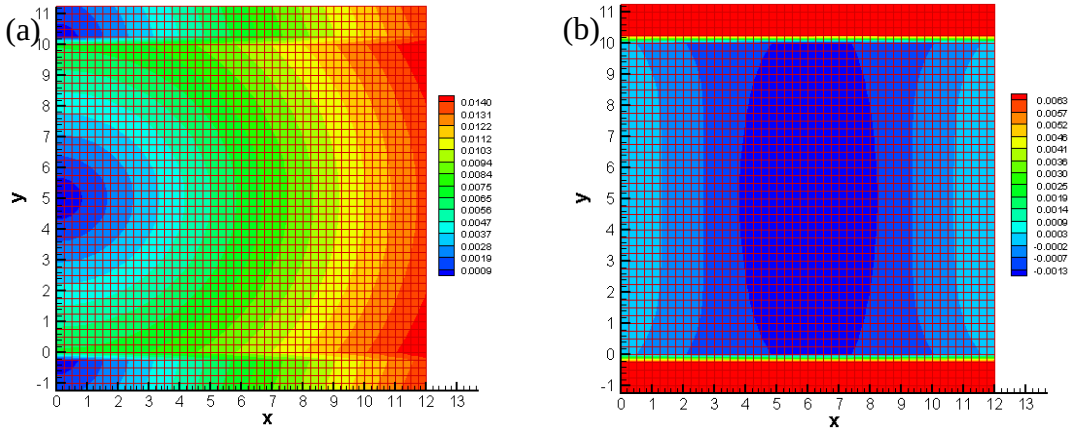

Figure 35. (a) Magnitude of Inplane Displacement and (b) Transverse Displacement From Final Temperature Field. Units in Inches. Results From Nastran Nonlinear.

Table 16. Results From Final Temperature With Pressure Loads. 37 Mode ROM.

	Transverse error [%]	Inplane error [%]	Nastran center disp. [th]	ROM center disp. [th]
3 psi down	.36	.26	-2.99	-2.99
2 psi down	.31	.32	-2.50	-2.50
1 psi down	.52	.38	-1.81	-1.81
0 psi	1.35	.34	-.024	-.023
1 psi up	.47	.28	1.65	1.66
2 psi up	.24	.68	2.28	2.28
3 psi up	2.69	4.18	2.72	2.74

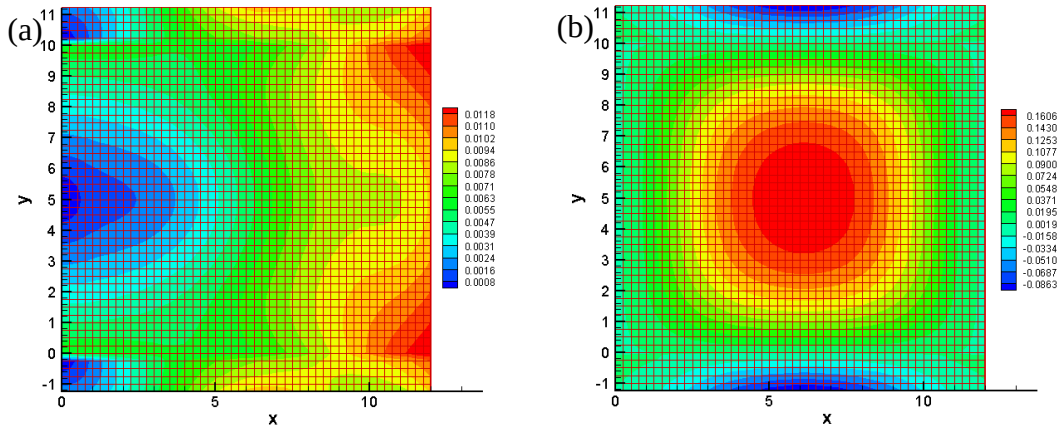

Figure 36. (a) Magnitude of Inplane Displacement and (b) Transverse Displacement From Final Temperature Field and 3 psi Upward Loading. Units in Inches. Results Are From 37 Mode ROM.

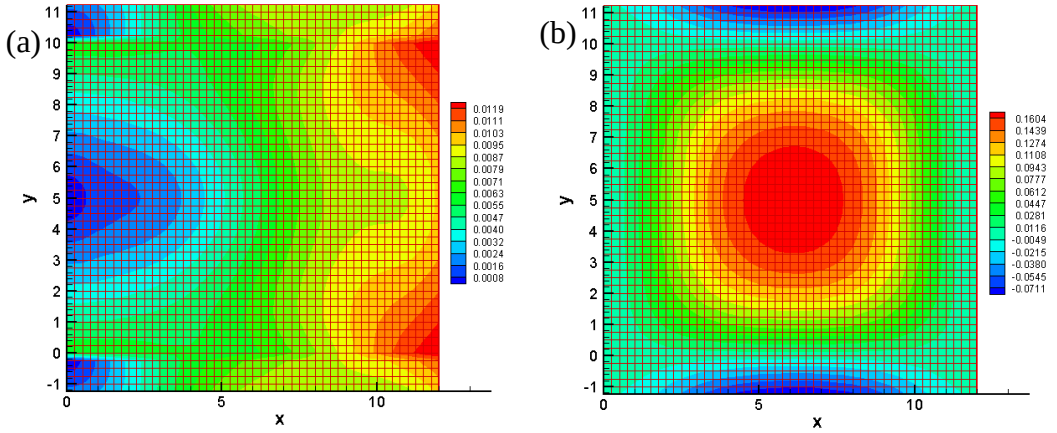

Figure 37. (a) Magnitude of Inplane Displacement and (b) Transverse Displacement From Final Temperature Field and 3 psi Upward Loading. Units in Inches. Results From Nastran Nonlinear.

It was finally desired to confirm the adequacy of the 37 modes over the entire temperature range. To this end, it was used for the prediction of the panel response in the absence of thermal loading but with applied pressure. Shown in Figs 38 and 39 (a) and (b) are the transverse and inplane responses to a loading of 3 psi in the upward direction. Moreover, the errors between the ROM and Nastran predictions for various pressure

loads acting on the panel without a thermal load are shown in Table 17. They are consistent with prior errors, see Tables 15 and 16.

Table 17. Results From Uniform Pressure Loads Without Thermal Loading. 37 Mode ROM.

	Transverse error [%]	Inplane error [%]	Nastran center disp. [th]	ROM center disp. [th]
3 psi down	1.09	.84	-2.45	-2.47
2 psi down	.52	.57	-1.93	-1.94
1 psi down	.18	.62	-1.20	-1.20
1 psi up	.16	1.26	1.14	1.14
2 psi up	.63	1.36	1.81	1.82
3 psi up	2.33	3.87	2.28	2.31

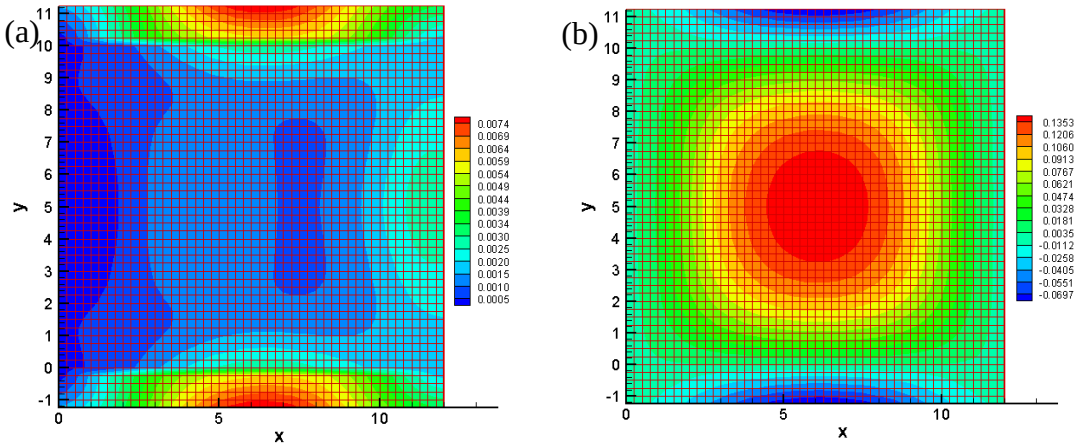

Figure 38. (a) Magnitude of Inplane Displacement and (b) Transverse Displacement From 3 psi Upward Loading. Units in Inches. Results Are From 37 Mode ROM.

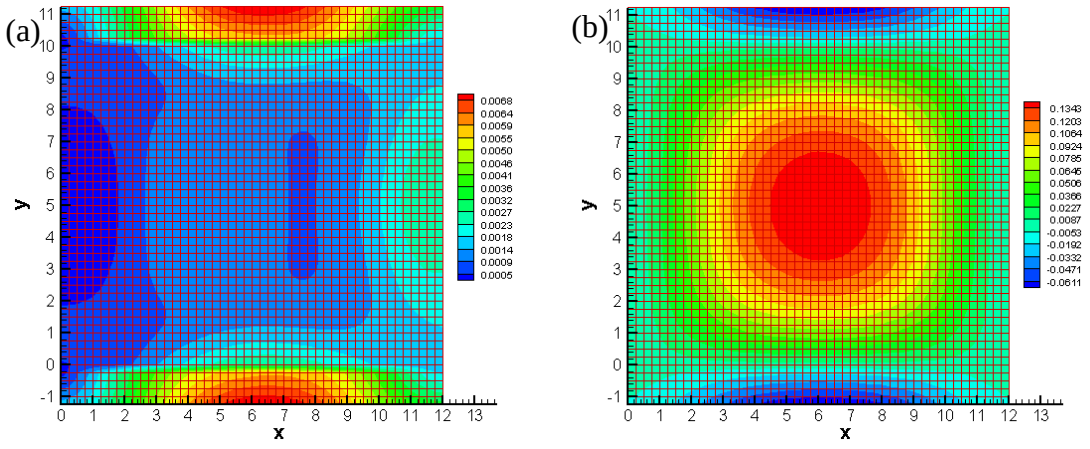

Figure 39. (a) Magnitude of Inplane Displacement and (b) Transverse Displacement From 3 psi Upward Loading. Units in Inches. Results From Nastran Nonlinear.

4.2.4 Thermal Buckling Investigation

The model so far has used a constant CTE value of 5.84 E-7 1/F, which does not produce a buckling effect in the temperature range specified. Before developing a model which incorporates the temperature dependent CTE, it is first desired to show that the ROM accurately captures the buckling effect. The prediction of thermal buckling is highly sensitive to changes in the model parameters. To demonstrate this sensitivity, the deformations of the panel with constant coefficient of thermal expansion, equal to 1.33 E-6 1/F, to a uniform temperature load was determined using MSC Nastran and NX Nastran for a broad range of applied temperatures. The same static nonlinear solver (SOL106) was used in both cases, but yielded very different results. Figure 40 shows the displacement at the center of the skin of the panel to uniform temperature loading predicted by MSC and NX Nastran, while Fig. 41 shows the norm error between the two responses.

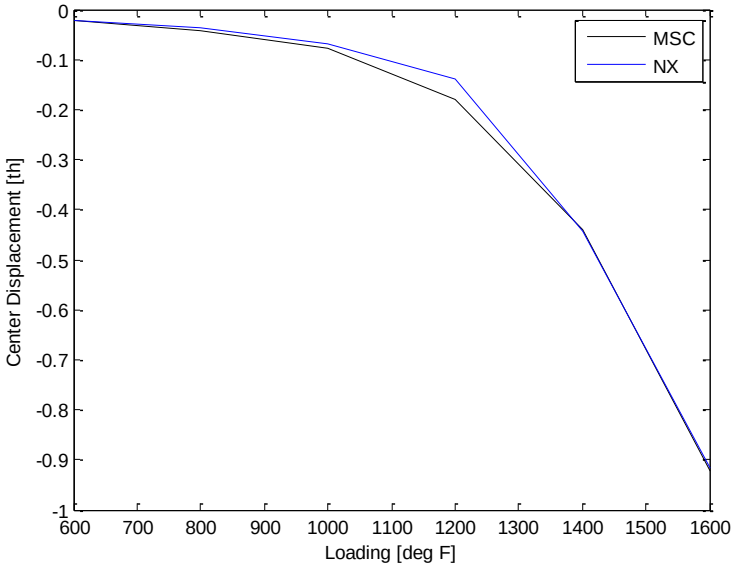

Figure 40. Center Displacement Predicted by MSC and NX Nastran SOL 106 for Uniform Temperature Loading.

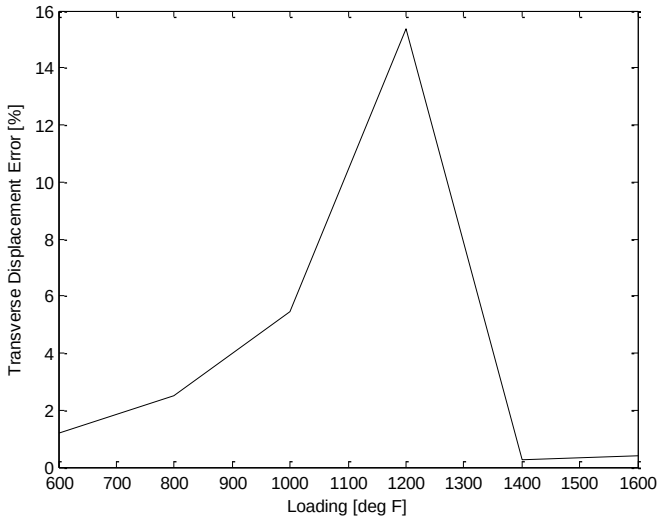

Figure 41. Transverse Displacement Error Between MSC and NX SOL 106 Solvers for Uniform Temperature Loading.

The difference between these two responses is striking, especially when considering that the solvers are expected to be quite similar, both emanating from the same code a few years ago. This comparison provides a first demonstration that the thermal buckling response is highly sensitive to small modeling variations.

Several structural reduced order models were built to test their ability to capture the thermal buckling behavior induced by uniform temperature loads. For the specific case considered here, specifically the uniform temperature case, the thermal enrichment modes were not all needed, allowing the model to be scaled back to 33 structural modes. The temperature-independent coefficient of thermal expansion of 1.33 10^{-6} 1/F was used in this effort. The quadratic and cubic stiffness coefficients of the reduced order model, i.e., $K_{ijl}^{(2)}$ and $K_{ijlp}^{(3)}$ of Eq. (5), are typically identified at reference temperature since their values are theoretically not dependent on temperature (for a derivation, see [56]). However, it was observed that these coefficients do change, depending on the temperature at which they are identified. Table 18 shows the values of the nonlinear parameters associated with the first transverse mode and first dual mode (inplane dominated) of the reduced order model identified at reference temperature as well as at 1400F, linear variations of these values with respect to the identification temperature were broadly observed. The first transverse and first dual mode, which are modes 1 and 17 respectively, were chosen because their values have been observed to be the most influential on the response of the panel.

Table 18. Effect of Temperature on Parameter Identification

Nonlinear Parameter	Identified at 0º F	Identified at 1400F	% change /1400F
$K_{1,1,1}$	3.5473E8	2.0121E8	43.2776
$K_{1,1,17}$	-1.7762E12	-1.7804E12	-0.2370
$K_{1,17,17}$	-8.0374E11	-8.0574E11	-0.2479
$K_{17,17,17}$	-8.4298E11	-8.4507E11	-0.2479
$K_{1,1,1,1}$	1.6842E12	1.6899E12	-0.3346
$K_{1,1,1,17}$	-1.4371E12	-1.4410E12	-0.2673
$K_{1,1,17,17}$	6.4021E12	6.4336E12	-0.4872
$K_{1,17,17,17}$	-8.6520E12	-8.6754E12	-0.2706

$K_{17,17,17,17}$	-4.7904E11	-4.8033E11	-0.3423

The relative change for most of the coefficients is consistent with those seen in Table 18, i.e., between 0.2% and 0.5% over the 1400F range investigated. $K_{1,1,1}$ varies much more significantly but most likely because of its much smaller absolute value. These small variations in nonlinear parameter values have a significant effect on the response of the panel, confirming the strong sensitivity deduced from the MSC/NX Nastran comparison of Figs 40 and 41. It was further found that the models identified near the buckling temperature (approximately 1500F according to a uniform temperature, linear buckling analysis) captured the thermal buckling behavior accurately. Shown below, Figs 42 and 43 show the center displacement and transverse displacement error of the model identified at reference temperature, while Figs 44 and 45 show these results for the model identified at 1400F.

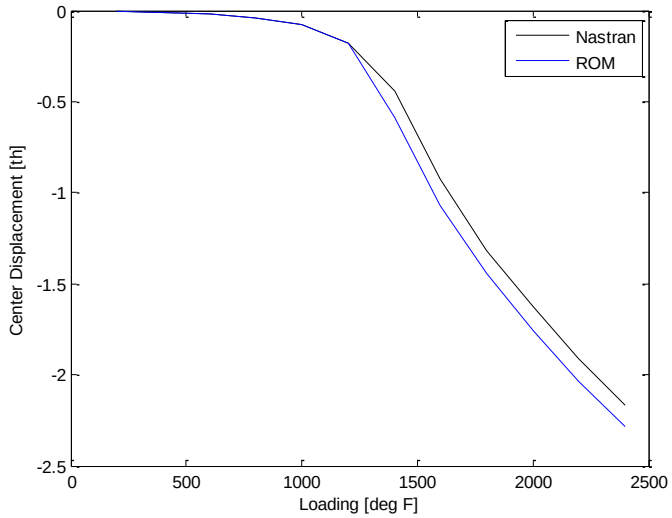

Figure 42. Center Displacement Due to Uniform Temperature Loading Predicted by MSC Nastran and the ROM Identified at Reference Temperature.

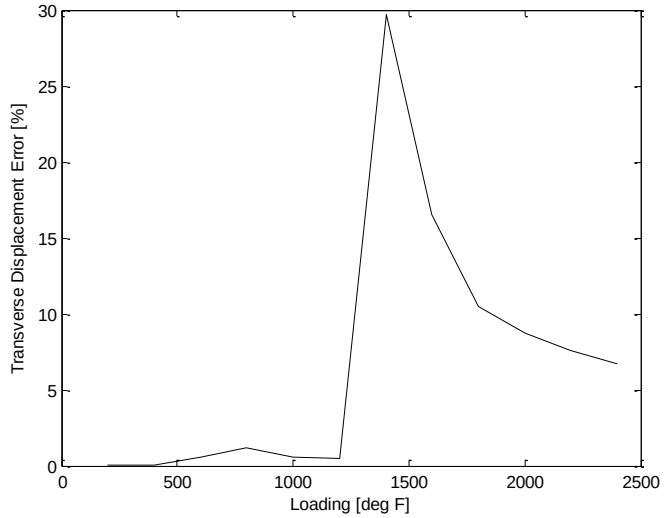

Figure 43. Transverse Displacement Error at Various Uniform Temperature Loading Levels Between MSC Nastran and the ROM Identified at Reference Temperature.

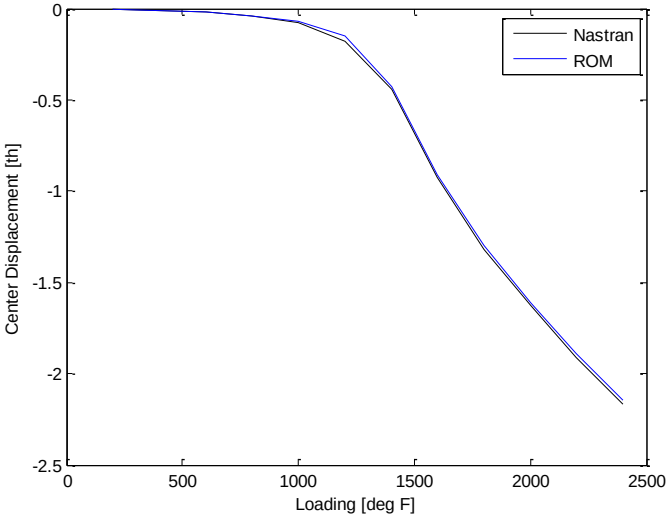

Figure 44. Center Displacement Due to Uniform Temperature Loading Predicted by MSC Nastran and the ROM Identified at 1400F.

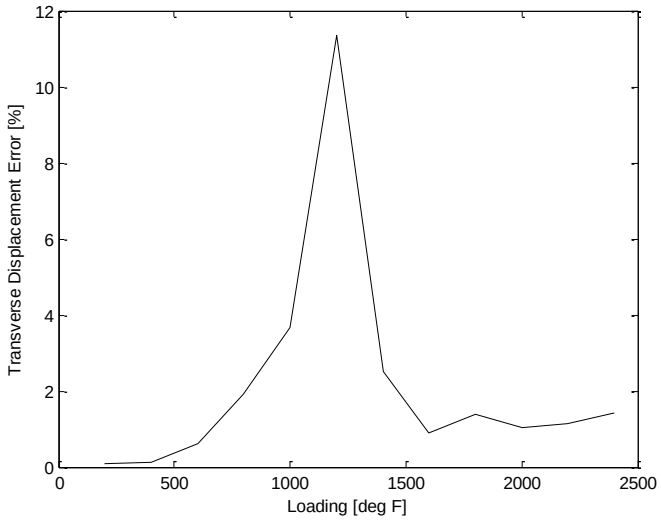

Figure 45. Transverse Displacement Error at Various Uniform Temperature Loading Levels Between MSC Nastran and the ROM Identified at 1400F.

Clearly, the small changes in parameter values allow for the model identified at 1400F to more accurately capture the buckling effect and to maintain accurate predictions after buckling. The results presented in the ensuing section for the constant CTE were obtained with a model whose nonlinear parameters were identified at 1400F.

4.2.5 300 Second Two-Way Coupled Simulation – Constant CTE

Thus far the structural model has been validated under the loading of temperature fields encountered in the one-way coupled problem. For the temperature fields arising in the two-way coupled problem it was found that the structural basis should be slightly modified, from 37 to 38 modes. The previously described model used 16 normal modes, 16 dual modes, a uniform temperature enrichment mode, and then four other enrichment modes found by performing a POD analysis on the linear structural responses to temperature fields comprising the thermal basis. The 38 mode model continues to use the 16 normal modes, 16 dual modes, and uniform temperature mode. Instead of using POD

modes, the linear structural responses to the 42 thermal modes were found and then appended to the 33 mode structural basis. The structural results of the full order model for the two-way coupled analysis were then projected onto this basis, and the five enrichment modes contributing most to the capturing of the structural response were found to be sufficient and were retained.

A fully coupled structural-thermal ROM analysis was next carried out with the 38 structural mode and 42 thermal mode model and was first achieved with the CTE held constant at 1.33 10^{-6} 1/F. The trajectory specified in [10], i.e., the constant rate ascent trajectory analysis from Mach 2 to Mach 12 in 300 seconds was adopted for the simulation and the ROM predictions were compared to the coupled full finite element analyses.

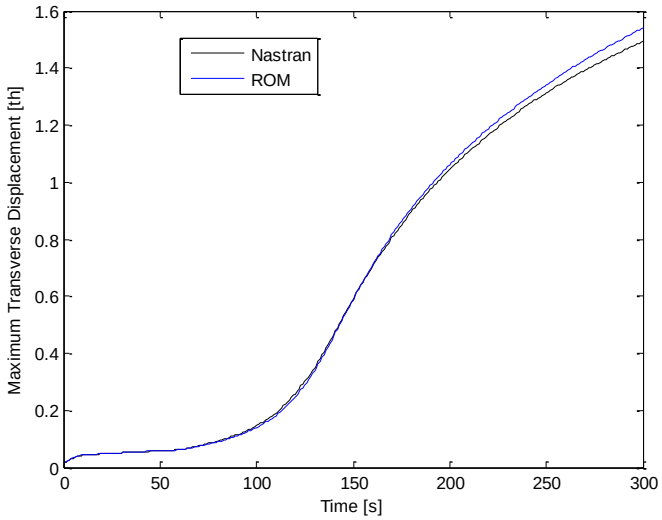

Figure 46. Maximum Transverse Displacement Predicted by ROM and Nastran for 300 Seconds.

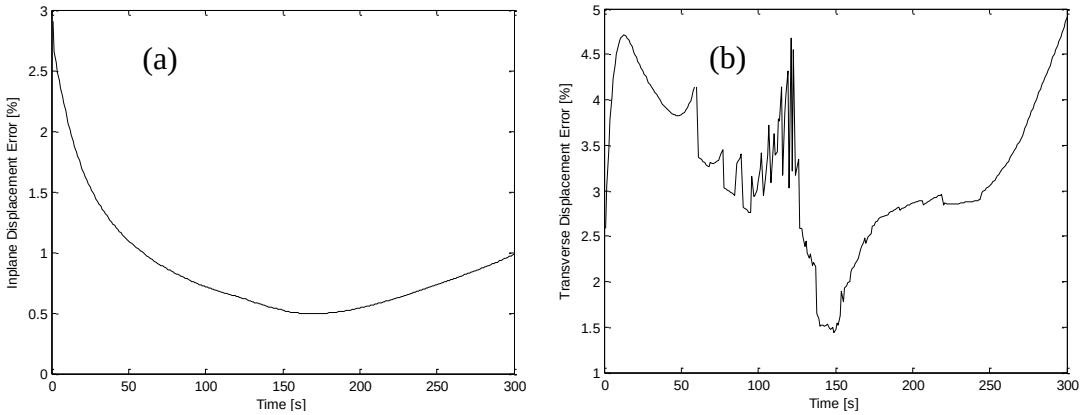

Figure 47. Structural Displacement Norm Error in a) Inplane and b) Transverse Directions Over the Trajectory.

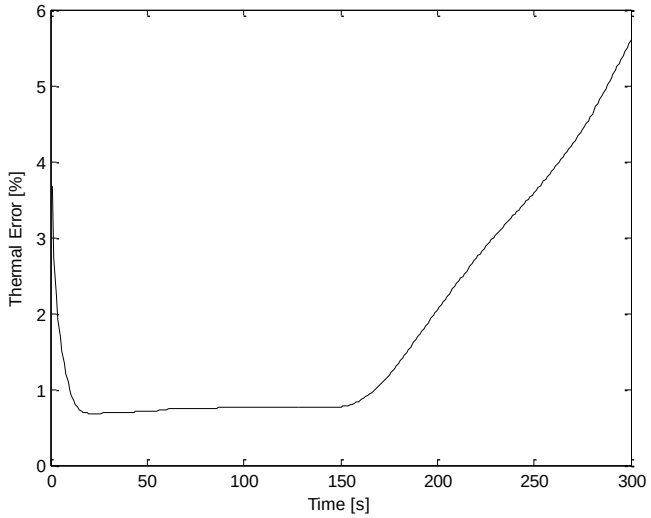

Figure 48. Norm Error in Predicted Temperature Fields Over the Trajectory.

Focusing on the structural displacements, shown in Fig. 46 are the time histories of the maximum transverse displacement predicted by the ROM and by Nastran. The agreement between these two curves is very good, albeit deteriorating slightly at the end, especially when considering the broad range of temperatures of the panel, from room temperature to 2400F. Given this matching, it could be expected that the various components of the displacement field and the temperature predicted by Nastran and the ROM match well and they do. The inplane error stays low throughout the analysis, but the transverse and thermal error are seen to rise slowly but steadily from about midway

through the analysis until the end. Comparing Figs 47(b) and 48 with Fig. 46 shows that the starting point of the increase in error is the buckling of the panel. After the panel buckles into the flow, the structural ROM predicts a larger upward displacement than Nastran. This increased transverse displacement into the flow leads to larger temperatures and thus larger displacements owing to the thermal expansion.

4.2.6 300 Second Two-Way Coupled Simulation – Temperature Dependent CTE

In Section 3.3.1.3, when describing the means by which the reduced order model is identified, the coefficient of thermal expansion and the elasticity tensor are both assumed to be linearly dependent on temperature. If this were the case, the quadratic and cubic stiffness coefficients, $K_{ijl}^{(2)}$ and $K_{ijlp}^{(3)}$, would be linearly dependent on temperature, while the linear stiffness coefficient, $K_{ij}^{(1)}$, and the thermal moment term, $F_{ij}^{(th)}$, would have a cubic dependence on temperature (see Eqs 36 through 39). However, in this analysis only the CTE is dependent on temperature. Therefore, the polynomial expressions relating the stiffness and thermal moment terms to temperature will be reduced by one order. The quadratic and cubic stiffness terms will not be dependent on temperature, while the linear stiffness and thermal moment terms will have a quadratic dependence on temperature. The method of identification outlined in Section 3.3.1.3 is still appropriate for this condition. The formulation involving both a temperature dependent coefficient of thermal expansion and elasticity tensor will be validated in Section 4.3 using the beam model.

The 38 structural, 42 thermal mode model was found to produce unsatisfactory results for the case involving a temperature dependent CTE, as shown below. Over the 300 second analysis, the first 200 seconds showed strong agreement between the ROM and Nastran. However, the behavior of the panel after 200 seconds is not well captured by the ROM.

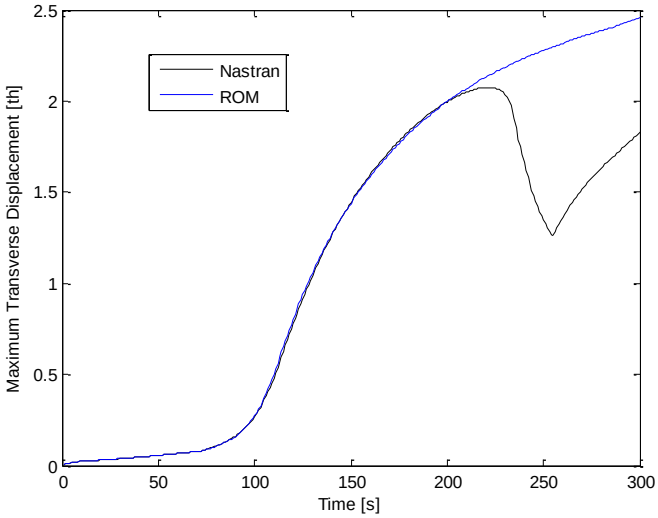

Figure 49. Maximum Transverse Displacement Predicted by ROM and Nastran for Model With Temperature Dependent CTE.

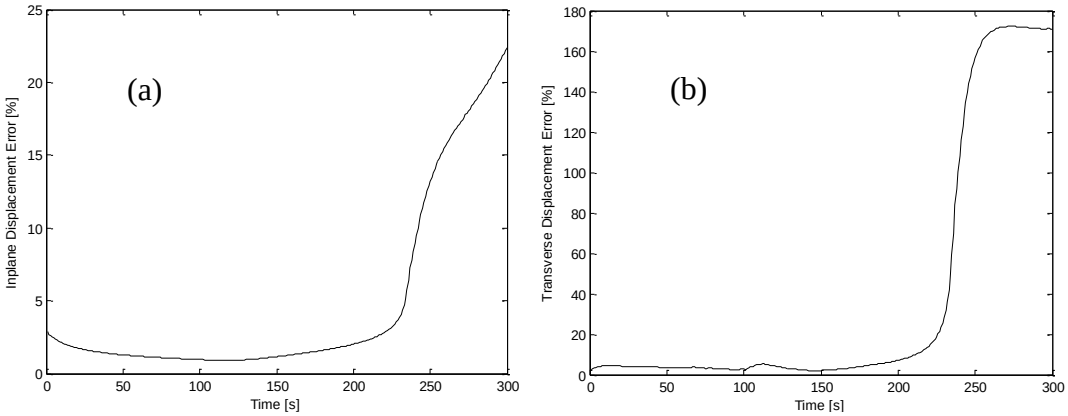

Figure 50. Structural Displacement Norm Error in a) Inplane and b) Transverse Directions for the Model With Temperature Dependent CTE.

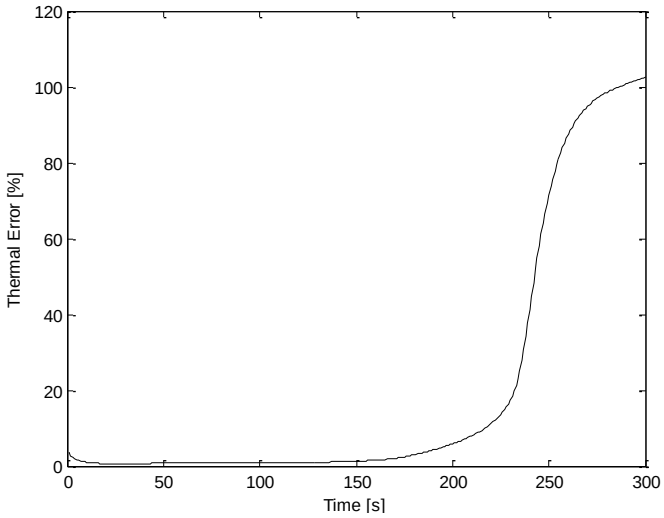

Figure 51. Norm Error in Predicted Temperature Fields for Model With Temperature Dependent CTE.

The full order model predicts that the panel will have a peak displacement near the center of the panel until about 230 seconds. The behavior up to this point is dominated by the first structural mode. Then, the peak begins to move to the front of the panel, and the back of the panel begins to be displaced in the downward direction, resembling the third normal mode of the structure. Figs 52 (a) and (b) show the first and third mode shapes, respectively. Figs 53 (a) and (b) show the displacement at 200 seconds and the displacement at 250 seconds, respectively, for the full order model. This transition is not captured by the 38 mode structural model.

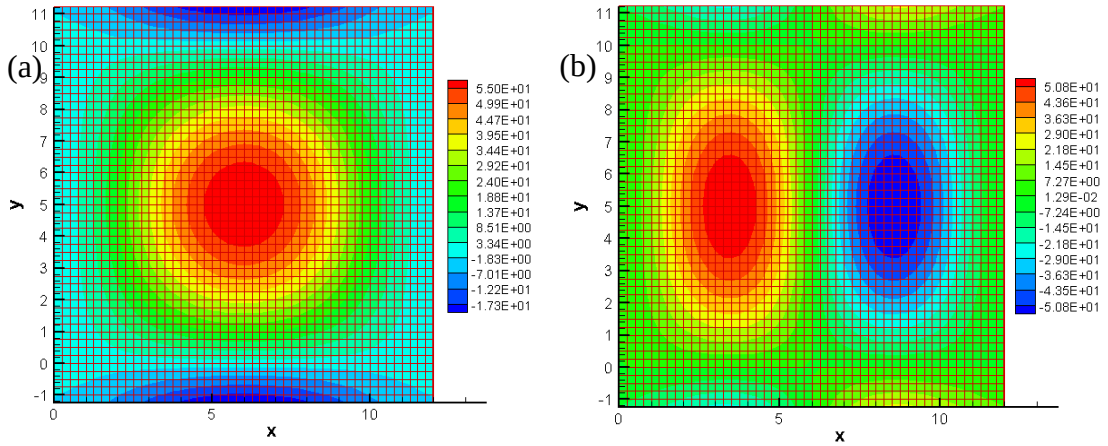

Figure 52. The Transverse Displacement of a) Normal Mode 1 and b) Normal Mode 3.

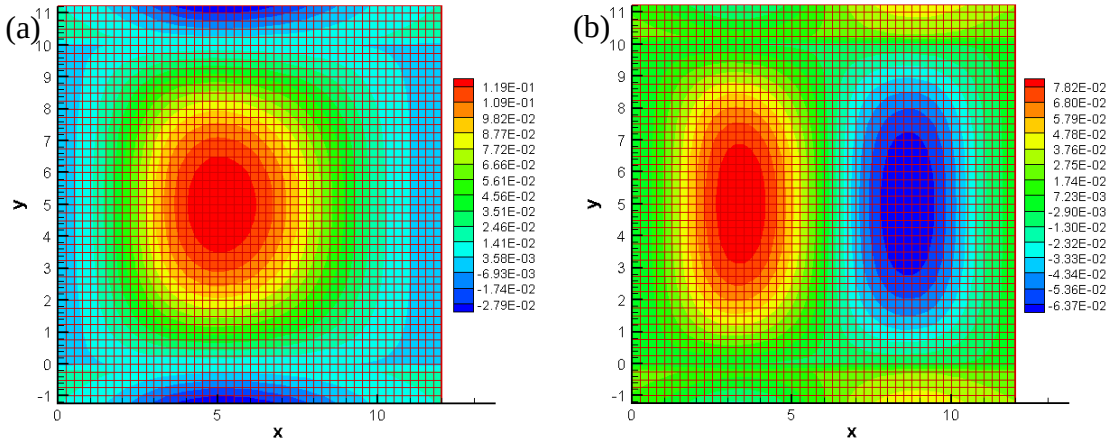

Figure 53. Transverse Response Predicted by Full Order Model With Temperature Dependent CTE at a) 200 and b) 250 Seconds of the 2-way Coupled Analysis.

The reduced order model predicted the peak moving forward to the front of the panel, but the full transition from mode 1 to mode 3 dominated deflection is never achieved. The transverse displacement of the panel at 200 seconds and 250 seconds is shown in Figs. 54 (a) and (b), respectively, for the reduced order model.

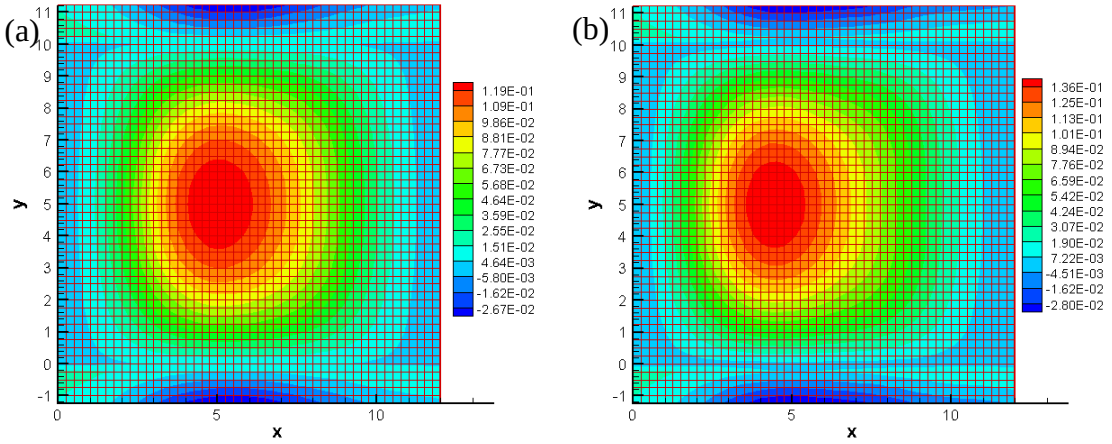

Figure 54. Transverse Response Predicted by Reduced Order Model With Temperature Dependent CTE at a) 200 and b) 250 Seconds of the 2-way Coupled Analysis.

It was suspected that the reduced order model was too stiff to transition from the mode 1 to mode 3 dominated displacement. In order to validate this suspicion, the first and third eigenvalue of the full order tangent stiffness matrix were compared to the first two eigenvalues of the ROM tangent stiffness matrix as well as the first two eigenvalues of the full order tangent stiffness matrix projected onto the ROM basis, as seen in Fig. 55. The second normal mode is not included in the reduced order model basis because it is not left/right symmetric. It should be noted that a mode switching occurs between modes 2 and 3 of the full order model, which accounts for the discrepancy in the second eigenvalue for the first 50 seconds of the simulation in Fig. 55. The projection of the full order tangent stiffness matrix onto the reduced order basis is described in Eq. 89.

$$K_{T,proj} = \Phi^T K_T \Phi \tag{89}$$

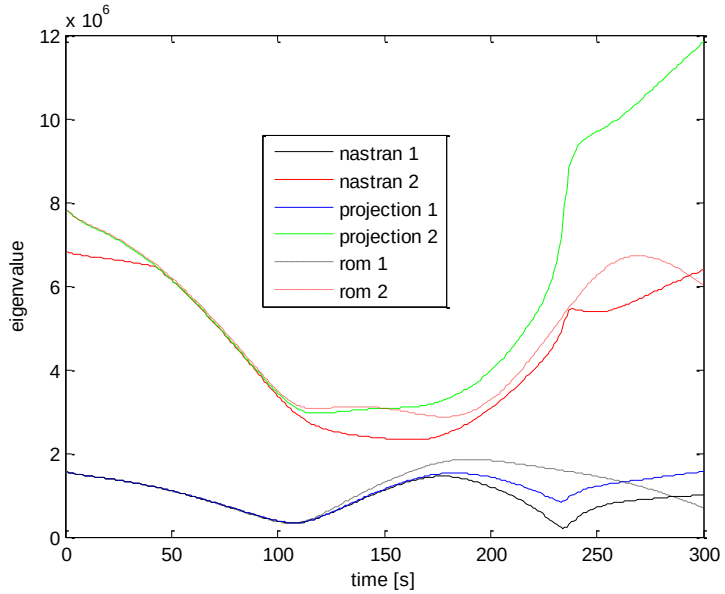

Figure 55. First and Third Eigenvalues of the Tangent Stiffness Matrix From Nastran, the First Two Eigenvalues of the 38 Mode ROM, and the First Two of the Nastran Tangent Stiffness Matrix Projected Onto the 38 Mode ROM Basis.

As seen in Fig. 55, neither the predicted ROM eigenvalues, or the eigenvalues from the projected stiffness matrix match the values predicted by the full order tangent stiffness matrix. Special attention should be given to the projected stiffness matrix eigenvalues since this is, in some sense, a best-case scenario. These values are solely dependent on the structural basis, which indicates that the 38 mode basis is not capable of producing the correct eigenvalues. Further, the eigenvalues from the ROM as well as the projected stiffness matrix are higher than those of the full order tangent stiffness matrix, confirming that the reduced order model is more stiff than the full order model.

An enrichment to the basis is needed in order for the ROM to be capable of predicting the correct eigenvalues, and thereby capture the transition from a mode 1 to a mode 3 dominated response. The first and third eigenvectors of the full order model at every second for the 300 second analysis were recorded and made orthogonal to the 38

mode structural basis. Then, a POD analysis was performed on the set of first and second eigenvectors. The first 3 POD modes from both the first and third eigenvector set were appended to the basis, resulting in a total of 44 modes. The resulting eigenvalues from the full order tangent stiffness matrix projected onto this 44 mode basis were found and can be seen plotted in Fig. 56. The matching is very good.

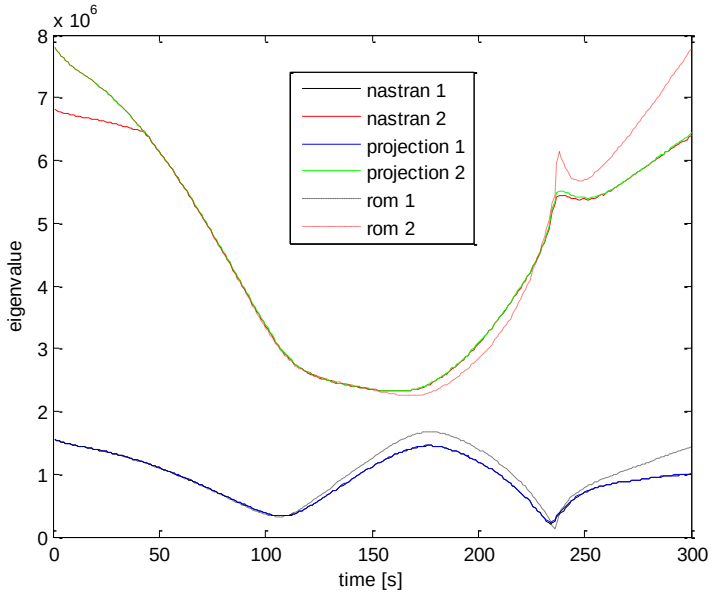

Figure 56. First and Third Eigenvalues of the Tangent Stiffness Matrix From Nastran, the First Two Eigenvalues of the 44 Mode ROM, and the First Two of the Nastran Tangent Stiffness Matrix Projected Onto the 44 Mode ROM Basis.

Next, the reduced order model parameters were identified. For the constant CTE case it was found that an identification temperature of 1400F was best to capture the thermal buckling that occurred midway through the analysis. For the temperature dependent case it was found that the model performed best when the quadratic and cubic parameters (symbols $K_{ijl}^{(2)}$ and $K_{ijlp}^{(3)}$ from Eq. 26) were identified at a temperature of 300F. The full 300 second, two-way coupled analysis was run for this new 44 mode structural, 42 mode thermal model, and the results are shown below. Additionally, an

eigenvalue analysis was performed using the tangent stiffness matrix at the predicted ROM displacements, and those values can been seen above in Fig. 56.

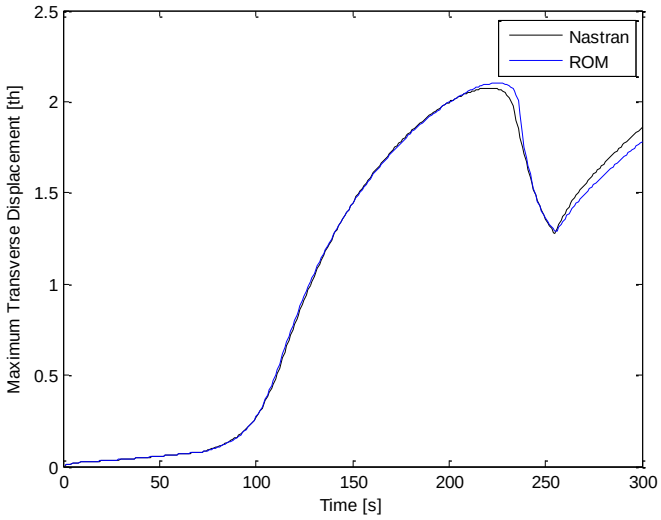

Figure 57. Maximum Transverse Displacement Predicted by ROM and Nastran Over 200 Seconds for Model With Temperature Dependent CTE.

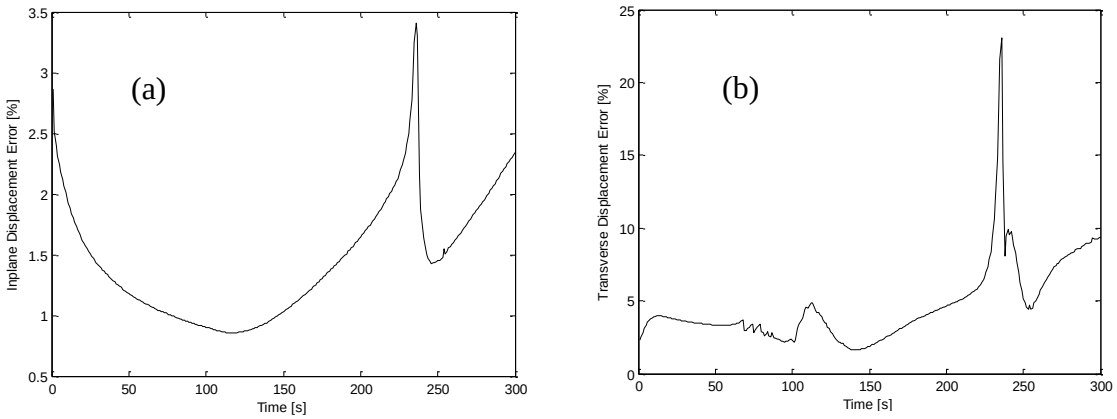

Figure 58. Structural Displacement Norm Error in a) Inplane and b) Transverse Directions for the 200 Seconds of Analysis of Model With Temperature Dependent CTE.

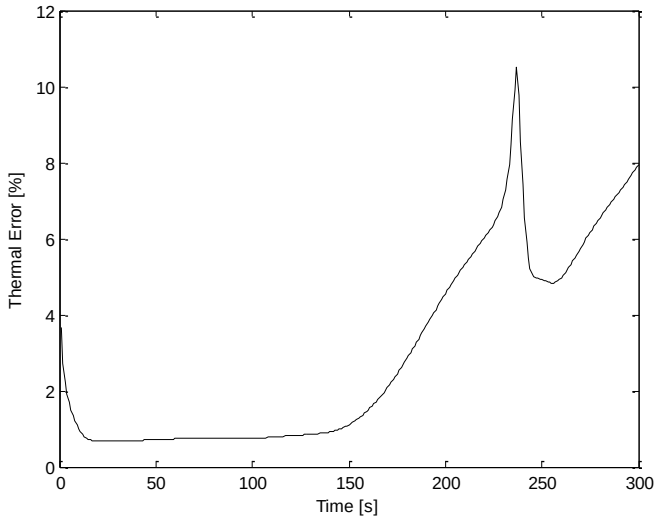

Figure 59. Norm Error in Predicted Temperature Fields Over 300 Seconds for Model With Temperature Dependent CTE.

Focusing on the structural results, the maximum error in the transverse and inplane directions are observed at around 235 seconds, which corresponds to the point at which the panel transitions from a mode 1 dominated behavior to a mode 3 dominated behavior. The errors are due to the slightly delayed reaction on the part of the ROM. However, the errors are quickly reduced once the ROM makes the transition to the third mode dominated behavior. This correlates to the difference in maximum transverse displacement seen in Fig. 57 at that same time. Additionally, the transverse and inplane error is observed to rise near the end of the analysis, correlating again to differences in the maximum predicted transverse response on the panel. Although the transverse error is 9.4%, Figs 60 (a) and (b) show that the predicted transverse displacement to be very similar after 300 seconds of simulation. The largest contribution to error is the back of the panel, which the ROM predicts to be displaced at a greater magnitude than the full order model.

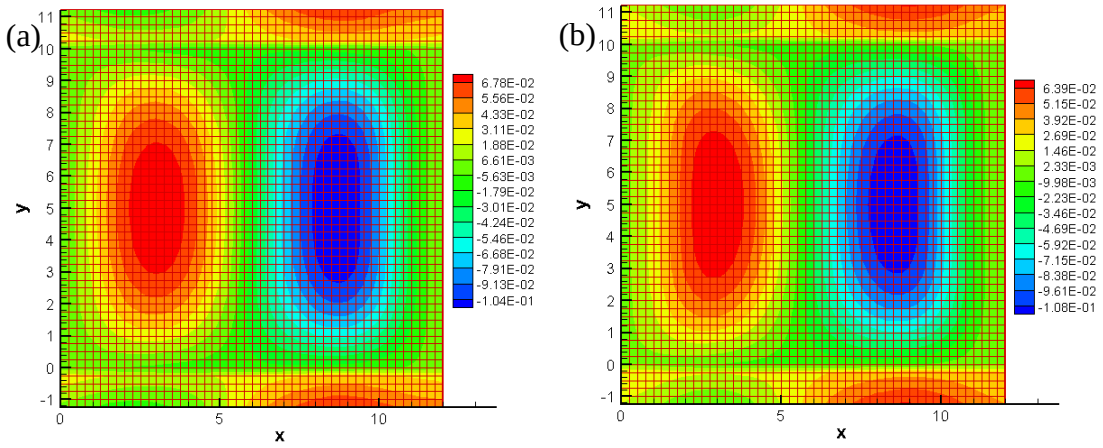

Figure 60. Transverse Response Predicted by a) Reduced Order Model and b) Full Order Model With Temperature Dependent CTE at 300 Seconds of the 2-Way Coupled Analysis.

Finally, the error in the predicted temperature fields correlates strongly with the transverse error of the structural model. Add to this the accuracy of the thermal model exhibited in Section 4.1.3 and it can be concluded that the error in the thermal results are produced by errors in the structural model.

4.3 Beam with Temperature Dependent Structural Properties

A validation of the methodology to incorporate a temperature dependent CTE and elasticity tensor into the structural reduced order model, described in Section 3.3.1.3, in comparison with full Nastran computations was performed using the beam of properties specified by Table 4 at zero temperature. Further, the changes with temperature of the Young's modulus and coefficient of thermal expansion were assumed as in Eq. (93) and (94), i.e.

$$E = E^{(0)} - E^{(1)}\, T \tag{93}$$

and

$$\alpha = \alpha^{(0)} - \alpha^{(1)}\, T \tag{94}$$

with $E^{(1)} = 3.0\ 10^{9}$ Pa/°C and $\alpha^{(1)} = 5.0\ 10^{-7}$ 1/°C^2. The Poisson's ratio was assumed to be temperature independent here. Note that these values are not representative of aluminum but rather were selected to ensure a notable change in properties with the range (10°C) of temperature experienced by the beam.

Consistent with Fig. 2, the thermal loading scenario considered here is a triangular heat flux centered on the beam, whose magnitude is prescribed to produce a peak temperature of 10 °C at the center of the panel. The bottom of the beam is held at a constant temperature of 0 °C. The temperature profile on top of the beam can be seen in Fig. 61.

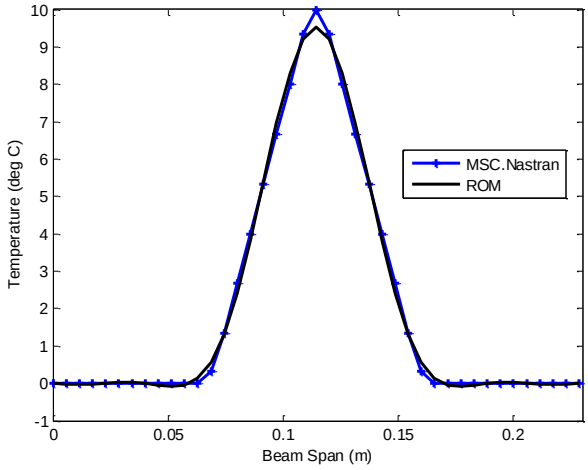

Figure 61. Temperature Profile on Top of Beam

In [62], a 10 mode thermal reduced order model was found to be sufficient for predicting the temperature distribution along the beam span. In fact, the even numbered modes do not contribute as they are antisymmetric and thus the 5-mode thermal reduced order model formed with the odd numbered modes is sufficient and is considered here for the static, symmetric loading case.

Shown in Fig. 62 are the transverse and inplane responses (labeled “temp”) obtained with both Nastran and the 17-mode structural model identified as discussed in Section 3.2.1. For brevity, the reader is referred to [62] for more details on the basis selection process. Also shown on these figures are the predictions obtained with the temperature independent properties. Note that there is large difference between these two sets of results, as desired for a thorough validation.

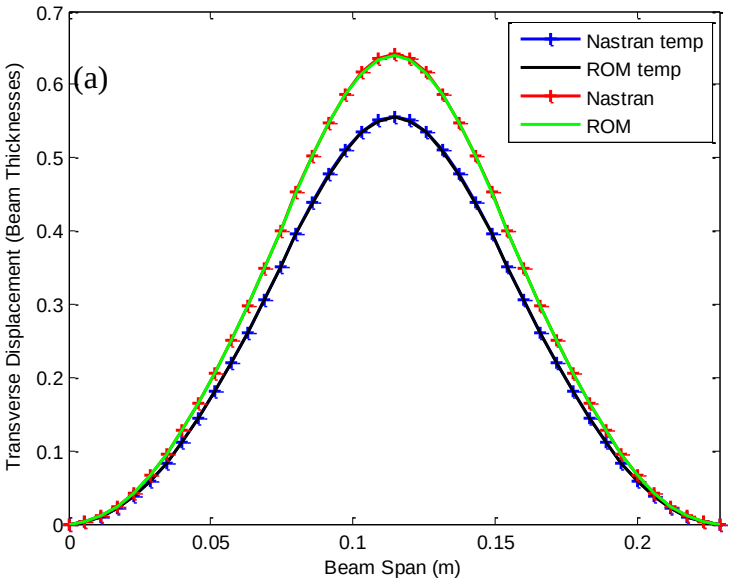

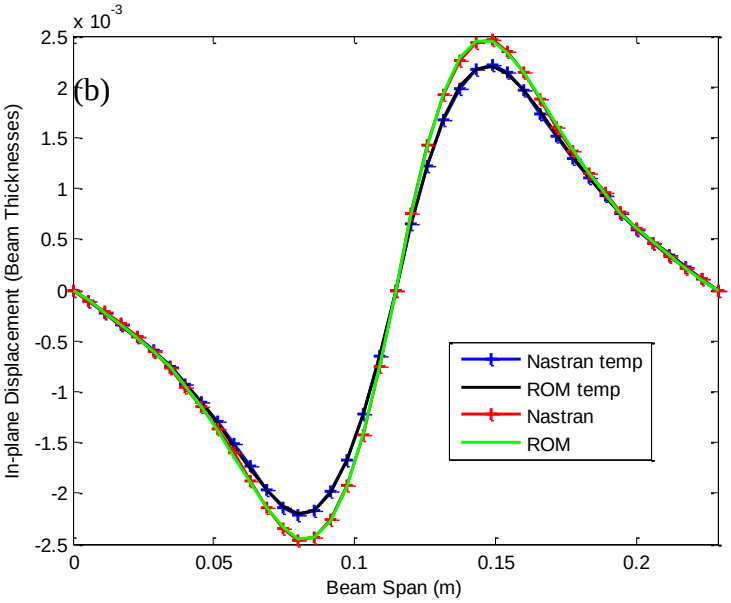

Figure 62. Displacements, (a) Transverse, (b) Inplane, Induced by the Localized Steady Heat Flux. ROM and Nastran Nonlinear Predictions for Both Temperature Dependent (Labeled "Temp") and Independent Properties.

In addition, the methodology was also validated under acoustic loading conditions, in which the excitation had an OASPL of 130 dB and frequency band of 1 kHz. Here, the heat flux was prescribed to oscillate at 20 Hz and then 40 Hz. The 5 mode thermal basis used in the previous static validation had to be increased to a 12 thermal mode basis in order to account for the unsteady heating, while the structural basis was maintained at 17 structural modes. The 12 thermal mode basis consisted of the first 10 modes previously mentioned, as well as two additional symmetric modes to better capture the peak temperature. The same linear through thickness thermal loading was provided to Nastran that was used in the ROM because of the limitations of the CBEAM element, which only accepts linear through thickness temperature variation. Figures 63 and 64 show the predictions of the ROM as well as the predictions of Nastran at the beam quarter and middle point, respectively, when an oscillating frequency of 20 Hz is applied,

while Figs 65 and 66 show the inplane and transverse response predictions with an oscillating frequency of 40 Hz. The excellent matching between the reduced order model and full Nastran displacements for the temperature dependent properties in both static and dynamic loading environments fully validates the development of Section 3.3.1.3 and accordingly demonstrates the capability of the structural ROM to account for linear variations in structural properties with respect to temperature.

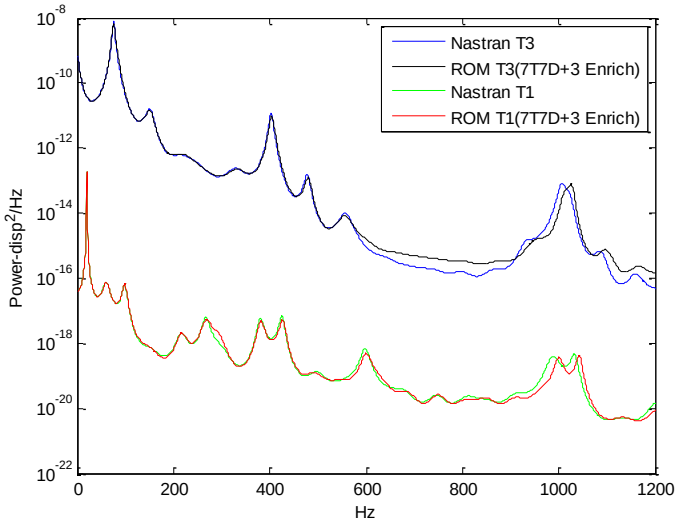

Figure 63. Power Spectral Density of the Transverse (T3) and Inplane (T1) Deflections at the Beam Middle. ROM and Nastran Nonlinear and Temperature Dependent Predictions. Oscillating Heat Flux, $\Omega=40\pi$(20Hz), and Acoustic Excitation of *SPL* =130dB.

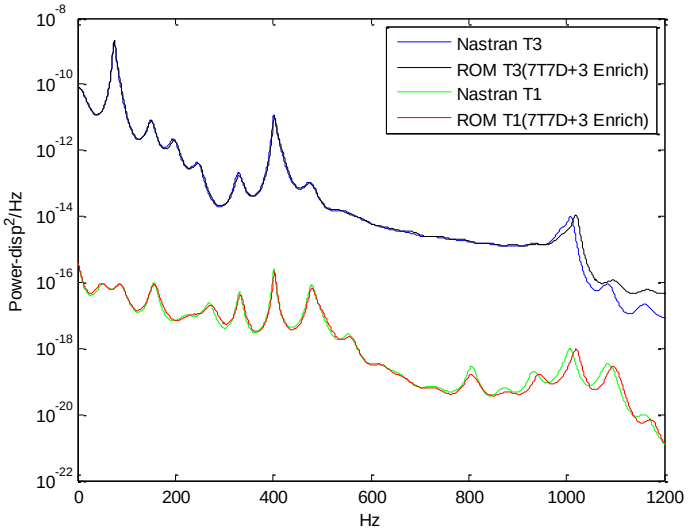

Figure 64. Power Spectral Density of the Transverse (T3) and Inplane (T1) Deflections at the Beam Quarter Point. ROM and Nastran Nonlinear and Temperature Dependent Predictions. Oscillating Heat Flux, $\Omega=40\pi(20\text{Hz})$, and Acoustic Excitation of *SPL* =130dB.

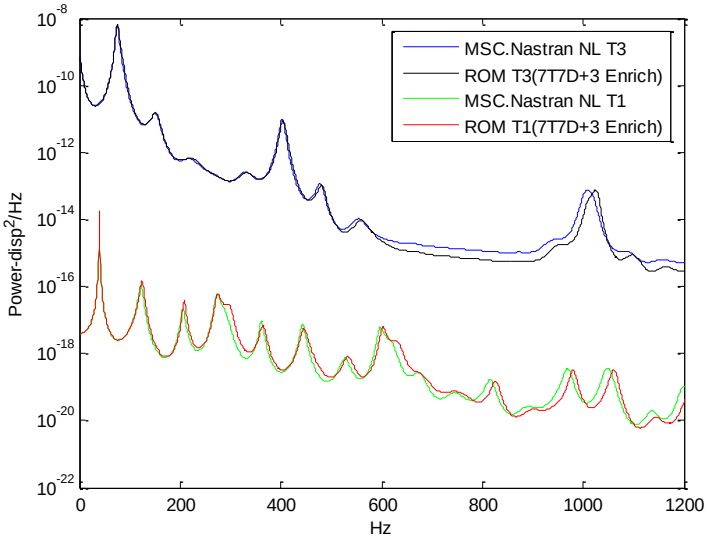

Figure 65. Power Spectral Density of the Transverse (T3) and Inplane (T1) Deflections at the Beam Middle. ROM and Nastran Nonlinear and Temperature Dependent Predictions. Oscillating Heat Flux, $\Omega=80\pi(40\text{Hz})$, and Acoustic Excitation of *SPL* =130dB.

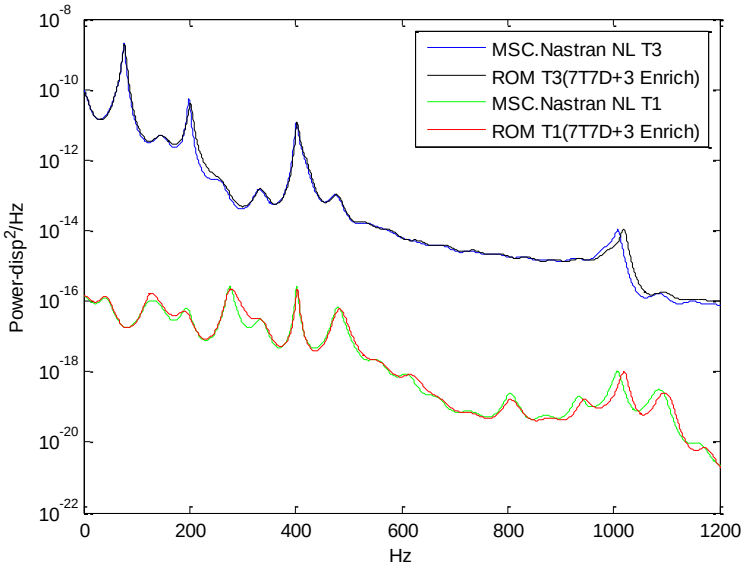

Figure 66. Power Spectral Density of the Transverse (T3) and Inplane (T1) Deflections at the Beam Quarter Point. ROM and Nastran Nonlinear and Temperature Dependent Predictions. Oscillating Heat Flux, $\Omega=80\pi$(40Hz), and Acoustic Excitation of *SPL* =130dB.

CHAPTER 5 - SUMMARY

In this paper details were presented regarding the development and validation of a coupled thermal-structural reduced order model of a 3-D representative hypersonic panel. A nonlinear thermal ROM was developed and produced accurate results compared to those found using MSC.Nastran's transient thermal solver. The thermal modes comprising the basis were constructed from eigenvectors of the capacitance-conductance eigenvalue problems, as well as enrichment modes developed to account for the coupling between the structural and thermal problems. Results from the thermal ROM compared very well with Nastran. Additionally, two different methodologies were outlined and pursued in order to provide improvements to the thermal basis. One method involved an adaptive basis that evolved as the simulation progressed, while the other developed displacement induced temperature fields. The latter method produced the greatest improvements and was utilized in this work to generate the final thermal basis. The basis for the structural model incorporated normal modes, dual modes, as well as enrichment modes provided by the linear responses of the structure to the modes of the thermal ROM. This structural basis was validated against MSC. Nastran's nonlinear structural solver when subjected to the final and most severe temperature field predicted in the one-way thermal analysis, as well as to a variety of combinations of structural and thermal loads. Maximum deflections of approximately 3 thicknesses were observed. Dynamic results were validated in isothermal conditions by subjecting the panel to acoustic excitations of 145 and 155 dB and with a frequency band of 2 kHz. A 300 second, fully coupled structural-thermal-aerodynamic simulation was performed using the thermal and

structural reduced order models and was validated against a full order thermal and structural model.

Additionally, temperature dependent material properties were incorporated into a structural reduced order model of a thin aluminum beam. The model was subjected to a localized heat flux and was validated for the case in which the flux is steady at the center of the beam and one in which the flux oscillated about the center of the beam, in addition to the presence of acoustic excitation.

REFERENCES

[1] G. Tzong, R. Jacobs, S. Liguore, "Predictive Capability for Hypersonic Structural Response and Life Prediction: Phase 1 – Identification of Knowledge Gaps," Technical Report, AFRL-RB-WP-TR-2010-3068, September 2010.

[2] B. Zuchowski, "Predictive Capability for Hypersonic Structural Response and Life Prediction, Phase 1 – Identification of Knowledge Gaps," Technical Report, AFRL-RB-WP-TR-2010-3069, August 2010.

[3] B. Zuchowski, H. Selby, J. Macguire, P. McAuliffe, "Investigation of Shortfalls in Hypersonic Vehicle Structure Combined Environment Analysis Capability," *Proceedings of the 52nd AIAA/ASME/ASCE/AHS/ASC Structures, Structural Dynamics, and Materials Conference*, Denver, Colorado, April 4-7, 2011, AIAA Paper 2011-2013.

[4] S.M. Spottswood, T.G. Eason, R. Chona, "A Structural Perspective on the Challenges Associated with Analayzing a Reusable Hypersonic Platform", *Proceedings of the 11th International Conference on Recent Advances in Structural Dynamics,* Pisa, Italy, July 1-3, 2013.

[5] B. Zuchowski, "Predictive Capability for Hypersonic Structural Response and Life Prediction: Phase II – Detailed Design of Hypersonic Cruise Vehicle Hot-Structure," Technical Report, AFRL-RB-WP-TR-2012-0280, May 2012.

[6] R. Quiroz, J. Embler, R. Jacobs, G. Tzong, and S. Liguore, "Predictive Capability for Hypersonic Structural Response and Life Prediction: Phase II – Detailed Design of Hypersonic Cruise Vehicle Hot-Structure ," Technical Report, AFRL-RQ-WP-TR-2012-0265, February 2012.

[7] B. Zuchowski, R. Wittman, K. Leung, J. Favela, "Structural Response and Service Life Prediction Concerns in the Design of Hypersonic Flight Vehicle Hot Structure," *Proceedings of the 54th AIAA/ASME/ASCE/AHS/ASC Structures, Structural Dynamics, and Materials Conference*, Boston, Massachusetts, April 8-11, 2013, AIAA Paper 2013-1457.

[8] G. Tzong, S.L. Liguore, "Verification Studies on Hypersonic Structure Thermal/Acoustic Response and Life Prediction Methods," *Proceedings of the 54th AIAA/ASME/ASCE/AHS/ASC Structures, Structural Dynamics, and Materials Conference*, Boston, Massachusetts, April 8-11, 2013, AIAA Paper 2013-1664.

[9] A.J. Culler, J.J. McNamara., "Studies on Fluid-Thermal-Structural Coupling for Aerothermoelasticity in Hypersonic Flow," *AIAA Journal*, Vol. 48, No. 8, 2010, pp. 1721–1738.

[10] A.J. Culler, J.J. McNamara, "Impact of Fluid-Thermal-Structural Coupling on Response Prediction of Hypersonic Skin Panels," *AIAA Journal*, Vol. 49, No. 11, 2011, pp. 2393-2406.

[11] C. Ostoich, D.J. Bodony, P.H. Geubelle, "Coupled Fluid-Thermal Response of a Spherical Dome due to a Mach 6.59 Laminar Boundary Layer," *AIAA Journal*, Vol. 50, No. 12, 2012, pp. 2791-2808.

[12] E.L. Blades, R.S. Miskovish, M. Nucci, P. Shah, P.G. Bremner, E.A. Luke, "Towards a Coupled Multiphysics Analysis Capability for Hypersonic Vehicle Structures," *Proceedings of the 52nd Structures, Structural Dynamics and Materials Conference*, Denver, Colorado, April 2011, AIAA-2011-1962.

[13] B.A. Miller, J.J. McNamara, S.M. Spottswood, A.J. Culler, "The Impact of Flow Induced Loads on Snap-Through Behavior of Acoustically Excited, Thermally Buckled Panels", *Journal of Sound and Vibration*, Vol. 330, Issue 23, 2011, pp. 5736-5752.

[14] R.L. Bisplinghoff, "Some Structural and Aeroelastic Considerations of High-Speed Flight," *Journal of the Aeronautical Sciences*, Vol. 23, No. 4, April 1956, pp. 289–329,367.

[15] M. Rogers, "Aerothermoelasticity," *Aero/Space Engineering*, Vol. 17, No. 10, Oct. 1958, pp. 34–43,64.

[16] R.L. Bisplinghoff, J. Dugundji, "Influence of Aerodynamic Heating on Aeroelastic Phenomena", Pergamon Press, Oxford, England, U.K., 1958, pp. 288–312.

[17] I.E. Garrick, "A Survey of Aerothermoelasticity," *Aero/Space Engineering*, Vol. 22, No. 1, Jan. 1963, pp. 140–147.

[18] E.A. Thornton, P. Dechaumphai, "Coupled Flow, Thermal, and Structural Analysis of Aerodynamically Heated Panels," *Journal of Aircraft*, Vol. 25, No. 11, Nov. 1988, pp. 1052–1059.

[19] P. Dechaumphai, E.A. Thornton, A.R. Wieting, "Flow-Thermal-Structural Study of Aerodynamically Heated Leading Edges," *Journal of Spacecraft and Rockets*, Vol. 26, No. 4, July–Aug. 1989, pp. 201–209.

[20] D. Kontinos, "Coupled Thermal Analysis Method with Application to Metallic Thermal Protection Panels," *Journal of Thermophysics and Heat Transfer*, Vol. 11, No. 2, April–June 1997, pp. 173–181.

[21] D.A. Kontinos, G. Palmer, "Numerical Simulation of Metallic TPS Panel Bowing," *Proceedings of the 36th AIAA Aerospace Sciences Meeting and Exhibit*, Jan. 1998, AIAA Paper 1998-866.

[22] R.D. Blevins, D. Bofilios, I. Holehouse, V.W. Hwa, M.D. Tratt, A.L. Laganelli, P. Pozefsky, M. Pierucci, "Thermo-Vibro-Acoustic Loads and Fatigue of Hypersonic Flight Vehicle Structure:Phase II Report," Rohr Industries, Inc., RHR 89-202, Nov. 1989; also AFRL Technical Rept., AFRL-RB-WP-TR-2009-3139, June 2009.

[23] R.D. Blevins, I. Holehouse, K.R. and Wentz, "Thermoacoustic Loads and Fatigue of Hypersonic Vehicle Skin Panels," *Journal of Aircraft*, Vol. 30, No. 6, Nov.–Dec. 1993, pp. 971–978.

[24] E.R.G. Eckert, "Engineering Relations for Heat Transfer and Friction in High-Velocity Laminar and Turbulent Boundary-Layer Flow over Surfaces with Constant Pressure and Temperature," *Transactions of the ASME*, Vol. 78, No. 6, Aug. 1956, pp. 1273–1283.

[25] E.R.G. Eckert., "Engineering Relations for Friction and Heat Transfer to Surfaces in High Velocity Flow," *Journal of the Aeronautical Sciences*, Vol.22, No.8, March 1955, pp. 585-587

[26] M.J. Lighthill, "Oscillating Airfoils at High Mach Numbers," *Journal of the Aeronautical Sciences*, Vol. 20, No. 6, June 1953, pp. 402–406.

[27] H. Ashley, G. Zartarian, "Piston Theory: A New Aerodynamic Tool for the Aeroelastician," *Journal of the Aeronautical Sciences*, Vol. 23, No. 12, Dec. 1956, pp. 1109–1118.

[28] J.J. McNamara, P.P. Friedmann, "Aeroelastic and Aerothermoelastic Analysis in Hypersonic Flow: Past, Present, and Future," *AIAA Journal*, Vol. 49, No. 6, June 2011, pp. 1089–1122.

[29] J.J. Hollkamp, R.W. Gordon, S.M. and Spottswood, "Nonlinear Modal Models for Sonic Fatigue Response Prediction: A Comparison of Methods," *Journal of Sound and Vibration*, Vol. 284, pp. 1145-1163, 2005.

[30] M. Nash, "Nonlinear Structural Dynamics by Finite Element Modal Synthesis", PhD Dissertation, Department of Aeronautics, Imperial College, The University of London, London, UK, 1977

[31] Y. Shi, C. Mei, "A Finite Element Time Domain Modal Formulation for Large Amplitude Free Vibrations of Beams and Plates", *Journal of Sound and Vibration*, Vol. 193, No. 2, 1996, 453-464.

[32] G. Maymon, "Response of Geometrically Nonlinear Elastic Structures to Acoustic Excitation-an Engineering Oriented Computational Procedure." *Computers and Structures*, Vol 18, no 4, 1984, pgs 647-652.

[33] M.I. McEwan, J.R. Wright, J.E. Cooper, A.Y.T. Leung, "A Finite Element/Modal Technique for Nonlinear Plate and Stiffened Panel Response Prediction", *Proceedings of the 42nd Structures, Structural Dynamics, and Materials Conference*, Seattle, Washington, April 2001, AIAA-2001-1595.

[34] A.A. Muravyov, S.A. Rizzi, 2003. "Determination of Nonlinear Stiffness with Application to Random Vibration of Geometrically Nonlinear Structures," *Computers and Structures*, Vol. 81, No. 15, pp. 1513-1523.

[35] S.M. Spottswood, T.G. Eason, X.Q. Wang, M.P. Mignolet, "Nonlinear Reduced Order Modeling of Curved Beams: A Comparison of Methods," *Proceedings of the 50th Structures, Structural Dynamics, and Materials Conference*, Palm Springs, California, May 4-7, 2009. AIAA Paper AIAA-2009-2433.

[36] J.J. Hollkamp, R.W. Gordon, S.M. Spottswood, "Nonlinear Sonic Fatigue Response Prediction from Finite Element Modal Models: a Comparison With Experiments", *Proceedings of the 44th Structures, Structural Dynamics, and Materials Conference*, Norfolk, Virginia, April 2003, AIAA-2003-1709.

[37] R.W. Gordon, J.J. Hollkamp, S.M. Spottswood, "Nonlinear Response of a Clamped–Clamped Beam to Random Base Excitation", *Proceedings of the Eighth International Conference on Recent Advances in Structural Dynamics*, Southampton, UK, July 2003.

[38] J.J. Hollkamp, R.W. Gordon,"Reduced-Order Models for Nonlinear Response Prediction: Implicit Condensation and Expansion," *Journal of Sound and Vibration*, Vol. 318, 2008, pp. 1139–1153.

[39] M.P. Mignolet, A. Przekop, S.A. Rizzi, S.M. Spottswood, "A Review of Indirect/Non-Intrusive Reduced Order Modeling of Nonlinear Geometric Structures", *Journal of Sound and Vibration*, Vol. 332, 2013, pp. 2437-2460.

[40] S.M. Spottswood, J.J. Hollkamp, T.G. Eason, "Reduced-Order Models for a Shallow Curved Beam Under Combined Loading", *AIAA Journal*, Vol. 48, No. 1, January 2010.

[41] J. Hollkamp, R. Gordon, "Application of Reduced-Order Models for Thermoelastic Trajectory Simulation," *Proceedings of the 53nd Structures, Structural Dynamics and Materials Conference*, Honolulu, Hawaii, Apr. 23-26 2012, AIAA -2012-1550.

[42] A. Przekop, S.A. Rizzi, "Dynamic Snap-Through of Thin-Walled Structures by a Reduced-Order Method", *AIAA Journal*, Vol. 45, No. 10, October 2007.

[43] A. Przekop, S.A. Rizzi, "Nonlinear Reduced Order Random Response Analysis of Structures With Shallow Curvature", *AIAA Journal*, Vol. 44, No. 8, 2006.

[44] S.A. Rizzi, A. Przekop, "System Identification-Guided Basis Selection for Reduced-Order Nonlinear Response Analysis", *Journal of Sound and Vibration*, Vol. 315, 2008, pp. 467–485.

[45] B.F. Feeny, R. Kappagantu, "On the Physical Interpretation of Proper Orthogonal Modes in Vibrations", *Journal of Sound and Vibration*, Vol. 211, 1998, pp. 607–616.

[46] B.F. Feeny, Y. Liang, "Interpreting Proper Orthogonal Modes of Randomly Excited Vibration System", *Journal of Sound and Vibration*, Vol. 265, 2003, pp. 953–966.

[47] R.J. Allemang, D.L. Brown, "A Correlation Coefficient for Modal Vector Analysis", *Proceedings of the International Modal Conference*, 1982.

[48] A. Przekop, X. Guo, S.A. Rizzi, "Alternative Modal Basis Selection Procedures for Reduced-Order Nonlinear Random Response Simulation", *Journal of Sound and Vibration*, Vol. 331, 2012, pp. 4005-4024.

[49] D. Chelidze, W. Zhou, "Smooth Orthogonal Decomposition-Based Vibration Mode Identification", *Journal of Sound and Vibration*, Vol. 292, 2006, pp. 461–473.

[50] U. Farooq, B.F. Feeny, "Smooth Orthogonal Decomposition for Modal Analysis of Randomly Excited Systems", *Journal of Sound and Vibration*, Vol. 316, 2008, pp. 137–146.

[51] A. Przekop, S.A. Rizzi, "Nonlinear Reduced-Order Analysis With Time-Varying Spatial Loading Distributions", *Journal of Aircraft*, Vol. 46, 2009, pp. 1395–1402.

[52] M.P. Mignolet, A.G. Radu, X. Gao, "Validation of Reduced Order Modeling for the Prediction of the Response and Fatigue Life of Panels Subjected to Thermo-Acoustic Effects", *Proceeedings of the 8th International Conference on Recent Advances in Structural Dynamics*, Southampton, UK, July 14-16, 2003.

[53] A. Radu, B. Yang, K. Kim, M.P. Mignolet, "Prediction of the Dynamic Response and Fatigue Life of Panels Subjected to Thermo-Acoustic Loading", *Proceedings of the 45th structures, structural Dynamics, and Materials Conference*, Palm Springs, California, April 19-22, 2004, Paper AIAA-2004-1557

[54] K. Kim, A. Radu, X.Q. Wang, M.P. Mignolet, "Nonlinear Reduced Order Modeling of Isotropic and Functionally Graded Plates", *International Journal of Non-Linear Mechanics*, Vol. 49, 2013, 100-110.

[55] K. Kim, V. Khanna, X.Q. Wang, M.P. Mignolet, "Nonlinear Reduced Order Modeling of Flat Cantilevered Structures", *Proceedings of the 50th Structures, Structural Dynamics, and Materials Conference*, Palm Springs, CA, May 4-7, 2009.

[56] R. Perez, X.Q. Wang, M.P. Mignolet, "Nonlinear Reduced Order Models for Thermoelastodynamic Response of Isotropic and FGM Panels", *Proceedings of the 50th Structures, Structural Dynamics, and Materials Conference*, Palm Springs, California, May 4-7, 2009.

[57] R. Perez, X.Q. Wang, M.P. Mignolet, "Nonlinear Reduced Order Models for Thermoelastodynamic Response of Isotropic and FGM Panels," *AIAA Journal*, Vol. 49, 2011, pp. 630-641.

[58] R. Perez, X.Q. Wang, M.P. Mignolet, "Steady and Unsteady Nonlinear Thermoelastodynamic Response of Panels by Reduced Order Models," *Proceedings of the 51st Structures, Structural Dynamics, and Materials Conference*, Orlando, Florida, Apr. 12-15, 2010, Paper AIAA-2010-2724.

[59] F. T. Hung, S. N. Greenschlag, and C. A. Scottoline. "Shock-Wave-Boundary-Layer Interaction Effects on Aerodynamic Heating", *Journal of Spacecraft and Rockets*, Vol. 14, No. 1, 1977, pp. 25-31.

[60] N.T. Clemens, V. Narayanaswamy, "Shock/Turbulent Boundary Layer Interactions: Review of Recent Work on Sources of Unsteadiness", *39th AIAA Fluid Dynamics Conference*, San Antonio, Texas, 2009, AIAA Paper 2009-3710, 2009.

[61] D. S. Dolling and M. T. Murphy. "Unsteadiness of the Separation Shock Wave Structure in a Supersonic Compression Ramp Flowfield", *AIAA Journal*, Vol. 21, No. 12, 1983, pp. 1628-1634.

[62] A. Matney, R. Perez, M.P. and Mignolet, "Nonlinear Unsteady Thermoelastodynamic Response of a Panel Subjected to an Oscillating Flux by Reduced Order Models", *Proceedings of the 52nd Structures, Structural Dynamics and Materials Conference*, Denver, Colorado, Apr. 4-7 2011, AIAA 2011-2016.

[63] A. Matney, R. Perez, S.M. Spottswood, X.Q. Wang, M.P. and Mignolet, "Nonlinear Structural-Thermal Reduced Order Modeling of a Representative Hypersonic Structure", *Proceedings of the 53nd Structures, Structural Dynamics and Materials Conference*, Honolulu, Hawaii, Apr. 23-26 2012, AIAA -2012-1972.

[64] A. Matney, "Thermoelastodynamic Responses of Panels Through Nonlinear Reduced Order Modeling: Oscillating Flux and Temperature Dependent Properties", M.S. Thesis, Arizona State University, August 2011.

[65] R. Perez, X.Q. Wang, M.P. and Mignolet, "Reduced Order Model for the Geometric Nonlinear Response of Complex Structures," *Proceedings of the 24th Conference on Mechanical Vibration and Noise,*, Chicago, Illinois, Aug. 12-15, 2012. ASME Paper DETC2012/MECH-71141.

[66] N.J. Falkiewicz, C.E.S. Cesnik, "Proper Orthogonal Decomposition for Reduced-Order Thermal Solution in Hypersonic Aerothermoelastic Simulations," *AIAA Journal*, Vol. 49, No. 5, 2011.

[67] N.J. Falkiewicz, C.E.S. Cesnik, A.R. Crowell, J.J. McNamara, "Reduced Order Aerothermoelastic Framework for Hypersonic Vehicle Control Simulation", *AIAA Journal*, Vol. 49, No. 8, August 2011.

[68] T.W. Simpson, T.M. Mauery, J.J. Korte, and F. Mistree, "Kriging Models for Global Approximation in Simulation Based Multidisciplinary Design Optimization", *AIAA Journal*, Vol.39, No.12, Dec. 2001, pp. 2233-2241.

[69] T. Kumano, S. Jeong, S. Obayashi, Y. Ito, K. Hatanaka, H. Morino, "Multidisciplinary Design Optimization of Wing Shape for a Small Jet Aircraft Using Kriging Model", *Proceedings of the 53nd Structures, Structural Dynamics and Materials Conference*, Reno, Nevada, Jan. 9-12, 2006, AIAA Paper 2006-0932.

[70] X.B. Lam, Y.S. Kim, A.D. Hoang, C.W. Park, "Coupled Aerostructural Design Optimization Using the Kriging Model and Integrated Multiobjective Optimization Algorithm", *Journal of Optimization Theory and Applications*, Vol. 142, No. 3, March 2009, pp. 533-556.

[71] H.G. Maahs, *Flight-Vehicle Materials, Structures, and Dynamics, Vol. 3: Ceramics and Ceramic-Matrix Composites*, Ch. 16: Carbon–Carbon Composites, ASME, New York, 1992.

[72] J. Neumeister, S. Jansson, F. Leckie, "The Effect of Fiber Architecture on the Mechanical Properties of Carbon/Carbon Fiber Composites," *Acta Materialia*, Vol. 44, No. 2, 1996, pp. 573–585.

[73] J.G. Zhao, K.Z. Li, H.J. Li, C. Wang, Y.Q. Zhai, "The Thermal Expansion of Carbon/Carbon Composites from Room Temperature to 1400 C," *Journal of Material Science and Technology*, Vol. 41, 2006, pp. 8356–8358.

[74] J.D. Buckley, "Carbon–Carbon, An Overview," *American Ceramic Society Bulletin*, Vol. 67, No. 2, Feb. 1988, pp. 364–368.

[75] C.W. Ohlhorst, W.L. Vaughn, P.O. Ransone, H.T. Tsou, "Thermal Conductivity Database of Various Structural Carbon–Carbon Composite Materials," Nov. 1997, NASATM 2006-214301.

[76] J.D. Anderson, Jr., *Modern Compressible Flow with Historical Perspective*, 3rd ed., McGraw–Hill, New York, 2003.

[77] Y.C. Fung, P. Tong, 2001. *Classical and Computational Solid Mechanics*. River Edge: World Scientific.

[78] J. Bonet, R.D. Wood, 1997. *Nonlinear Continuum Mechanics for Finite Element Analysis.* Cambridge: Cambridge University Press.

[79] L. Vujosevic, V.A. Lubarda, "Finite-Strain Thermoelasticity based on Multiplicative Decomposition of Deformation Gradient," *Theoretical and Applied Mechanics*, Vol. 28-29, 2002, pp. 379-399.